POLITECNICO DI MILANO

School of Industrial and Information Engineering

Master of Science degree in Engineering Physics

Optimization of a lab-on-a-chip rapid diagnostic test for malaria

Supervisor: Prof. Giorgio Ferrari
Co-supervisor: Prof. Riccardo Bertacco
PhD Marco Giacometti

M.Sc. Thesis of:
Federico Fagiani
Student ID Number: 897183

Academic Year 2018-2019

Contents

List of Figures

List of Tables

Acknowledgements

I would first and foremost like to thank Prof. Riccardo Bertacco, who offered me such a great opportunity to join TMek project. I thank him for his time and for his constant assistance during the whole thesis work. I wish to thank Prof. Giorgio Ferrari for his stimulating insights and his helpfulness. To Marco Giacometti and Francesca Milesi my biggest gratitude: no one could ever ask for a better team; I found in you not simple colleagues, but real friends. Also deserving special thanks to Lorenzo Coppadoro and Luca Paroni for their congeniality and expertise. Of course, I must also thank PoliFAB staff and NaBiS group made of by great people, who taught me a lot, as a student and as a man.

Remembering all the people who shared these years is not easy, to them goes my sincerest thanks: without even your small contribute, I would not be who I am now.

Finally, I would like to express my profound gratitude to my friends, Chiara, my family and my parents: I am forever indebted for their full kindest support in every single step of my life.

Abstract

Malaria remains the most important mosquito-borne infectious disease worldwide, with 3.5 billion people still at risk, 228 million cases and 405 000 deaths in 2018. The disease is caused by parasites belonging to the genus of *Plasmodium*, which infect red blood cells by feeding on hemoglobin and transforming it into hemozoin nanocrystals. Despite the World Health Organization recommends "prompt parasite-based diagnosis in all patients suspected of malaria before treatment is administered, either by microscopy or malaria rapid diagnostic test (RDTs)", the quality of microscopy-based diagnosis is frequently inadequate while the reliability of RDTs based on antigens detection is still affected by a sizable number of false negative/positive results.

This Master's thesis project is about the optimization and characterization of a lab-on-a-chip pan-malaria rapid diagnostic test, that, based on the paramagnetic properties of hemozoin nanocrystals, combines magnetophoretic separation and electrical impedance detection. The presented diagnostic test, exploiting the competition between gravity and magnetic forces, relies on the local capture of infected red blood cells and hemozoin crystals on micromagnetic concentrators and subsequent detection by electrical measurement. The long-range attraction is provided by external NdFeB permanent magnets, while a concentration on the electrodes is performed by Ni pillars fabricated in the chip. Finally, because of the presence of particles within a solution changes its conductivity, the amount of hemozoin crystals and infected red blood cells can be quantified through an impedance variation detection.

During this thesis work, different activities have been carried out to characterize and optimize a diagnostic platform previously developed. First, a solid and reliable analysis code has been realized and used during a preclinical validation study carried out in Cameroon. Then, other important characterization experiments have been performed to demonstrate a limit of detection (LoD) of 10parasites$\cdot\mu l^{-1}$ and a measurement range from the LoD up to 10^5parasites$\cdot\mu l^{-1}$. During the thesis, the first follow up monitoring has also been carried out. Later, a new microchip with interpenetrated sensitive regions has been designed, fabricated and characterized in order to remove the spurious drift signal affecting the previous chip.

This thesis work was part of the *TMek project*. The experimental activities have been performed in *PoliFAB*, the micro and nanotechnology center of the "Politecnico di Milano", under the direct supervision of Prof. Giorgio Ferrari and Prof. Riccardo Bertacco, head of the *Nanomagnetism for Biology and Spintronics* group of the Department of Physics, and in *"Luigi*

Sacco" hospital in Milan. The detection system has been developed in collaboration with the I^3N group of "Politecnico di Milano", directed by Prof. Marco Sampietro and Prof. Giorgio Ferrari, that designed, fabricated and characterized the electronics of the device. The blood samples used in the calibration tests have been provided and treated by *μBS Lab* of "Politecnico di Milano", led by Prof. Gianfranco B. Fiore, while the prevalidation campaign has been carried out in the diagnostic laboratory of *Hôpital Saint Luc* of Mbalmayo in Cameroon.

Sommario

La malaria con 3.5 miliardi di persone ancora a rischio, 228 milioni di casi e 405 000 morti nel 2018, rimane la più importante malattia al mondo causata da puntura di zanzara. La malattia è causata dai parassiti del genere *Plasmodium*, che infettano i globuli rossi nutrendosi dell' emoglobina e trasformandola in nanocristalli di emozoina. Nonostante l' Organizzazione Mondiale della Sanità raccomandi una "pronta diagnosi, o con microscopio o usando test diagnostici rapidi (RDT), in tutti i pazienti sospetti di malaria prima che venga loro somministrato un trattamento", la qualità della diagnosi con microscopio è frequentemente inadeguata, mentre l'affidabilità degli RDT basati sull' individuazione di antigeni è ancora affetta da un considerevole numero di falsi positivi e falsi negativi.
Questo progetto di tesi magistrale tratta l'ottimizzazione e la caratterizzazione di un lab-on-a-chip test diagnostico rapido pan-malarico che, basandosi sulle proprietà magnetiche dell'emozoina, combina la separazione magnetoforetica e la tecnica di misura impedenziometrica. Il test diagnostico presentato, sfruttando la competizione tra la gravità e le forze magnetiche, si basa sulla cattura locale dei globuli rossi infetti e dei cristalli di emozoina su concentratori micromagnetici e la seguente misura elettrica. L'attrazione su lungo raggio è data da magneti esterni permanenti di NdFeB, mentre una concentrazione sugli elettrodi è eseguita da strutture di Ni fabbricate nel chip. Infine, a causa del cambio di conduttività in una soluzione data la presenza di particelle, la quantità di cristalli di emozoina e globuli rossi infetti può essere valutata attraverso una misura impedenziometrica.
Durante questo lavoro di tesi, sono state eseguite diverse attività in modo da caratterizzare e ottimizzare la piattaforma diagnostica precedente. In primo luogo è stato scritto un codice di analisi robusto e affidabile, usato poi durante la validazione clinica in Camerun. Dopodiché, altri importanti esperimenti sono stati condotti volti a dimostrare il valore minimo di parassitemia misurabile (LoD) di 10parassiti$\cdot\mu l^{-1}$ e una curva di calibrazione dal LoD fino a una concentrazione di 10^5parassiti$\cdot\mu l^{-1}$. Durante la tesi, è stato inoltre eseguito il primo esperimento di monitoraggio (follow up). Più tardi, un nuovo microchip con aree sensibili compenetrate è stato ideato, fabbricato e caratterizzato in modo da rimuovere il segnale spurio di drift tipico del chip precedente. Questa tesi è stata parte del progetto *TMek*.
Le attività sperimentali sono state eseguite a *PoliFAB*, il centro di nano e micro tecnologia del Politecnico di Milano sotto la diretta supervisione dei Prof. Giorgio Ferrari e Prof. Riccardo Bertacco, direttore del gruppo *"NABIS"* del Dipartimento di Fisica del Politecnico di Milano, e all' Ospedale Luigi Sacco di Milano. Il sistema elettronico del dispositivo è stato sviluppato e

caratterizzato in collaborazione con il gruppo I^3N del Politecnico di Milano, diretto dai Prof. Marco Sampietro e Prof. Giorgio Ferrari. I campioni di sangue usati nei test di calibrazione sono stati forniti e trattati dal gruppo *μBS Lab* del Politecnico di Milano, guidato dal Prof. Gianfranco B. Fiore, mentre la campagna di validazione clinica è stata fatta nel laboratorio di diagnosi dell' Hôpital Saint Luc di Mbalmayo in Camerun.

CHAPTER I

Introduction

I.1. Malaria in the world

Malaria is a life-threatening disease that affects humans and other animals. It is caused by parasites belonging to the genus of *Plasmodium* [1, 2]. These micro-organisms are transmitted to people through the bites of infected female *Anopheles* mosquitoes, called "malaria vectors". Even though over one hundred different species of *Plasmodium* have been classified, just five can infect and be spread by humans: *P. ovale*, *P. malariae*, *P. knowlesi*, *P. vivax* and *P. falciparum* [1, 3]. While the others have milder outcomes, only the last two, *P. vivax* and *P. falciparum*, can cause anemia and severe malaria with fatal effects: the former one is less dangerous, but can still carry complications, while the latter is the most virulent and lethal [4]. About eight to twenty-five days after the bite of an infected mosquito, malaria causes a wide variety of typical symptoms such as fever, headaches, tiredness and, in the worst cases, usually associated with *P. falciparum*, coma and death [1, 4].
In 2018 an estimated 228 million cases of malaria occurred worldwide and most of them were in the African Region (213 million or 93%), followed by the South-East Asia Region with 3.4% of the cases and the Eastern Mediterranean Region with 2.1%, according to the *World Health Organization* (by now WHO). *Plasmodium falciparum* is the most prevalent malaria parasite in the African Region, accounting for 99.7% of estimated malaria cases in 2018, as well as in the South-East Asia Region (50%), the Eastern Mediterranean Region (71%) and the Western Pacific Region (65%) [2]. According to the "World malaria report 2019", in the last year, there were approximately 405 000 deaths from malaria globally, where children aged under 5 years still represent the most vulnerable group, about 67%, of all malaria deaths worldwide [2]. Apart from the obvious disastrous consequences on life and health themselves, malaria brings with it clear economic and social effects [5]. In its entirety, the economic impact of malaria (including costs of health care, working days lost due to sickness, days lost in education, loss of investment and tourism, etc.) has been estimated to cost Africa US$12 billion every year [6]. In Fig.1, the distribution of malaria in 2018 is displayed.

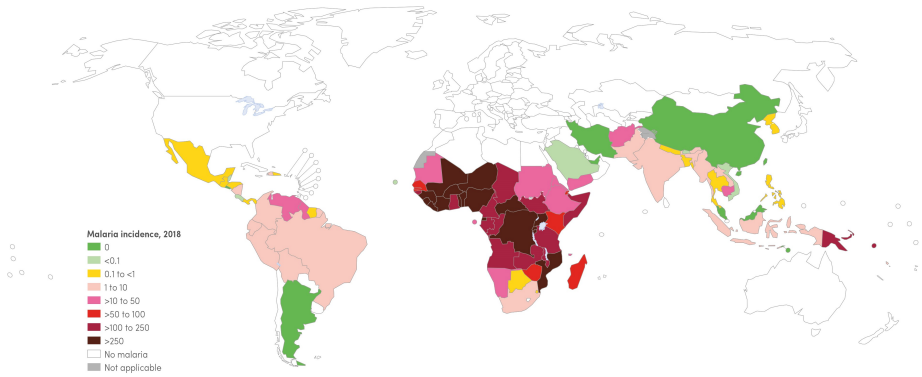

FIGURE 1. *Map of malaria case incidence (cases per 1000 population at risk) by country, in 2018*, [2].

Strengthened attempts are being made to dramatically reduce the disease burden: between 2010 and 2018, the rate of new cases among populations at risk fell by 10% all over the world. As stated in Fig.2, the elimination net is widening, with more countries moving towards zero indigenous cases: in fact, the amount of nations with fewer than 10 up 10000 indigenous malaria cases, is monotonously increasing. The number of nations with fewer than 100 indigenous cases, a strong indicator that elimination is within reach, increased from 17 in 2010, to 25 in 2017 and finally to 27 in 2018.

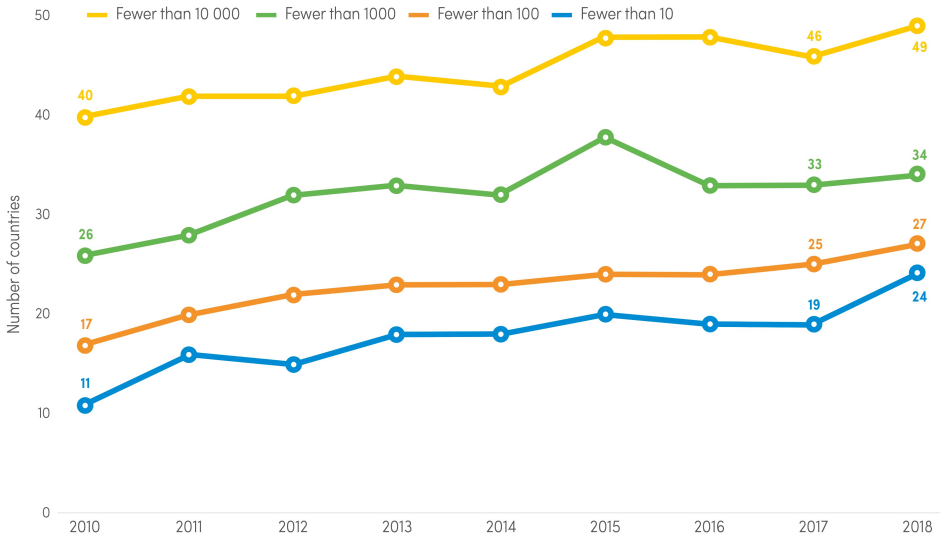

FIGURE 2. *Number of malaria endemic countries with fewer than 10, 100, 1000 and 10000 indigenous malaria cases between 2010 and 2018, [2].*

Despite this positive trend, malaria still remains the most important parasitic disease and the second infectious one in the world for morbidity and mortality after tuberculosis. It follows that great efforts are still needed, in prevention and treatment, as well as in the development of proper diagnostic systems. In order to eradicate and eliminate malaria, several programs have been set up and relevant scientific challenges have been addressed [7].
There are various methods used to prevent and treat malaria, starting from elimination of mosquitoes and the prevention of bites. For individual protection, the most effective insect repellents are based on *picaridin*; on the other hand, *insecticide treated mosquito nets (ITNs)* and *indoor residual spraying (IRS)* have shown to be highly effective in preventing malaria among children in endemic areas [8].
Furthermore, climate is a key determinant of both the geographic distribution and the seasonality of malaria: without sufficient rainfall, mosquitoes cannot survive, and, if not sufficiently warm, parasites cannot replicate in the mosquito. In warm climates people are more likely to sleep unprotected outdoors, thereby increasing exposure to night-biting *Anopheles* mosquitoes. Nevertheless, many of the most dangerous species bite human indoors: for these species, *ITNs* and indoor residual spray are effective interventions. It must be highlighted also the possibility of transmission throughout others ways apart of mosquitoes: infected blood administration, transplacental passage between a mother and the child during pregnancy and the so-called "airport disease" which affects western people travelling to tropical countries [3].
Proper treatment of malaria requires a good knowledge of critical information such as the genus of *Plasmodium*, the stage of infection, expected drug susceptibility etc. Having said this, there are anyway some guidelines for clinicians to be followed: the most effective treatment for *P. falciparum* is known as *artemisinins-combination therapy* or *ATC* and includes the use of *artemisinins* in combination with other antimalarials such as *amodiaquine*, *lumefantrine*, *pyrimethamine* or *primaquine*. *ACTs* are about 90% effective when used to treat not-severe malaria and this is the suggested drug approach to treat malaria due to *P. falciparum* all over the world [9]. Apart from *artemisinins*, *chloroquine* is known as one of the most used anti-malaria drugs. By the way, it represents a shining example of drug for which an increasing drug resistance in endemic countries has been observed in the 21st century [1]. Indeed, in these regions, the efficacy of chloroquine against *P. falciparum* has decreased because of a strengthening of the parasite itself.
Severe malaria still has a fatality rate around 20%; nevertheless, when properly treated, a complete recovery can be achieved. Nevertheless, it is clear from this picture how transmission prevention and treatments are not the final answer, but further strategies can be followed. It emerges that a prompt and efficient diagnosis becomes fundamental in order both to reduce deaths and the number of *false positives*, which is a type of over-diagnosis favouring drug resistance due to the prescription of unnecessary drugs [1, 10]. Nowadays clinicians can study the potential case of malaria with different techniques: the most frequently used are the microscopic examination of *blood films*, both *thin* and *thick*, and the so-called *malaria rapid diagnostic tests* (*RDTs*). Nevertheless, there's a strong need for the development of more efficient diagnostic tests [2, 11], as explained later (see section I.3).

I.2. Biology of malaria

For malaria transmission to occur, conditions must be such that all three components of the malaria life cycle are present: *Anopheles mosquitoes*, able to feed on human blood, and in which parasites can complete the "invertebrate-host" half of their life cycle, *humans*, who can be bitten by mosquitoes, and in whom parasites can complete the "vertebrate-host" part of their life cycle and finally *malaria parasites*. In Fig.3 malaria cycle is represented.

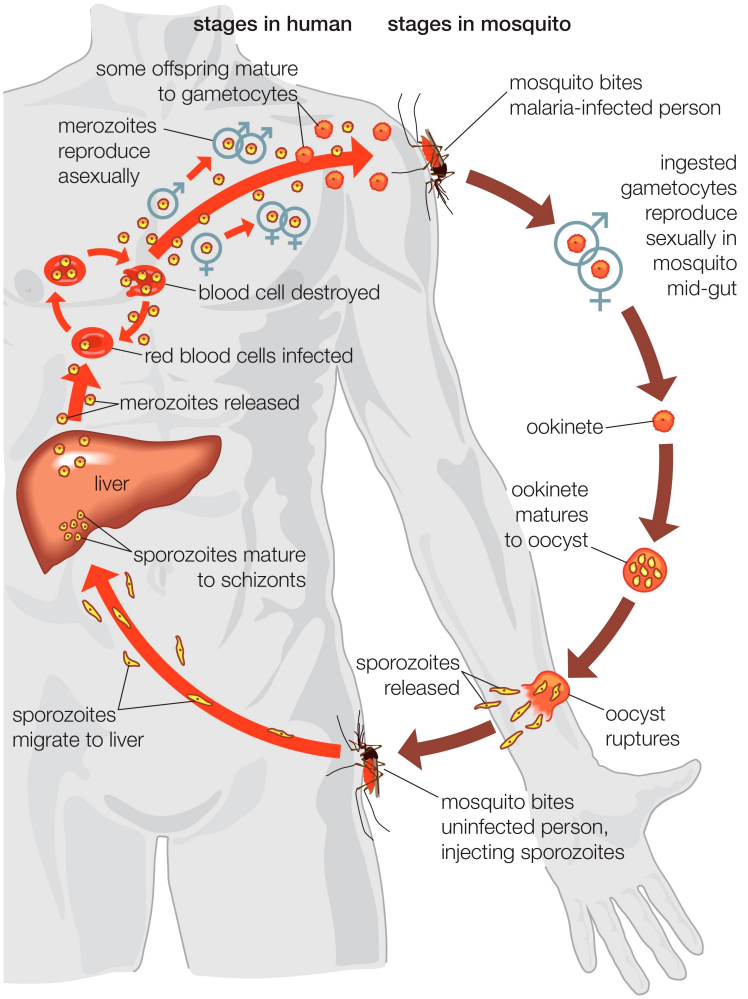

FIGURE 3. *Life cycle of Plasmodium both in human and mosquito, [12].*

A malaria episode begins when an infected female *Anopheles* mosquito bites a person, inoculating *Plasmodium* parasites, in form of *sporozoites*, into the bloodstream. These micro-organisms are then accumulated in the human liver where, during the next seven to ten days, depending on the species of *Plasmodium*, asexually multiply themselves generating a more mature form, said *schizonts*, each of

produces many daughters, called *merozoites*. At this stage, there's no evident symptom yet. After it, *schizonts* break their host hepatocytes (i.e. cell of the liver) so that *merozoites* are released into the bloodstream.
From now on, the so-called *human blood stage* starts, in which symptoms of malaria, such as fever attacks and headaches, become manifest. *Merozoites* are now able to infect red blood cells (RBCs), also said erythrocytes, leading to the *erythrocytic schizogony*, during which there's another asexual and cyclic reproduction (*intra-erythrocytic cycle*): in this phase the parasite passes through three stages that are very useful to the clinicians to study the evolution of the disease. Represented in Fig.4: *ring*, *trophozoite* and *schizont* [13]. During the intra-erythrocytic cycle, the parasites degrade cytoplasm and hemoglobin of the RBCs to sustain their multiplication. Along with this process, in their digestive vacuole, there's the accumulation of free-heme, a by-product toxic to the parasite and that, for this reason, is converted into *hemozoin*, an insoluble bio-crystal with particular physics properties such as paramagnetism (see section I.2.1). After the *schizonts* are formed, they break and deliver the *merozoites* which determine the lysis of the infected erythrocytic membrane (i.e. lysis of the RBC). *Merozoites* infect others RBCs and restart a new intra-erythrocytic cycle. This cycle is regular and lasts 48 hours for *P. falciparum*, *P. vivax* and *P. ovale* while it lasts 72 hours for *P. malariae*: each periodic start corresponds to a typical fever attack. In *P. vivax* and *P. ovale* infections, some *sporozoites* can remain quiescent in hepatic cells for several months or even years and then reactivate (*hypnozoites*); similarly, with *P. falciparum* and *P. malariae*, there's a dormant phenomenon, but in this case parasites stay always in bloodstream.
After many cycles, *merozoites* develop into erythrocytic sexual forms of the parasite, called *gametocytes*, which are the precursors of *gametes* and circulate in the bloodstream. These are the primary cause of persistence of *Plasmodium*: humans represent the reservoir of *gametocytes*, till to one year after a malaria attack, from which mosquitoes procure them. The *micro-gametocytes* (male) and the *macro-gametocytes* (female) are ingested by the *Anopheles* during the blood meal and, from this event, the *sporogynic cycle* (i.e. sexual cycle) takes place. In mosquito's stomach, *gametocytes* exit from host RBC generating motile and elongated *zygotes* called *ookinetes* which later develop into *oocysts*. The latter grow up and eventually break their membrane, thus releasing *sporozoites* that are guided into mosquito's salivary glands. During mosquito's bit, inoculation of *sporozoites* into human perpetuates the malaria life cycle.

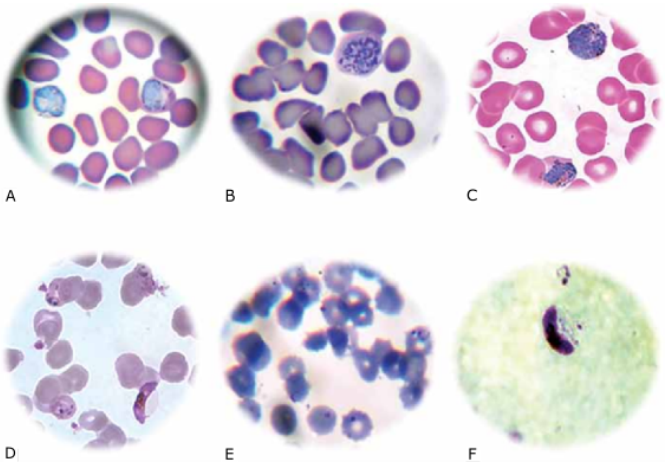

FIGURE 4. *Different stages of malarial parasites in thick smear: (A) trophozoites of P. vivax, (B) schizont of P. vivax, (C) gametocytes of P. vivax, (D) gametocytes of P. falciparum, (E) ring stage of P. falciparum and (F) gametocytes of P. falciparum, [13].*

I.2.1. Hemozoin. Before starting, hemoglobin is the iron-containing oxygen-transport protein present in RBCs [14]. Briefly, its complicated structure is shown in Fig.5A, where in blue and red are represented the protein sub-units, whereas in green the iron-containing *heme groups*. A heme group (see Fig.5B) consists of an iron ion held in a heterocyclic ring, known as a *porphyrin*.

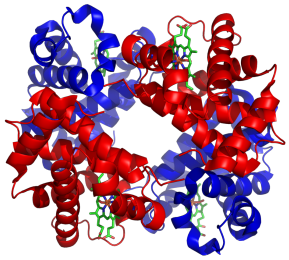

(A)

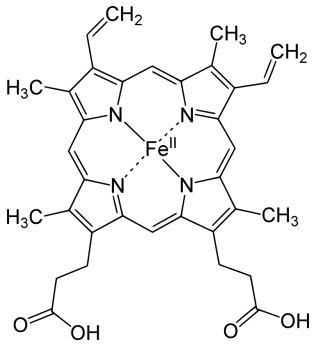

(B)

FIGURE 5. *(A) Structure of human haemoglobin: in red and blue the protein sub-units, while the iron-containing heme groups are in green. (B) Heme group structure, [15].*

As previously anticipated, during the intra-erythrocytic cycle, parasites consume up to 65% of host RBC hemoglobin, whose digestion releases *free heme groups* which oxidize generating a toxic compound: *ferriprotoporphyrin IX* (also *hematin*) [16]. This organic complex, consisting of an iron atom at the center of a porphyrin ring, is highly oxidizing: it is a pro-oxidant and catalyzes the production of reactive

oxygen species which, under environmental stress (e.g. UV or heat exposure), can damage cell structure [17]. By consequence, *Plasmodium* eliminates it throughout the bio-crystallization of hematin inside the digestive vacuole, converting it into inert and inorganic β-hematin crystals, also said *hemozoin*. *Hemozoin* is also known as the *malaria pigment*.

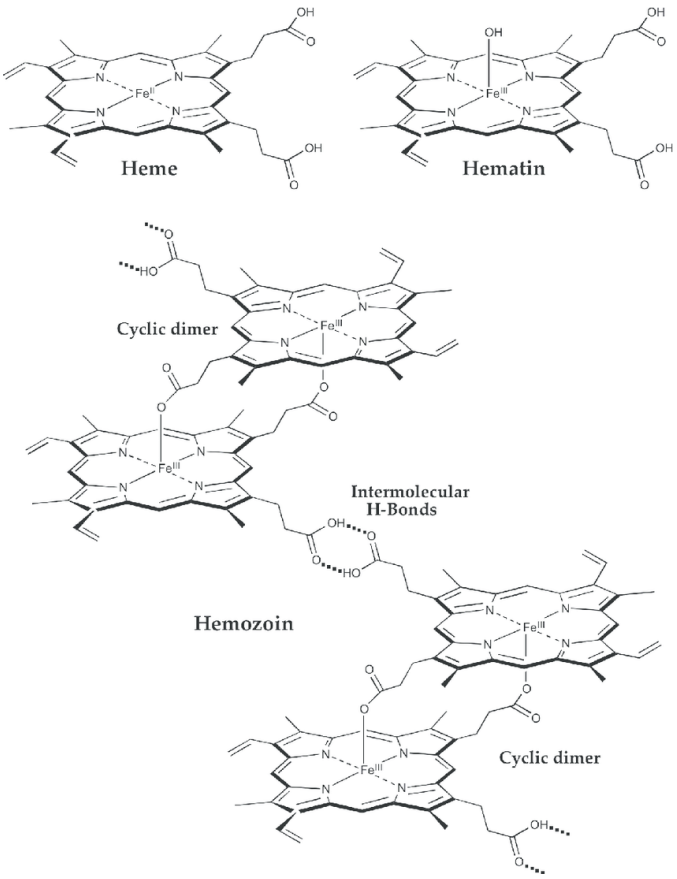

FIGURE 6. *Chemical structure of heme, hematin, and β-hematin or hemozoin, [18].*

Hemozoin crystals (see Fig.6) are made of dimers of hematin molecules which are linked by hydrogen bonds to form larger structures. Within each hematin, its central ferric ion Fe^{3+} is connected, in turn, to the oxygen of the carboxylate ($RCOO^-$) side-chain of the adjacent hematin through an iron-oxygen coordinate bond.
In oxyhemoglobin, i.e. when hemoglobin is linked to oxygen molecules, iron is in *ferrous* state Fe^{2+} and here all electrons are paired, giving a low-spin state (S=0) and diamagnetism occurs. On the other side, since a transition in valence number takes place thanks to bio-cyrstallization, in hemozoin, iron is in *ferric* state Fe^{3+}, such that unpaired electrons results in high-spin state (S=5/2) and, as demonstrated by Pauling, it is *paramagnetic* [19] (see section II.2.1).

Several mechanisms have been proposed for the production of hemozoin in *P. falciparum*, and the topic is still highly controversial, with membrane lipids, proteins or even a combination of the two, being proposed to catalyse the formation of hemozoin [20, 21]. Even though the mechanism of its formation remains uncertain, because of its importance to the parasite survival inside the erythrocyte, hemozoin has been the subject of intensive physicochemical and crystal studies. *Hemozoin crystals* have a brick-like structure (1:1:8), are about 50-1000 nm long [22], depending on the protozoan species, and each of them contains about 80000 heme molecules [23]. They present a typical dark bluish or brownish pigment and exhibit several remarkable physical properties: in particular *paramagnetism* and *optical birefringence* [24]. The spectroscopic and crystallographic analysis indicate that the hemozoin crystal structure is identical to that of a synthetic bio-mineral, called *synthetic β-hematin*. Its magnetic properties have been determined with electron paramagnetic resonance (EPR) and Mössbauer spectroscopy showing the same high-spin configuration (S=5/2) of its natural counterpart [25, 26]. Anyway, as shown in Fig.7 [27], synthetic β-hematin crystals are morphologically different, since their typical size ranges from 50 nm to 20 µm with a much wider dispersion with respect to hemozoin [28].

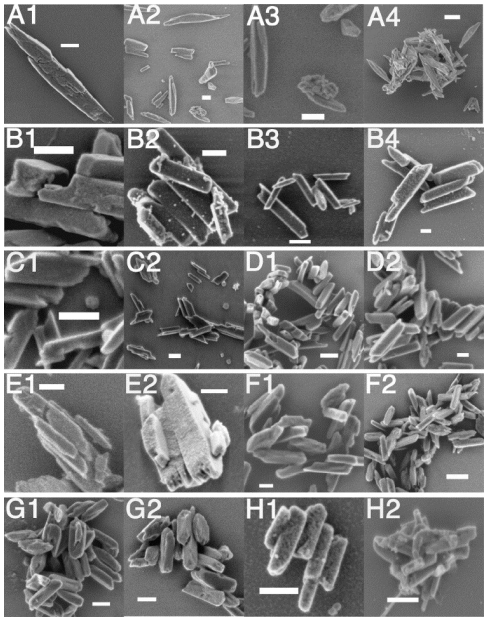

FIGURE 7. *Electron micro-graphs shows heterogeneity of shape and size for synthetic β-hematin and Plasmodium hemozoin. Several different SEM images of β-hematin (A) compared to that of hemozoin from P. falciparum (B), from P. vivax (C),P. ovale (D),P. malariae (E),P. brasilianum (F),P. knowlesi (G), and P. yoelii (H). The size bar is 200 nm, [27].*

The image above shows the morphological difference between synthetic crystals and natural hemozoin: the former one has a more elongated shape and a less cubical aspect with respect to the other one. Moreover, hemozoin from the mammalian

Plasmodium species is more brick-like with smooth sides at right angles [27]. The number and the size of the *hemozoin crystals* in the erythrocyte depend on the stage of the parasite development, with the lowest amount of the crystals detected in the *ring* stage and the highest amount in the *schizont* stage [25].

I.3. Diagnosis of malaria

Prompt and accurate diagnosis is critical to the effective management of malaria [2]. The global impact of malaria has stimulated the development of effective diagnostic strategies not only for resource-limited areas where malaria is endemic, but also in developed countries, where malaria diagnostic expertise is often lacking [29, 30]. The low specificity of signs and symptoms of malaria is the first problem. Typically patients go to the hospital because they have got a fever; discovering its origin requires the use of a diagnostic test, whose efficacy is limited by many factors. Although malaria diagnostics has a long story, the efficacy of currently available diagnostic tests, is limited by many factors. First of all, the peculiarities of the five *Plasmodium* species at the different stages of erythrocytic schizogony, require the development of specific tests. Secondly, the low value of *parasitemia* (i.e. the most used quantifier for the analysis, given by the percentage of infected RBCs with respect to healthy ones, see later) and the presence of other corpuscles in whole blood are serious obstacles to the detection of infected RBCs or their biomarkers. There are then others subtler aspects that can influence the identification and interpretation of malaria in a diagnostic test: persisting viable or non-viable malaria in endemic areas, where people can live with a lot of parasites without revealing any symptoms, sequestration of the parasites in the deeper tissues, drug resistance are just some examples [30]. Improper or unclear diagnostics can lead to presumptive antimalarial treatment, which can generate a recrudescence of drug resistance [29, 31].
From this analysis it is clear that, engineering an accurate and, if needed, panplasmodic, diagnostic test would solve many problems related to malaria and its eradication. Apart from these fundamental issues, the choice of the test must consider (i) where it is intended to be used, underdeveloped tropical countries or European countries, and (ii) who is going to use it, under-trained medical staff or experienced laboratory technicians. In particular, for endemic zones, the diagnostic system, to achieve a wide distribution, has to be user-friendly and cheap.
Before deeply explaining the principal techniques, currently available or under development, it can be beneficial to illustrate the indicators which are used to compare them [32]:

- *Sensitivity*: also called *true positive rate*, it represents the percentage of correctly identified diseased patients. To evaluate it, we should calculate the ratio between true positive and actual sick cases given by the sum of true positive (TP) and false negative (FN):

$$Sensitivity = \frac{TP}{TP + FN} \tag{I.1}$$

- *Specificity*: also called *true negative rate*, it's the ability to determine the healthy cases properly. To estimate it, we should calculate the ratio of true negative (TN) with respect to healthy cases, which is obtained by

summing true negative (TN) and false positive (FP):

$$Specificity = \frac{TN}{TN + FP} \tag{I.2}$$

- *Accuracy*: it exhibits the ability to rightly differentiate the sick and healthy cases. It corresponds to the ratio between the sum of correct tests and all performed tests:

$$Accuracy = \frac{TN + TP}{TN + TP + FN + FP} \tag{I.3}$$

- *Limit of Detection (LoD)*: it expresses the smallest variation of the physical quantity we're measuring. In malaria diagnostic tests, it is the smallest value of detectable *parasitemia*.
- *Parasitemia* ($\boldsymbol{P}$): it's the quantitative content of parasites in the blood. Apart from the important numerical value itself, it permits to have something more than a binary result and also to monitor the evolution of the disease. Its value is given by the ratio of parasite-infected red blood cells (i-RBCs) and total RBCs, or the volume of solution they're immersed in. So, in the former case it's a percentage (%), while in the latter one as the ratio between the number of i-RBCs and the volume (parasites/µl). Assuming the conventional value of RBCs/µl of $5 \cdot 10^6$, we can pass from one definition to the other one: for example a parasitemia of $1\% = 5 \cdot 10^4$parasites/µl.

In this section, several types of approaches involved in diagnosis of malaria will be presented. The conventional methods used for malaria diagnosis are *microscopy using blood smears* (simpler "microscopy"), *Rapid Diagnostic Tests* (RDTs) and *Polymerase Chain Reaction* (PCR). Currently there are several approaches in development, some that are just an upgrade of conventional tests, others exploiting different physical properties such as fluorescence, dielectrophoresis, vapor nanobubbles and magnetism [30, 33, 34].

I.3.1. Microscopy. Microscopic examination of slides for presence of malaria parasites has been the *gold standard* for malaria diagnosis since it was first introduced nearly 100 years ago. There exist two kinds of microbiological diagnosis: thin and thick blood smears. In both cases, blood needs to be collected preferably from peripheral capillaries where concentration of *Plasmodium* is higher (e.g. finger or ear). Moreover, blood should be taken, if possible, during or after fever attacks, and before administration of drug. Usually, after sampling, the blood sample is mixed with anticoagulant, such as *EDTA* or *heparin*. The specimen then has to be analysed within three hours in order to avoid possible morphological changes due to anticoagulants.
Let's first analyse the *thin blood smear* method: in this case, after the preparation just explained, the blood drop is put on a slide and then another slide's edge is used to smear it such that a single layer of RBCs can be obtained. After this process, the sample is dried, fixed with methanol and colored. Typically, to get coloration of investigated cells, doctors use GIEMSA, Wright's of Field's stains [35]. It is then performed the actual analysis, whose execution depends on the specific laboratory; however, WHO provide some guidelines, among which the one that suggests to examine twenty-five different microscopic fields (ten if there's a high percentage of

parasites) [36].
Looking at the *thick blood smear* technique, on the other hand, three drops are needed. Then a blood spot is stirred in a circular motion with the corner of the slide, taking care not make the preparation too thick, and allowed to dry without fixative. After drying, the spot is stained with diluted GIEMSA (1:20, vol/vol) for 20 minutes, and washed by placing the film in buffered water for 3 minutes. The slide is allowed to air-dry in a vertical position and examined using a light microscope [30]. With respect to the thin blood smear, here RBCs walls are ruptured during preparation of the sample. In this case the areas investigated are just the ones where there's already a certain evaluation of about 200 white blood cells (WBCs).
Microscopy is an established and relatively simple technique that is familiar to most doctors. Any laboratory that can perform routine hematology tests is equipped to perform a thin and thick malaria smear [37]. First and foremost, it can determine that malaria parasites are present in the patient's blood. Once the diagnosis is established, the microscopist can examine the smear to determine the malaria species and the percentage of the patient's red blood cells that are infected with malaria parasites. Thin films are similar to usual blood films and allow species identification because the parasite's appearance is best preserved in this preparation. Thick films, on the other side, since they screen a larger volume of blood, are more sensitive than the thin films, allowing the microscopists to appreciate low levels of infection. By the way, in the latter case, the appearance of the parasite is much more distorted and therefore, distinguishing between the different species, can be much more difficult. With the pros and cons of both thick and thin smears taken into consideration, an accurate diagnosis would require the use of both methods [35]. Clearly, the reliability of microscopy results is based on the procedures adopted in the laboratories performing the tests and it follows that, to avoid misdiagnosis, several conditions must be satisfied: presence of central coordinators to oversee quality assurance, good training systems in place based on competency relevant to clinical settings, regular retraining and grading of competency, an adequate budget for tools maintenance etc.
Microscopy involves an upfront purchase of microscopes (good quality microscopes from leading suppliers cost US$1000–1500), ongoing training, and purchase of relatively inexpensive reagents [33]. However, the main drawbacks, assuming a skillful and well-trained microscopist is available, remain the need of light microscope with 1000× magnification and the time needed for a single diagnosis, which is about 30-60 minutes. The limit of detection (LoD) in fieldwork is in the range 50-100parasites/µl, whereas an expert microscopist in a laboratory equipped with state of the art microscopy tools can attest around 5 to 10parasites/µl [34].
The discussion above indicates that, even if microscopy analysis of blood films is still considered the *gold standard* for malaria diagnostic, it presents some critical problems. That's why others methods emerged in the last years: some are just an upgrade of already existing microscopy test with automatic smear preparation, staining or slide-reading; others provide a completely different approach.

I.3.2. Rapid Diagnostic Test. Malaria Rapid Diagnostic Tests (RDTs) perform the diagnosis of malaria by detecting malaria bio-markers in human blood evidences, in particular antigens [2]. RDTs permit a simple and reliable detection of malaria infections, particularly in remote areas, where skilled technicians to evaluate blood films are not available, and there's a limited access to good quality microscopy services. Moreover, RDTs are portable, disposable, easy to be interpreted and provide results of diagnosis rapidly.
Malaria RDTs employ antibodies to detect specific antigens, which are proteins produced by malaria parasites. Some RDTs detect a single species (*P. falciparum* or *P. vivax*), some are pan-malaria (*P. falciparum*, *P. vivax*, *P. malariae* and *P. ovale*) and some further distinguish between *P. falciparum* and non *P. falciparum* infection, or between specific species [2, 33].
RDTs are lateral flow immuno-chromatographic antigen-detection tests; they rely on the interaction between a treated-membrane, covered by proper antibodies (e.g. HRP-II for *P. falciparum*), and the whole blood sample. Blood for the test is commonly obtained from a finger-prick and then it is mixed with a lysing agent: the latter breaks the RBCs membrane, releasing more antigens. During the test, as long as the mixture moves through the so-called "RDT cassette" (see Fig.8) thanks to capillary forces, it reacts with the dye-labeled antibodies of the membrane. If targeted antigen bio-markers are present, some labeled antibody-antigen complexes will be trapped and accumulate on the test line. If the thin test line is absent, it means that there's no antigen. In order to check that the test properly works, another control-line is always present. Typically, results of the test are available within 15–30 minutes.

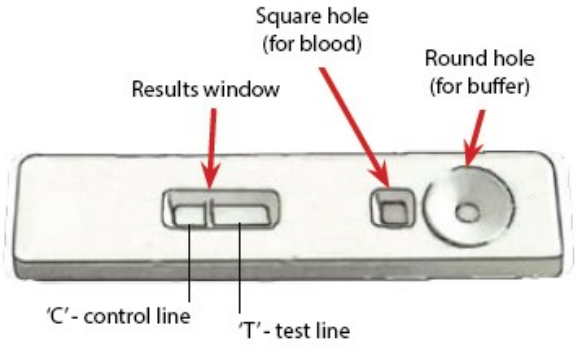

FIGURE 8. *Inside the cassette is a strip made of filter paper and nitrocellulose. Typically, a drop of blood is added to the RDT through one hole (square hole) and then a number of drops of buffer usually through another hole (round hole). Buffer carries the blood along the length of the RDT, [37].*

The LoD of RDTs is attested at about 200parasites/µl [11]. In 2018, a comparison of microscopy and RDT [38] highlighted a significant difference between these two techniques, reporting, in the former case, a specificity of 81% and a sensitivity of 55% while, in the latter one, respectively 89% and 83%. Many others reviews about RDT relevant values have been performed throughout the years [33], always

attesting >90% sensitivity and >90% specificity. So, RDTs provide accurate diagnosis in circumstances where demonstration of parasitaemia has previously been impossible or where microscopy-based diagnosis may be unreliable. That's why in recent years, RDT testing has been significantly expanded around the world: manufacturers surveyed by WHO for the "World malaria report 2018" [2], reported a total of 276 million RDT sales in 2017. Most RDTs (66%) were supplied to sub-Saharan Africa. In 2017, an estimated 75% of malaria tests in sub-Saharan Africa were conducted using RDTs, up from 40% in 2010 [33, 37]. Although there are variations among the more than 200 malaria RDTs products on the market, the principles, timing and performances of the tests are similar.
Nevertheless, this technique still has several limitations. In specific geographic regions there's a variation in the expression of antigens (i.e. variation in the number and arrangement of the genes coding) such that false negatives can occur. Then, LoD is not adequate for reliable detection of very low-density infections in asymptomatic individuals and, on the other hand, high concentration of antigens may also result in false negatives due to the "prozone effect" (i.e. an excess of antigen) [39]. Moreover RDTs are at risk of deterioration and reduced sensitivity when they're exposed to heat and humidity for prolonged periods: their stability is assured in the range from 4 to 40°C for 18-24 months [33]. Finally, RDTs are not able to quantify parasite density which is useful for monitoring a patient's response to treatment and is at times used, along with clinical symptoms, to assess the severity of illness. Several efforts are under way to improve existing RDT technologies, for instance using fluorescent dyes to improve the LoD or moving to urine based malaria rapid tests [33].

I.3.3. Nucleic acid detection. Nucleic acid detection refers to the detection of parasite genes (DNA/RNA) in a sample. These laboratory techniques, developed in the past 25 years, are highly sensitive, capable of detecting nucleic acid in minute quantities (down to a single molecule in a specimen) and, as a result, have revolutionized diagnostic medicine in many fields. With respect to malaria, several highly sensitive techniques for detecting the nucleic acid of the malaria parasite have been developed: the following discussion focuses on *Polymerase Chain Reaction (PCR)* and *Loop-Mediated Isothermal Amplification (LAMP)*.

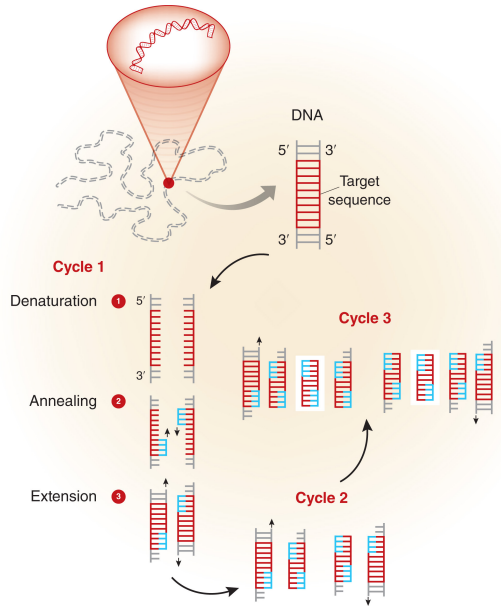

FIGURE 9. *Steps of PCR: (1) the DNA template is heated to 94°C and this breaks the weak hydrogen bonds that hold DNA strands together in a helix, allowing the strands to separate creating single stranded DNA. (2) The mixture is cooled to anywhere from 50-70° C. This allows the primers to anneal to their complementary sequence in the template DNA. (3) The reaction is then heated to 72° C, the optimal temperature for DNA polymerase to act. DNA polymerase extends the primers, adding nucleotides onto the primer in a sequential manner, using the target DNA as a template.*
With one cycle, a single segment of double-stranded DNA template is amplified into two separate pieces of double-stranded DNA. These two pieces are then available for amplification in the next cycle. As the cycles are repeated, more and more copies are generated and the number of copies of the template is increased exponentially, [40].

PCR based tests detect malaria parasites in a blood sample by multiplying the nucleic acid present in the sample. This process, called amplification, is accomplished through the use of special reagents that catalyse gene replication and through precise control of the environment in order to create favourable conditions for the reactions (see Fig.9). In one cycle of PCR, it is theoretically possible to double the amount of target gene present; the cycle is typically repeated several times to produce large quantities (e.g. millions of copies) of the target gene. The product of this amplification process is then analysed for the presence of malaria using a variety of detection methods. PCR is able to detect extremely low parasite densities, generally surpassing today's microscopic and antigen detection methods in sensitivity and specificity. With regard to LoD, PCR can detect as few as 1parasite/µl of blood (using a finger-prick sample) as compared to 50–100parasites/µl for microscopy or RDTs. Using higher volumes of blood (e.g. venous-blood rather than finger-prick),

researchers have developed ultrasensitive PCR with a LoD of 22parasites/ml [41]. Generally, PCR requires a very well-equipped laboratory and technicians trained in molecular biology. In addition to the upfront investment in laboratory infrastructure, equipment and training for technicians, PCR is also several times more expensive than microscopy and RDTs [42]. As a result, malaria PCR is used for research, epidemiological surveys and as a reference standard against which other methods are evaluated. Even in facilities with PCR capacity, it is not always used to diagnose patients, as the results are not immediately available to the clinician and it is expensive. Nevertheless, PCR is extremely useful to investigate complex cases; for example, to establish species after diagnosis has been made with microscopy or RDT. There are three main types of malaria PCR: *conventional* PCR in which result is qualitative; *nested* PCR which uses two rounds of amplification one for pan-malaria genes and another for a specific gene; and *real-time* PCR which provides also a quantitative result.
On the other hand, there's *LAMP* approach: it is a recent diagnostic test which uses isothermal DNA amplification technology, whereby parasite DNA is amplified at a stable temperature and the by-products of amplification are detected based on changes in turbidity or emission of a fluorescent signal. The fact or working at a fixed temperature, without the thermal cycles typical of PCR, is the main advantage if this technique, especially in view of on-field usage. As for PCR, the LAMP procedure begins with a sample preparation step to extract DNA, followed by amplification and detection of DNA through reaction at a constant temperature using simple instruments such as water bath. During the process, large quantities of DNA are amplified, enabling simpler end-point detection as compared to PCR methods. In addition, the DNA sequences are amplified in such a way that the products fold into a looped structure causing the reaction mixture to appear turbid. Following amplification, detection is conducted through various methods: fluorescence detection or turbidity measurements. Recent works suggest that LAMP can achieve sensitivity and specificity comparable to PCR and well above RDTs and microscopy. Nevertheless, LAMP remains intrinsically a qualitative technique.
Despite the advantages and high resolution seen, these nucleic acid detection methods present several factors that limit their use: high cost and sophisticated infrastructure needed, the lack of standardization methods and also limited availability of skilled technicians. Moreover, even if this problem is reduced with LAMP, a lot of time per sample is requested every time, at least on the order of 45 minutes [33, 41, 43]. Last but not least, apart from real time PCR, these tests are not always quantitative. In the past years, the principal efforts to improve these techniques have been dealing with the simplification of sample preparation (i.e. purification of DNA away from other sample components), the standardization of procedures and the attempt to reduce costs. By the way, so far DNA based diagnostic tests are widely used within well-equipped laboratories and we haven't seen a wide spreading in endemic regions.

I.3.4. Fluorescent microscopy. *Fluorochrome staining* to detect malaria parasites in blood films is more sensitive, is easier to do, and is less time-consuming than GIEMSA staining [37]. However, standard illuminated mercury vapour fluorescence microscopes are expensive, especially for tropical countries where malaria is endemic. Fluorescence microscopy with a standard light microscope and a new

interference filter specially designed for the fluorochrome stain, *acridine orange*, was used to detect malaria parasites in thick and thin blood films. In this system two fluorescence colours, green for nuclei and red for cytoplasm, were emitted from stained parasites. Thick and thin blood films from patients with malaria were examined with this system. This system actually helps the identification of parasites leading to a sensitivity around 90% even for low values of parasitemia (100parasites/µl), otherwise difficult to reach. Nevertheless, the typical issues of microscopy (e.g. operator dependent diagnostic, need for a bulky microscope, long operation time, etc.) still affect this version of the gold standard.

I.3.5. Serology and spectroscopy. Here we briefly analyse two uncommon techniques which, anyway, represent an interesting different point of view.
Malaria serology refers to the use of antigens to detect malaria antibodies, which are a marker of exposure to malaria, as seen with RDTs [3]. Although initially developed as a diagnostic test, nowadays they're not used to detect malaria for two reasons: first, it's not possible to distinguish between current and past infections; secondly, antibodies to malaria parasites are not present during the acute phase of a infection, but they appear several days later. Serology tests for malaria are, however, used to detect exposure to malaria, because antibodies to malaria parasites remain in the body long after an infection has been cleared [33]. In particular three main applications have been found for this technique: (i) screening blood donors to avoid transfusion-induced malaria when the donor's parasitemia may be below the detectable level of blood film examination, (ii) testing a patient, usually from an endemic area, who has had repeated or chronic malaria infections, (iii) testing a patient who has been recently treated for malaria but in whom the diagnosis is questioned [37].
Spectroscopy involves the absorption of particular wavelengths of electromagnetic radiation by molecules in a sample. The unique way through which molecules interact with light is used to classify and characterize the sample. Depending on the source exploited, different types of spectroscopy can be done resulting in different information. There are no platforms that currently use spectroscopic approach, but some of them are in development stage [33]. For example, it can be used a biomarker that is present across all *Plasmodium* life stages: lipids. The parasites have a unique set of lipids in their membranes, which produce a characteristic IR signature corresponding to the stretching of C-H bonds in their hydrocarbon chains. After having acquired the blood and spiked the red blood cells, to the sample is added a bit of methanol to break down the blood cells membranes, releasing the parasites and making them easier to detect. The entire process, from sample preparation to collecting a spectrum, takes just minutes. The spectra of parasite-spiked blood cells differs from those of blood cells alone in the C-H stretching region. These intensity differences and shifts in certain signals also distinguishes samples with parasites at early life stages from the others. So, using a statistical algorithm, the researchers can determine whether a spectrum corresponded to an infected sample [44].

I.3.6. Hemozoin detection. As seen in section I.2.1, malaria parasites produce hemozoin crystals (HCs). Even though hemozoin was discovered and linked to malaria in the 1800s [33], initially it has not been used to diagnose malaria. Moreover, while it is possible to see hemozoin in certain stages of the parasite's life cycle using microscopy, it is not always detectable with traditional microscopy.

Although the technologies under development differ in the approach, the methods exploit two of the main physical properties of HCs: dichroism and magnetism. With the former case, scientists take advantage of the way in which they interact with light, as described by birefringence; in the latter one, instead, is used the magnetization due to unpaired electrons of Fe^{3+} atoms.
Most of the hemozoin-based tests are designed to be hand-held devices that only use finger-prick blood sample. These kinds of tests are usually very fast compared to the previous one, giving the results in about 5 to 10 minutes [33]. Moreover, as it follows by WHO statement [2], these new technologies must try to be suitable in endemic regions where infrastructures and well trained personnel are missing. Even if the target used to diagnose malaria here is always hemozoin, there are several technologies with as many different performances.
Magneto-optical technology (MOT): this test involves applying a magnetic field to the sample, causing alignment of any hemozoin crystals present. Then the device compare the transmittance of a polarized laser before and after the application of the magnetic field to the sample. A photodetector measures the change in transmittance of light that would indicate the presence of hemozoin and finally a microprocessor interprets the change in light providing the result to the test operator. Time needed is just 1 minute, sensitivity is about 90% and the LoD is still high, attested at 100 parasites/µl. It's important to underline that before the analysis, the sample has to be mixed up with a lysing agent to disperse hemozoin [33].
Several techniques exploit paramagnetic properties not only of hemozoin itself, but also of host RBCs. These can be attracted with an *high gradient magnetic separation method (HGMS)* [45]. For example, RBCs with enough malaria parasites, since they act as paramagnetic particles, can be moved toward high magnetic field regions [46]. Another similar approach is represented by *MACS (magnetic-activated cell sorting)*: superparamagnetic nanoparticles are coated with antibodies that can be attached to antigens typically expressed by targeted cells. After mixing the cells and the beads in a solution, they're transferred to a magnetic column. Now, cells attached to the magnetic nanoparticles stay on the column, while other cells, which are not expressing the antigen, flow through. It follows that the cells can be separated positively or negatively with respect to the particular antigen [47]. These last two methods, nevertheless, still need a microscope for evaluation and quantification.
Then, others more complex and promising methods exist, such as a *magnetic resonance relaxometry system (MRR)* or non invasive tests where blood sample is obviated, collecting information just through the skin [33, 48].

From this brief introduction it comes out that, despite the strong efforts to eliminate malaria and the technological improvements made, there are still growth margins both in drugs field either in diagnostics one. Exactly in this context *TMek* was born.

I.4. TMek

TMek comes from *"Tid Mekii"*, the name of "malaria" in the local language of Mbalmayo, the small village of Cameroon where the first preclinical validation of the test has been carried out.
The idea of TMek is to design a novel diagnostic test with the following prerequisites: it has to be compact, low-cost, user-friendly, pan-plasmodic and, above all, more rapid and, at least, as sensitive as *gold standard microscopy*. In order to do that, two physical principles are used: *magnetophoretic separation* and *electrical impedance spectroscopy*. We first exploit magnetic field gradient to attract the targeted particles in specific areas where sensitive electrodes are placed such that a variation in resistance occurs; the targeted particles are host i-RBCs and hemozoin crystals. This is a lab-on-chip approach: therefore, all the measurements are done thanks to a silicon chip with nickel pillars acting as magnetic concentrators, on top of which, gold electrodes are deposited.

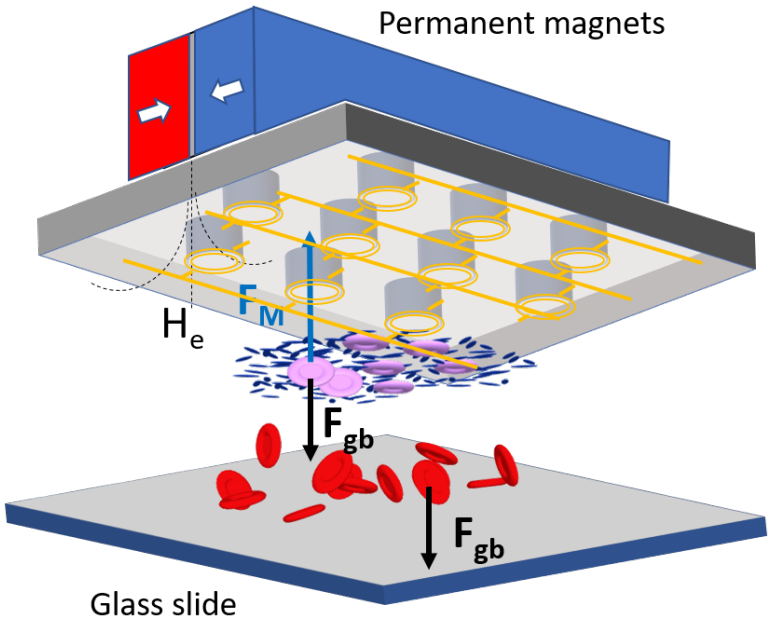

FIGURE 10. *TMek schematic concept in horizontal configuration: i-RBCs (pink) and HCs (black) are attracted towards the chip, while healthy h-RBCs (red) sediment.*

After the blood sample is diluted with a solution made by *phosphate buffered saline (PBS)* and an anticoagulant (e.g. *EDTA*), it is placed in a cell defined by a glass slide and a *PDMS* gasket put in contact with the sensitive part of the chip. Several configurations during the analysis are possible: we can pass from the horizontal one (i.e. surface of the chip parallel to the ground plane) to the vertical one (i.e. surface of the chip perpendicular to the ground plane), exploring also intermediate angles (see Fig.10). In any case, the same forces will play

a role: magnetic, gravity, buoyancy and drag forces. In particular, the magnetic force is provided, macroscopically, by permanent NdFeB magnets and, locally, by Ni pillars. The resulting total force permits the paramagnetic particles to be attracted to the sensitive areas of the chip, whereas other diamagnetic corpuscles will sediment. Paramagnetic particles will then induce a variation in resistance of the chip-circuit and the signal can be detected with an electronic system, composed by a trans-impedance amplifier and a LIA (i.e. lock-in amplifier), and transferred to a computer where it will be analysed with MATLAB software.
Four main features can be highlighted to describe and define the state of the art of TMek:

(1) it allows a direct *quantitative analysis* studying the amplitudes of the signals
(2) has a *timing of execution* around 10 minutes
(3) *Limit of Detection* of 10parasites/µl
(4) presents the possibility to distinguish *different stages* of the parasite life cycle looking at the dynamics of the signal

There are still unexplored margins of growth for TMek, but all the improvements are oriented to satisfy the requirements stated by the World Health Organization in its guideline report "*New Perspectives: Malaria Diagnosis*" [49]:

- *Compact, easy to use and cheap*
- *Limit of Detection* in the order of 10parasites/µl such as *gold standard*
- Aiming 100% of *sensitivity* for densities of >100 parasites/µl in all species
- Reduction in the number of steps and test components
- Reduction or suppression of *time-critical steps* (10 minutes)
- Develop methods that permit *quantification* of parasite density

For the aforementioned project's idea, two patents have been deposited. Moreover, TMek won the *Polisocial award* in 2017 and was one of granted projects of *Switch to Product* context of "Politecnico di Milano" in 2018.

I.5. Outlook of the thesis

This thesis work is part of the TMek project, whose aim is to develop a rapid, accurate, quantitative, easy to use and low cost diagnostic test for malaria. It relies the previous feasibility and magnetophoretic studies performed by the same research group and summarized in previous Master's thesis [50, 51]. The experimental activities have been performed in *PoliFAB*, the micro and nanotechnology center of the "Politecnico di Milano", under the supervision of Prof. Riccardo Bertacco, head of the *Nanomagnetism for Biology and Spintronics* group of the Department of Physics, and in *"Luigi Sacco" hospital* in Milan. The detection system has been developed in collaboration with the I^3N group of "Politecnico di Milano", directed by Prof. Marco Sampietro and Prof. Giorgio Ferrari, that designed, fabricated and characterized the electronics of the device. The blood samples used in the calibration tests have been provided and treated by *µBS Lab* of "Politecnico di Milano", led by Prof. Gianfranco B. Fiore. The prevalidation campaign has been carried out in the diagnostic laboratory of *Hôpital Saint Luc* of Mbalmayo in Cameroon.
During this thesis, different areas of knowledge and competences have been involved. First, the realization of a MATLAB code aimed to analyse the signals detected by the system. Then, several type of tests have been executed to characterize the

system. After the analysis of data related to the prevalidation campaign it was time to design and fabricate the new microchip. Finally, the new chip has been characterized and used to perform a further optimization of the overall system. These results, together with the previous, constitutes the basis for the next step: the realization of a completely reliable and drift-free rapid diagnostic system.
Here, an overview of the chapters is presented:

- **Chapter 1: Introduction.** This chapter reports the main aspects of malaria, focusing on its biology and the diagnostic tests currently used. There is also a summary of what TMek is and its principal physical concepts.
- **Chapter 2: Theory.** The theoretical aspects underlying the device are presented. First, a focus on magnetism and the forces acting on a particle in a fluid is shown; then, the focus shifts on the basic principles of impedance detection to better understand the diagnosis mechanism.
- **Chapter 3: Experimental techniques and methods.** This part concerns the design and fabrication of the new chip. Later on, there is a discussion about electronics involved in the device; finally the overall system, and the analysis software as well, are explained.
- **Chapter 4: Experimental results.** The chapter presents the experimental results obtained during the thesis work. Before starting, the protocol and the main noises terms are presented.
- **Chapter 5: Conclusions and perspectives.** This section summarizes the main results of this thesis work and opens up new perspectives and ideas for the TMek project.

CHAPTER II

Theory

In this chapter we will deeply focus on the physics that underlies the TMek project. First there is an explanation of the principles of micromagnetism necessary to understand the design of magnetic concentrators and the force on a blood corpuscle. Then, all the forces acting on the corpuscles are taken into account, in order to explain magnetophoretic separation in its entirety. The final section of the chapter is devoted to the explanation of electrical impedance detection principles.

II.1. Micromagnetism

The fundamental entity in magnetism is the *magnetic moment* $\boldsymbol{\mu}$. A magnetic solid consists of a large number of atoms with magnetic moments and the *magnetization* vector $\mathbf{M(r)}$ is defined as the magnetic moment per unit volume. In condensed matter, magnetization $\mathbf{M}$ is related to the magnetic field $\mathbf{H}$, meaning $\mathbf{M(H)}$. Taking into consideration all the physical interactions existing in magnetic solids is not easy, in fact four main energetic terms are present: *magnetostatic energy, exchange energy, crystal anisotropy energy* and *Zeeman energy.* To get the final equilibrium configuration, it's necessary to minimize all these energy contributions. What is usually done to tackle the problem, is exploiting the continuum theory of *micromagnetism* [52].
Micromagnetism is the field of physics dealing with the prediction of the magnetic properties of matter at micro-metric and sub-micrometric scale, as for *ferromagnetic* Ni pillars fabricated in the chip. The theory of micromagnetism was developed in the late 1950s by Brown [53] and its purpose is the calculation of the magnetization distribution as a function of the applied field, taking into account the structure of the material and the mutual interactions between the different parts of a body. It's a quasi-classical theory in which spin operators of the Heisenberg model are replaced by classical vectors; moreover it states, as fundamental assumption, that the spin direction changes only by small angles from one lattice point to the next [54], so the material can be divided in small volumes whose magnetization is uniform. The characteristic length scale of these volumes is the so-called *exchange length* and it must be: (i) large enough to replace discrete atomic spins by a continuous function of position like $\mathbf{M(r)}$ and (ii) small enough to investigate the details of the transition of the magnetization between magnetic domains [54]. For 3d transition metal ferromagnetic materials this length scale ranges from nanometers to micrometers. Another important assumption within this theory, refers to the fact that relaxation time within each volume, is much smaller than one of the entire system. Let's now analyze each of the aforementioned energy terms.

II.1.1. Exchange energy. The exchange energy term has quantum mechanical roots. This energy term comes out from the interaction between magnetic spins, favouring a parallel configuration (*ferromagnetism*) or an anti-parallel one (*anti-ferromagnetism*), and it lies at the heart of the phenomenon of long-range magnetic order.
The exchange energy, E_{ij}, between two localized spins is:

$$E_{ij} = -2J_{ij}\mathbf{S}_i \cdot \mathbf{S}_j \tag{II.1}$$

where J_{ij} is the exchange integral between atoms i and j, representing a measure of the strength of the coupling; on the other hand $\mathbf{S}_i$ is the spin angular momentum of the atom placed in i-th position. For cubic metals, such as Ni, $J_{ij} = J$. Treating the exchange energy for a large number of coupled spins, we regard E_{ij} as a classical potential energy and replace $\mathbf{S}$ by a classical vector. Let $\mathbf{m}$ be the ratio between magnetization $\mathbf{M}$ and the saturation magnetization M_s: so $\mathbf{m}_i$ is the unit vector in direction $-\mathbf{S}_i$ [54]. If ϕ_{ij} is the angle between the vectors $\mathbf{m}_i$ and $\mathbf{m}_j$, the exchange energy is:

$$E_{ij} = -2JS^2 \cdot cos(\phi_{ij}) \tag{II.2}$$

where $S = |\mathbf{S}_i| = |\mathbf{S}_j|$. Normally exchange interaction is short-ranged, thus only nearest neighbours can be taken into account. Keeping in mind this and the continuous approximation, we get that the overall exchange energy of the body is:

$$E_{ex} = \int_V A[(\nabla m_x)^2 + (\nabla m_y)^2 + (\nabla m_z)^2]dV \tag{II.3}$$

where A (J/m) is the *exchange stiffness constant* that indicates the strength of the interaction and its expression in cubic lattices is:

$$A = \frac{JS^2 n}{a} \tag{II.4}$$

In cubic lattices n is the number of atoms per unit cell ($n = 1, 2, 4$ respectively for simple cube, body centered cube and face centered cubic lattices) and a the distance between nearest neighbours.
The *exchange stiffness constant* A is connected to the fundamental aforementioned *exchange length* l_{ex} which is defined as the critical size for magnetization reversal by quasi-uniform rotation in particles. Moreover, l_{ex} describes the relative importance of the exchange energy with respect to the magnetostatic energy (see section II.1.2); it is mathematically expressed as:

$$l_{ex} = \sqrt{\frac{A}{\mu_0 {M_s}^2}} \tag{II.5}$$

where μ_0 is the *permeability of free space* and equals $4\pi \cdot 10^{-7} H/m$.

II.1.2. Magnetostatic energy. The *magnetostatic energy* is also called dipolar interaction energy: in a crystal, each moment $\boldsymbol{\mu}$ creates a dipole field and, in its turn, it interacts with the fields created by the others. Therefore, a long range interaction occurs and energy is stored for a given configuration moment $\mathbf{M}$. Summing the energy over all atoms, magnetostatic energy results:

$$E_{dem} = -\frac{\mu_0}{2}\int_V \mathbf{M} \cdot \mathbf{H}_d dV \tag{II.6}$$

The term $\mathbf{H}_d$ stands for the *demagnetizing field*, which is the magnetic field generated by the magnetization in a magnet. This name reflects the fact that it is antiparallel to the magnetization of the body. $\mathbf{H}_d$ gives rise to magnetic domains in macroscopic bodies and to *shape anisotropy*. For a magnetic material with surface defined by a second order equation, it can be written as:

$$\mathbf{H}_d = -N\mathbf{M} \tag{II.7}$$

where N is the *demagnetizing tensor*, highly influenced by the shape of the material, while $\mathbf{M}$ is the magnetization of the object. Magnetostatic energy is minimized when $\mathbf{M}$ tends to align to the longest axis of the body [55].

II.1.3. Crystal anisotropy energy. The magnetic properties of a ferromagnetic crystal are anisotropic. *Magnetocrystalline anisotropy* arises from the single-ion *crystal field* interaction between the aspherical electron cloud of the ion and the charge distribution surrounding it (i.e. the crystal field). In this context, the magnetocrystalline anisotropy is a consequence of the directional dependence of the energy of the charge cloud within the crystal field. The crystallographic direction associated with the energy minimum determines the easy magnetization direction along which the magnetic moment $\boldsymbol{\mu}$ preferentially orients with respect to the crystallographic axis [56]. To manage it, it's used the *crystal anisotropy energy density* $e_{AN}(\mathbf{m})$, which is a function of the reduced magnetization $\mathbf{m}$, so that $\mathbf{M} = M_s\mathbf{m}$. $e_{AN}(\mathbf{m})$ can be represented as a surface where the distance of each point from the origin identifies the value of the energy density for a given direction $\mathbf{m}$: the bigger the distance the less favourite will be that direction. From this perspective we can visualize the *easy* and *hard axis*.
For *uniaxial anisotropy*:

$$e_{AN} = K_0 + K_1 sin^2(\theta) + K_2 sin^4(\theta) \tag{II.8}$$

where θ is the angle between easy axis and the magnetization, while K_0, K_1 and K_2 (J/m^3) are the *anisotropic constants*. Keeping into account just the first two elements, if $K_1 < 0$ an *easy plane anisotropy* is achieved; on the other side, if $K_1 > 0$ we get an *easy axis anisotropy*.
The crystalline anisotropy energy is:

$$E_{AN} = \int_V e_{AN}(\mathbf{m}) dV \tag{II.9}$$

Another relevant physical quantity is the *anisotropy field* H_{AN} which is a fictitious field that mimics the strength of crystalline anisotropy. So, H_{AN} is the value of the external field necessary to saturate the magnetization along the *hard axis*:

$$H_{AN} = \frac{2K_1}{\mu_0 M_s} \tag{II.10}$$

II.1.4. Zeeman energy. The energy of a magnetic dipole moment $\boldsymbol{\mu}$ in an external applied magnetic field $\mathbf{H}_a$ is given by the scalar product $-\boldsymbol{\mu} \cdot \mathbf{H}_a$: the energy is minimized if these two vectors are parallel, i.e. the magnetic moments are

aligned with the external field. Summing up all the dipoles in a continuum model we obtain the *Zeeman energy* term:

$$E_{Zeeman} = -\mu_0 \int_V \mathbf{M} \cdot \mathbf{H}_a dV \tag{II.11}$$

II.1.5. Final configuration. Using all the energy terms analysed above, we get the total energy E_{TOT}:

$$E_{TOT} = E_{ex} + E_{dem} + E_{AN} + E_{Zeeman} \tag{II.12}$$

such that, explicitly:

$$\begin{aligned} E_{TOT} = \int_V \Bigg[\frac{A}{2}[(\nabla m_x)^2 + (\nabla m_y)^2 + (\nabla m_z)^2] + \\ + e_{AN} - \frac{\mu_0}{2}\mathbf{M} \cdot \mathbf{H}_d - \mu_0 \mathbf{M} \cdot \mathbf{H}_a \Bigg] dV \end{aligned} \tag{II.13}$$

The Brown's equation allows to find the equilibrium configuration of the magnetization within the body: this corresponds to the local minima of equation II.13 as mathematically demonstrated by Landau and Lifshitz [57]. Finding the solution is not easy since the phenomena described compete with each other. Exchange interaction tries to keep the magnetic moments $\boldsymbol{\mu}$ aligned with $\mathbf{M}$; magnetostatic interaction tends to orientate the spins in such a way that the demagnetizing field outside the body is minimized; magnetocrystalline anisotropy then favours the easy axis; finally the Zeeman energy term advantages $\mathbf{M}$ parallel to the external applied field. Considering these competing tendencies and the relative weights of them, different equilibrium configurations can arise, which means that a different pattern of the domain walls, to separate them, comes out.

II.2. Magnetic particles

As said in section II.1, a magnetic material has many magnetic moments $\boldsymbol{\mu}$ which concur to define the magnetization vector $\mathbf{M}$. In vacuum, since there is no body, magnetization is null, so:

$$\mathbf{B} = \mu_0 \mathbf{H}. \tag{II.14}$$

Here the two fields are parallel; $\mathbf{B}$ is measured in Tesla T, while $\mathbf{H}$ is measured in A/m in the S.I. of units.
In a magnetic solid, on the other hand, things get more complicated because we need to keep into account the magnetization of the body, such that $\mathbf{B}$ and $\mathbf{H}$ can have different directions:

$$\mathbf{B} = \mu_0(\mathbf{H} + \mathbf{M}). \tag{II.15}$$

Assuming to deal with a *linear material*, the magnetic field $\mathbf{H}$ is related to $\mathbf{M}$ through the dimensionless quantity χ, the *magnetic susceptibility*, i.e. $\mathbf{M} = \chi \mathbf{H}$. It follows that:

$$\mathbf{B} = \mu_0(1 + \chi)\mathbf{H} = \mu_0 \mu_r \mathbf{H} \tag{II.16}$$

where $\mu_r = 1 + \chi$ is the *relative permeability of the material*.
Looking at the behaviour of a body when an external field is applied, three main different cases can be spot:

- *Diamagnetism*: all materials show some degree of diamagnetism; it's a weak effect according to which the body presents a magnetization **M** opposite to the external applied field, this means that a diamagnetic particle tends to move away from a high field region, being the Zeeman interaction unfavorable. Even though it is a quantum mechanical effect, it can be viewed as a response of the magnetic moment of the material which opposes to the applied magnetic field that caused it. Here, χ has a small and negative value (i.e. $\mu_r < 1$). As will be displayed below, healthy RBCs and white blood cells display a diamagnetic behavior.
- *Paramagnetism*: paramagnetism is a form of magnetism whereby susceptibility is positive: an applied magnetic field induces a magnetization which aligns to the applied magnetic field which caused it. This feature is strictly related to the presence of *unpaired electrons*, such that the magnetic moment of the atoms is different from zero at variance with the diamagnetic case. Without an applied field, the magnetic moments will point randomly because the thermal agitation is dominant compared to the the weak interactions of neighbouring atoms (i.e. $\boldsymbol{\mu}$ are considered independent). On the other hand, the application of a magnetic field tends to align the magnetic moments and, as expressed by the *Langevin function*, the stronger the applied field, the stronger the alignment. Hemozoin particles are paramagnetic as discussed in section II.2.1.
- *Ferromagnetism*: while in the prior cases no magnetization was present, unless an external magnetic field was applied, in ferromagnetism there can be a permanent magnetization even if **H** is null. This is due to exchange interaction and it is linked to the phenomenon of hysteresis typical of ferromagnets where is also evident the relationship between applied **H** and magnetization: indeed, in this case, **M(H)** is not a single value function. In case of soft ferromagnets, with negligible coercivity and remanence, the linear portion of the M(H) curve can be described by $\mu_r >> 1$, thus, a strong attraction between the magnetic field and the body occurs [55].

II.2.1. Magnetic properties of hemozoin. Hemozoin, as seen in section I.2.1, is paramagnetic, which means that a hemozoin particle is attracted by a magnet. This is crucial because the fundamental physics underlying magnetophoretic technologies like *TMek*, relies on the possibility to disentangle magnetic bodies (i.e. hemozoin and i-RBCs) from non-magnetic ones (i.e. h-RBCs and other corpuscles). The paramagnetic property of HCs arises from the central iron Fe^{3+} (see section I.2.1) which is in the high-spin configuration due to five unpaired electrons $3d^5$, resulting in a spin angular momentum S=5/2; this was shown by experimental techniques such as EPR, magnetophoresis and magnetization studies [25, 22].
On the other hand, *oxyhemoglobin* (the state of oxygenated hemoglobin in healthy RBCs) and *carbonmonoxyhemoglobin* (the state of hemoglobin bound to carbon monoxide) are diamagnetic: the starting point to deeply understand this behaviour is based on their electrons configuration. Hemoglobin has many sub-unit heme groups, as the one shown in Fig.6. The iron ion could be either in the Fe^{2+} or in the Fe^{3+} state, but ferrihemoglobin or methemoglobin (Fe^{3+}) cannot bind oxygen; therefore iron must exist in the +2 oxidation state to bind oxygen (oxyhemoglobin) or carbon monoxide (carbonmonoxyhemoglobin) [19]. Recognised that iron is in ferrous state, this ion has a $3d^6$ shell which, on a first sight, following the *Aufbau*

principle, would induce to conclude a four unpaired electrons configuration, giving S=2. It is nonetheless important to keep in consideration the local environment surrounding the central iron: in fact, an electric field derived form neighbouring atoms arises, the so-called *crystal field*. The binding of a free oxygen molecule leads the system to an octahedral environment, where each iron atom is accordingly attached to the four porphyrin nitrogen atoms, the globin molecule and the oxygen molecule [19]. Given an octahedral configuration, the d orbitals fall into two classes, the t_{2g}, where orbitals point between the x, y and z axes, and e_g orbitals which point along these axes (see Fig.11) [55].

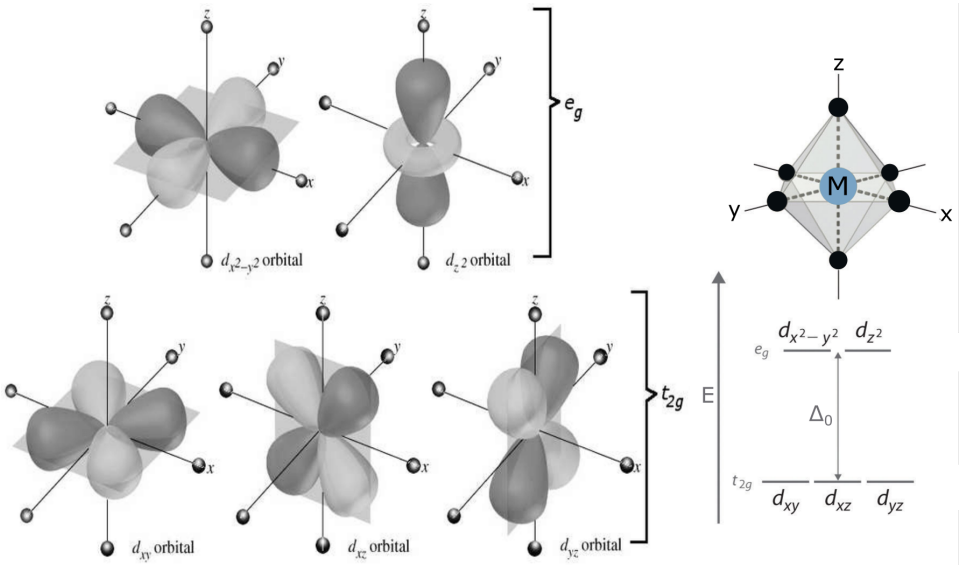

FIGURE 11. *The angular distribution of the d orbitals within the octahedral environment. The d_{z^2} and $d_{x^2-y^2}$ are grouped together and called the e_g levels; the d_{xy}, d_{xz} and d_{yz} are the t_{2g} levels. Moreover, on the bottom right is represented the energy difference Δ_0 between the two groups, while on the respective top, the corresponding atoms distribution, [58].*

In an octahedral environment, neighbouring charges (i.e. not Fe atoms) producing the crystal field are placed at $(\pm r, 0, 0), (0, \pm r, 0), (0, 0, \pm r)$: so, the t_{2g} orbitals are lowered in energy with respect to the e_g because in the former case the orbitals maximally avoid the charge density associated with atoms situated on the corners of octahedron. If one is dealing with ions in which not all 3d electrons are present, those that are present will fill the lower (t_{2g}) orbitals before filling the e_g. However, the precise order in which the orbitals fill, depends on two competing terms: the one associated with the crystal field (i.e. overlapping orbitals) and the Coulomb energy cost of putting two electrons in the same orbital (i.e. it contrasts Aufbau principle), also said *pairing energy cost*. In Fe^{2+}, where six outermost electrons are available, the crystal field energy is larger than the pairing energy (*strong-field* case), so the electrons will doubly occupy the lower energy orbitals leading to three

filled t_{2g} orbitals that result in a *low-spin* S=0 configuration, finally explaining the diamagnetic behaviour of ferrous Fe^{2+} in healthy oxygenated RBCs.

II.2.2. Magnetic susceptibility. As explained in II.2, magnetic susceptibility χ is a dimensionless constant which expresses the degree of magnetization of a material under the effect of an applied magnetic field. In this section, will be exposed the relevant values of magnetic susceptibilities related to the corpuscles of interest in blood.
Since the magnetic bodies are immersed in a buffer solution, what's really important, is not the absolute magnetic susceptibility, but the net one $\Delta\chi$, with respect to the buffer itself:

$$\Delta\chi = \chi_{particle} - \chi_{buffer} \tag{II.17}$$

In TMek, as clarified in section IV.1, blood sample is suspended in a solution of *Phosphate Buffer Saline (PBS)* only or a solution of *PBS* and *plasma*. The value of *PBS* susceptibility χ_{PBS} that will be used is $-9.05 \cdot 10^{-6}$ for a 150mM solution [59]. For the sake of completeness, the absolute values of magnetic susceptibilities of water and blood plasma are very similar, respectively, $\chi_{H_2O} = -9.04 \cdot 10^{-6}$ and $\chi_{plasma} = -8.97 \cdot 10^{-6}$ [60, 61]: this is the reason why, from now on, $-9.05 \cdot 10^{-6}$ will be the assumed value of fluid susceptibility.
Despite its well-known paramagnetic behaviour, not many experimental values of hemozin magnetic susceptibility have been reported: starting from results obtained by Hackett [62], in 2012 Coronado et al. obtained $\chi_{HC} = 320 \cdot 10^{-6}$ [63]. This value was confirmed by Giacometti et al. who measured a comparable $\chi_{HC} = 410 \cdot 10^{-6}$ [64]. In contrast to the solution susceptibilities, for hemozoin χ is positive, it is thus a paramagnetic material.
The magnetic susceptibility of RBCs depends on the oxidation state of Fe in hemoglobin which, in turns depends on what it is linked to. Healthy red blood cells presents a diamagnetic behaviour: their net magnetic susceptibility with respect to PBS, is $\Delta\chi_{h-RBC} = -0.01 \cdot 10^{-6}$, basically equal to the solution; so, in proximity to a magnet a tiny repulsive force arises [62].
On the other hand, when we deal with infected i-RBCs, things become more complicated. During the human blood stage, there's a development of hemozoin crystals within red blood particles, leading to physical changes of these corpuscles in terms of morphology, membrane shape and magnetic properties [25]. *Plasmodium*, over the intra-erythrocytic stage, causes a linear increase in hemoglobin degradation. The HCs number increases in infected RBCs, leading to an overall positive magnetic susceptibility (paramagnetic). As shown in Fig.12, there's a linear increase of both the percentage of iron as hemozoin (Fig.12A), and of the molar magnetic susceptibility (Fig.12B) as a function of the density of mature parasites (i.e. the percentage of RBC infected by the parasite in the trophozoite and schizont stage). [62].

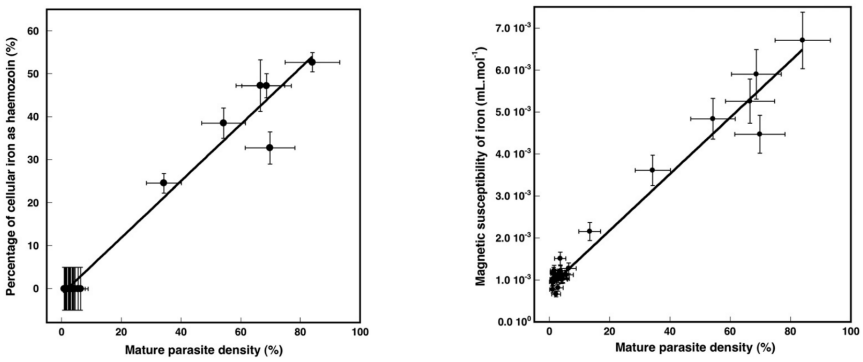

(A) (B)

FIGURE 12. *Percentage of cellular iron converted to hemozoin (A) and molar magnetic susceptibility of iron in cgs units (B), versus mature parasite density, (percentage of trophozoites and schizonts), [62].*

From these considerations, it follows that the net relative volume magnetic susceptibility $\Delta\chi_{i-RBC}$, in S.I. of units, is different at different stages: relatively to PBS it has been found $\Delta\chi_{i-RBC} = 0.82 \cdot 10^{-6}$ for the *ring stage*, $\Delta\chi_{i-RBC} = 0.91 \cdot 10^{-6}$ for the *trophozoite stage* and $\Delta\chi_{i-RBC} = 1.8 \cdot 10^{-6}$ for the *schizont stage* [62]. So i-RBCs are always attracted by a magnet, but with different strength and dynamics; as will be seen, this can be used to distinguish the stages of the infections looking at the dynamics of the magnetophoretic capture.
To conclude, there's another aspect that will be deeply analysed in section IV.1: when hemoglobin is fully oxidized, it behaves like hemozoin since it goes through a phase transition achieving an unpaired electron configuration Fe^{3+}, such that S=5/2. This oxidized form is called *methemoglobin* (*metHb*), not to be confuse with oxyhemoglobin (i.e. hemoglobin bound to oxygen for its transport to cells) and can be obtained exposing h-RBCs to oxidizing agents. *metHb*, under a magnetic field, presents paramagnetic properties with a relative susceptibility $\Delta\chi_{metHb} = 3.9 \cdot 10^{-6}$, about twice that of i-RBCs in the schizont stage. For this reason, treated RBCs (t-RBCs), obtained inducing a full conversion from hemoglobin into metHb, will be used as synthetic model of infected RBCs.
Net magnetic susceptibilities values are summarized in Table II.1.

II.3. Forces acting on a magnetic particle within a fluid

In this section, an analysis of the transport and the capture of magnetic nanoparticles in a magnetophoretic system, is presented. Particle transport in a magnetophoretic system is influenced by many forces of different nature: (i) *magnetic force* due to magnetic field gradients, (ii) *viscous drag*, (iii) *gravity*, (iv) *buoyancy*, (v) random forces due to thermal kinetics, (vi) particle-fluid interactions and (vii) inter-particle effects such as Van der Waals force. For most magnetophoretic applications involving sub-micron particles only the first four aforementioned terms are dominant and will be taken into account [66].

Particle	$\Delta\chi(\cdot 10^{-6})$
Healthy h-RBC	0.01
Ring i-RBC	0.82
Trophozoite i-RBC	0.91
Schizont i-RBC	1.82
met-Hb t-RBC	3.9
Hemozoin crystals HCs	320

TABLE II.1. *Net magnetic susceptibilities of hemozoin and RBCs with respect to PBS, [59, 60, 61, 62, 63, 64, 65].*

Gravity and buoyancy force. The first two forces are: the *gravity force* F_G, linked to the mass of the particle, and the *buoyancy force* F_B, related to Archimede's principle. Their effects are opposite, so the net contribution is:

$$\mathbf{F}_{G-B} = \frac{4}{3}\pi r_p^3(\rho_p - \rho_{fluid})\mathbf{g} \tag{II.18}$$

where ρ_p and ρ_{fluid} are, respectively, the density of the particle and the density of the fluid, and $\mathbf{g}$ is the gravity acceleration [66].

Drag force. The system the magnetophoretic force is acting on, is a multiphase and dispersed system: it means we are dealing with solid particles dispersed inside the fluid. Since we use corpuscles whose dimensions are bigger than 10 nm, both fluid and particles can be studied through Navier-Stokes equations. Assuming a small Reynolds number $Re << 1000$ (i.e. a fluid with low turbulence) and that the fluids are incompressible, it comes out, for a particle with radius r_p:

$$\mathbf{F}_{DRAG} = 6\pi\eta_{fluid} r_p(\mathbf{u} - \mathbf{v}) = b(\mathbf{u} - \mathbf{v}) \tag{II.19}$$

where η_{fluid} is the *fluid viscosity*, b is the *drag coefficient* and $\mathbf{u}$ the velocity of the fluid while $\mathbf{v}$ the particle's one. A system such that the one considered in this thesis, is in steady state condition, so the fluid does not move, which implies $\mathbf{u} = 0$. Equation II.19 becomes:

$$\mathbf{F}_{DRAG} = -6\pi\eta_{fluid} r_p \mathbf{v} \tag{II.20}$$

from which "viscous" attribute of $\mathbf{F}_{DRAG}$ is evident [66].
As anticipated at the beginning of the section, other second order forces are involved in the motion of the particle. One of them is related to the *thermal kinetics*, which gives rise to a random motion said *Brownian motion*. This random motion can be analytically expressed through a *diffusion coefficient* D that, according to *Stokes-Einstein* equation, for a spherical particle is:

$$D = \frac{k_B T}{b} \tag{II.21}$$

where $k_B = 1.38 \cdot 10^{-23} J/K$ is the Boltzmann constant and T the absolute temperature (K) [67]. From D we obtain the so-called *diffusion length* l_{diff} which represents the average distance explored considering only diffusion, and whose expression is:

$$l_{diff} = \sqrt{Dt} \tag{II.22}$$

in which t is the time of travel. The bigger l_{diff}, the bigger the contribution of the Brownian motion. Nevertheless, assuming $\eta_{fluid} = 9 \cdot 10^{-4} mPa \cdot s$ and $r_p = 3\mu m$, at room temperature $l_{diff} \simeq 100nm$ for 1 second: therefore in TMek system, the overall physics is not affected by this term. To analyse the magnetic force, a deeper focusing in the next section is useful.

II.3.1. Magnetic force. The force exerted on a magnetic particle, assuming that the length scale over which the magnetic field varies is much bigger with respect to the size of the magnetic particle itself and that the magnetic susceptibility of the particle is linear, can be expressed as:

$$F_M = \frac{\mu_0}{2} V_p \Delta\chi_p \nabla \mathbf{H}^2(\mathbf{x}_c) = \frac{2}{3}\pi\mu_0 \Delta\chi_p r_p^3 \nabla \mathbf{H}^2(\mathbf{x}_c) \tag{II.23}$$

where μ_0 is the vacuum permeability constant ($4\pi \cdot 10^{-7} H/m$), V_p the volume of the particle, r_p the radius of the particle, which in RBCs is around 3µm [68], $\Delta\chi = \chi_{particle} - \chi_{fluid}$ the net magnetic susceptibility and $\mathbf{H}(\mathbf{x}_c)$ represents the field at the position $\mathbf{x}_c$ (i.e. center of the particle), thus $\nabla\mathbf{H}^2$ is the gradient of $\mathbf{H}$ squared. Just to figure out the order of magnitude of magnetic forces involved: $F_M = 3fN$ for i-RBCs at schizont stage and $0.1fN$ for HCs.
Magnetic forces have been already employed in biochips and microfluidic systems, for example to perform magnetic cells sorting or separation [69, 70]. Two main approaches are usually considered when dealing with magnetophoretic force. In the first case, separation of biological cells is achieved by labeling them with magnetic nanoparticles and further exploiting a high-gradient magnetic field. In the second, which represent the case of TMek, the separation is obtained taking advantage of the magnetic susceptibility of the particle itself inserted in high-gradient magnetic field [45, 59]. The second approach does not involve cell labelling but exploits lower susceptibilities of cells with respect to magnetic particles, which requires intense magnetic field gradients.
To achieve such a high field gradient, it is important, firstly, to remember that the total magnetic field in space is given by two terms: the externally applied magnetic field $\mathbf{H}_0$ and the demagnetizing field $\mathbf{H}_d$. This last term (see section II.1), represents the field produced by the magnetization of the material itself and, inside the magnetic body, points in the opposite direction of $\mathbf{M}$. Since also $\mathbf{H}_d$ permeates the space out of the sample, the total magnetic field in space is given by the sum of $\mathbf{H}_0$ and $\mathbf{H}_d$ [52]. To obtain an high $\nabla\mathbf{H}$ in a portable instrument, it is convenient to use permanent magnets: these materials, residing in the category of hard ferromagnets (see section II.2), exhibit a permanent magnetization, with the spins aligned, even after removing the external field $\mathbf{H}$. Commercially available permanent magnets with high saturation magnetization and coercivity are typically made of neodymium-iron-boron (NdFeB) [71]. In TMek two strong permanent NdFeB magnets are used in combination with some micron-size Ni ferromagnetic concentrators fabricated on the chip. When the NdFeB magnets are close enough to the microchip, a macroscopic field to get a long range attractive force is given by the permanent magnets, while a microscopic deformation of the field lines, in order to localize interested particles on the sensitive areas, is provided by the Ni concentrators. Lifting the NdFeB magnets by 5mm from the chip is enough to strongly suppress the magnetic force, thus achieving a way to modulate it over time.

II.3.2. Motion equation in TMek. Identified the four main terms, is time to sum them up in a unique motion equation. Before doing that, some premises are needed.
TMek setup can work in two configurations: a first *horizontal* configuration, in which the surface of the chip is placed parallel to the table top, and a *vertical* configuration, where the surface of the chip is placed perpendicular to the table top. It is evident that, depending on which configuration we are dealing with, forces are competing in a different way, and this is displayed in Fig.13 below.

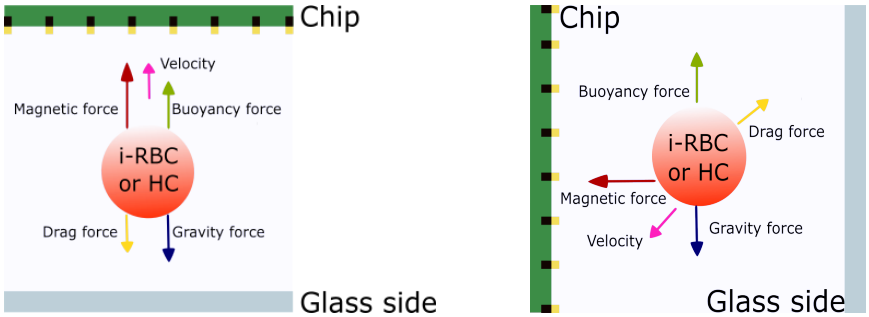

(A) (B)

FIGURE 13. *Forces in TMek magnetophoretic system. (A) represents the horizontal configuration, while (B) the vertical one.*

In Fig.13A the direction of the forces is just along one axis perpendicular to the surface of the chip and the calculus of forces is straightforward and a typical vertical motion in a viscous medium is expected. On the other hand, looking at the vertical configuration (see Fig.13B), the balance of non-collinear forces gives rise to a more complex motion. Here particles would sediment because of the gravity, but if they display paramagnetic properties, a magnetic force, attracting them towards the chip, arises in perpendicular direction with respect to the gravity, bending the trajectory. It follows that the movement of the corpuscle is not parallel to the chip's surface, neither perpendicular to it; by consequence, the drag force is obliquely oriented. A simple analytical analysis can be carried out for the former horizontal situation, while the latter case, to be fully understood, needs a numerical software approach such as *COMSOL*, a finite element multiphysics analysis solver [72].
So, looking at Fig.13A and summing all the aforementioned force terms (i.e. magnetic, gravity, buoyancy and drag), the resulting motion equation using Newton's second law is:

$$\frac{\mu_0}{2} V_p \Delta\chi_p \nabla \mathbf{H}^2(\mathbf{x}_c) - V_p(\rho_p - \rho_{fluid})\mathbf{g} - b\mathbf{v} = \rho_p V_p \frac{d\mathbf{v}}{dt} \tag{II.24}$$

Grouping some terms, equation II.24 can be recognized as the one of an accelerated motion inside a viscous medium; characteristic timing that the system needs to reach a steady-state is $\tau = (\rho_p V_p)/b$.

Property	HCs	i-RBC	h-RBC
Net susceptibility ($\Delta\chi$)	$320.72 \cdot 10^{-6}$	$1.8 \cdot 10^{-6}$	$0.01 \cdot 10^{-6}$
Radius (r)	0.18(µm)	2.78(µm)	2.78(µm)
Density (ρ_p)	$1490(kg/m^3)$	$1125(kg/m^3)$	$1125(kg/m^3)$

TABLE II.2. *Summary of physical and morphological properties of HCs, i-RBCs and h-RBCs. In the first line $\Delta\chi$ is the one of the particle, with respect to the fluid, [27, 68].*

Within a region where $\nabla\mathbf{H}^2$ can be considered constant, referring to the physical and morphological properties resumed in Table II.2, τ can be assumed less than $0.5\mu s$, meaning that a little interval is sufficient to reach a steady-state. The particles have a constant velocity $\overline{\mathbf{v}}$ driven by the balance between the magnetic and gravity-buoyancy force. This value can be obtained starting from equation II.24, zeroing the right term, since no variations during time are present, and rearranging the remaining ones:

$$\begin{aligned}\overline{\mathbf{v}} &= \frac{\frac{\mu_0}{2} V_p \Delta\chi_p \nabla\mathbf{H}^2(\mathbf{x}_c) - V_p(\rho_p - \rho_{fluid})\mathbf{g}}{6\pi\eta_{fluid} r_p} = \\ &= \frac{2r_p^2}{9\eta_{fluid}}\left[\frac{\mu_0}{2}\Delta\chi_p \nabla\mathbf{H}^2(\mathbf{x}_c) - (\rho_p - \rho_{fluid})\mathbf{g}\right]\end{aligned} \tag{II.25}$$

In order to move towards the chip, $\overline{\mathbf{v}}$ must be parallel to the $\nabla\mathbf{H}^2$, which points towards the chip as the field increases when moving towards the magnets placed behind it. Thus the following condition must hold:

$$|\nabla\mathbf{H}^2(\mathbf{x}_c)| > \left|\frac{2(\rho_p - \rho_{fluid})\mathbf{g}}{\mu_0 \Delta\chi_p}\right| \tag{II.26}$$

The fundamental physical quantities which determine the minimum gradient of magnetic field needed to capture a corpuscle are the net susceptibility of the particle with respect to the fluid it is immersed in (i.e. $\Delta\chi_p$), and the difference of their densities ρ. As it will be explained in section IV.1, in TMek sample preparation, blood is diluted with PBS, in order to achieve the right value of *hematocrit Hct* (hematocrit is the volume percentage of red blood cells in blood). Being the mass densities of plasma and PBS, respectively, $1.025g/mL$ and $1g/mL$ ("SIGMA-ALDRICH" PBS (1X)), we can use the same density for both fluids $\rho_{fluid} = 1g/mL$ [73]. Concerning net susceptibility $\Delta\chi_p$, the values of $\Delta\chi_p$ reported in Table II.1 apply to RBCs and HC dispersed in diluted blood as well as in plasma+PBS solutions. Knowing all these values, is possible to deduce the minimum gradient of $\mathbf{H}^2$, needed to attract magnetic particles towards the chip: all these values are reported in Table II.3.

Particle	Minimum $\nabla \mathbf{H}^2$ value (A^2/m^3)
Healthy h-RBC	$1.56 \cdot 10^{17}$
Ring i-RBC	$1.9 \cdot 10^{15}$
Trophozoite i-RBC	$1.72 \cdot 10^{15}$
Schizont i-RBC	$8.6 \cdot 10^{14}$
met-Hb t-RBC	$4 \cdot 10^{14}$
Hemozoin crystals HCs	$2.26 \cdot 10^{13}$

TABLE II.3. *Minimum gradient of magnetic field values needed to attract particles towards the chip: keeping into account Table II.1 values, the bigger the net magnetic susceptibility, the smallest the gradient.*

This leads to typical values of $\nabla \mathbf{H}^2$ on the order of $1 \cdot 10^{15} A^2/m^3$ for i-RBCs and $1 \cdot 10^{13} A^2/m^3$ for HC. From Table II.3, it is evident that h-RBCs, since their $\Delta\chi_p$ is quasi-zero, need an extremely high field gradient, so that a value of about $1 \cdot 10^{15} A^2/m^3$ can be safely used to separate infected RBCs and HC from healthy ones. By the way, HCs and metHb are more paramagnetic, and easily attractable, with respect to any i-RBC stage.

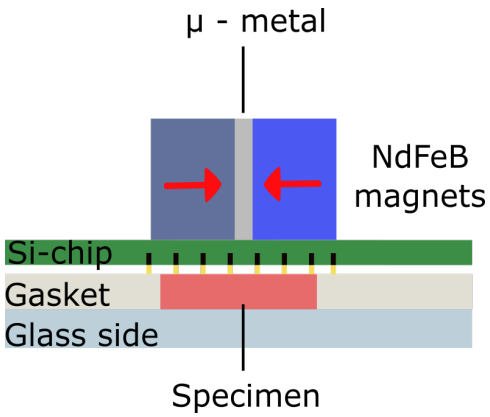

FIGURE 14. *In this figure are represented the fundamental magnetic elements to analyse the specimen, usually a drop of blood mixed with other liquids such as plasma or PBS. On a PMMA glass is deposited a PDMS gasket, in which the sample is contained during the measurement. Above the blood is nestled the silicon chip with nickel pillars aimed to catch the paramagnetic particles, also thanks to the magnetic force due to the quasi-uniform magnetic field gradient of the NdFeB permanent magnets.*

II.3.3. TMek two-levels approach. Several considerations have now been exposed about the magnetic features that a magnetophoretic system must display. TMek, in order to achieve magnetic separation and sense the targeted particles, exploits a two-levels approach. A macroscopic strong and approximately uniform (within the cell height) $\nabla \mathbf{H}^2$ is provided by a magnet assembly made of two permanent magnets, able to attract particles on long-range. A more localized distortion of the field lines is provided by Ni micrometric concentrators fabricated inside the silicon chip, thus creating a localized field gradient which concentrate particles on the electrodes. As explained in next section, the electronic signal measures a relative impedance variation $\Delta R/R$, and this, is proportional to the so-called *volumetric fraction* Φ, which is given by the particle volume V_p divided by the sensitive volume of the electrodes V_{el}. It follows that, the smaller V_{el}, the highest the sensitivity of the system. A micro-array of Ni pillars is then used to concentrate targeted particles onto small electrodes, fabricated on top of them.
In Fig.14 is represented the fundamental magnetic elements to analyse the specimen in horizontal configuration. During the measure, the sensitive side of the chip is put in contact with the sample, while on the rear is placed the assembly of the magnets. These two are *N52 grade* by "Supermagnete" [74], made of neodymium iron boron NdFeB. They have parallelepiped shape (25x25x6mm), with two north poles facing each other, pointing along the broader surface and in both cases towards an interposed 0.2mm µ-metal sheet (see Fig.14). Due to their huge magnetization and repulsive strength, they have to be clamped together mechanically. Between the magnets, µ-metal is interposed: it is a nickel–iron soft ferromagnetic alloy, which modify the lines of the field in the central zone of the chip, and concentrate them such that they exit perpendicular to chip's surface, without inhomogeneity with respect to others coordinates (see Fig.14). It has been previously demonstrated that the $\nabla \mathbf{H}^2$ at 0.5mm from the magnet surface, i.e. at the typical distance of the concentrators from the magnet when the latter is placed in close proximity to the back of the chip, is $7 \cdot 10^{14} A^2/m^3$, the same order of magnitude of the threshold values listed above (see Table II.3) for the horizontal configuration [51]. The experimental value is close to threshold, therefore, due to the biological variability of the parameters used to estimate the values of II.3, the horizontal configuration is less used when dealing with i-RBCs. On the other hand, a vertical configuration would be more favourable to magnetic force, rather than sedimentation of targeted particles, and this is the reason why is usually preferred during trials.
Regarding the Ni micro-array concentrators, their configuration was subject of another previous thesis work which evidenced the optimal geometrical layout [50]. It is an hexagonal array, chosen to maximize packing and improving capture efficiency, of cylindrical Ni concentrators with height of $20\mu m$, embodied in the Si-chip. Their diameter is $40\mu m$ and the spacing is $80\mu m$. In order characterize the magnetic properties of the system, an hysteresis cycle of the Ni array has been measured using a *Vibrating Sample Magnetometer (VSM)*: the resulting M-H curve along the out-of-plane direction is represented in Fig.15 and highlights a required external field of about $400000 A/m$ in order to saturate Ni pillars (see section III.1). The aforementioned NdFeB permanent magnets can provide it, since the experimental value of $\mathbf{H}$ at $500\mu m$, the typical distance between the magnet assembly and the top surface of the chip when it is placed in close proximity to the magnets, is about

7700 Oe (i.e. 612746A/m) [74, 51].

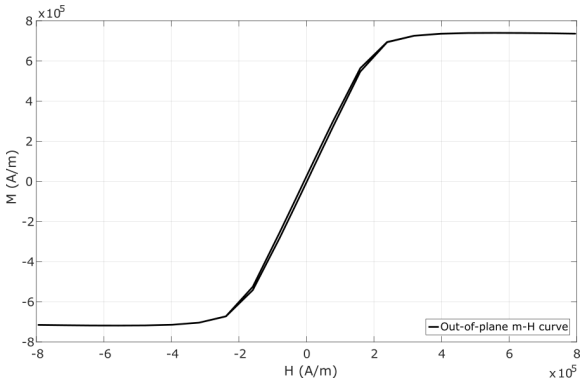

FIGURE 15. *Out-of-plane magnetization curve M-H of a single sensitive area of the chip. It is possible to see how the external magnetization field exerted by NdFeB permanent magnets is sufficient to saturate the magnetic structures at all.*

In Fig.16 the results of a multiphysics simulation using *COMSOL* [72], carried out in previous thesis work, are reported [51]. Assuming an external uniform magnetic field H_0 able to saturate Ni pillars and perpendicular to the surface of the chip, it follows that a demagnetizing field H_d from the pillars themselves arises such that the total magnetic field is given by the sum of the two: $H_{tot} = H_0 + H_d$. The resulting magnetic field will have areas with different density of field lines, which implies a different magnetic force and capability of attraction. As it is possible to see by Fig.16, the gradient of the field is strengthened in correspondence of the Ni pillars such that is possible to capture the magnetic corpuscles in correspondence of sensitive areas where impedimetric measurements are done.

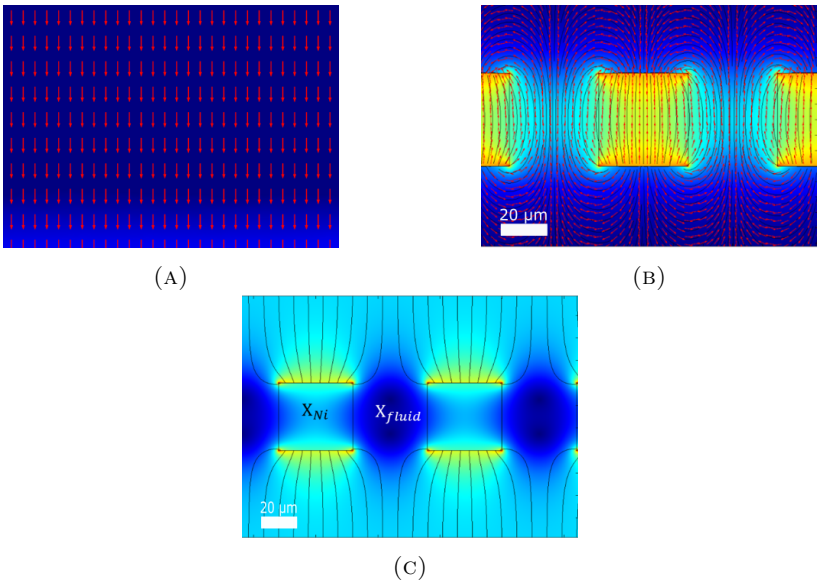

(A) (B)

(C)

FIGURE 16. *(A) depicts the approximately uniform applied magnetic field H_0. Figure (B), on its turn, represents the demagnetizing magnetic field H_d generated by the magnetization of the Ni pillars. The sum, expressing the interaction of the previous fields, is then simulated in the third (C) picture: $H_{tot} = H_d + H_0$. Simulations were carried out by COMSOL and have just qualitative purpose. Modified from [50].*

II.4. Principles of impedance detection

As previously said, the detection system which permits measurements of the signal related to the magnetically captured particles, is based on *impedance detection*. To fit the requirements of a diagnostic tool for malaria in terms of costs, robustness, rapidity and usage in difficult environmental conditions [2, 11], *impedance detection* has been chosen. This approach, along with the just mentioned pros, is *label free*, (i.e. no markers are needed to help detection) and permits *real-time* measurements [75]. In TMek, the targeted particles (hemozoin crystals and infected red blood cells) are attracted above interdigitated electrodes, inducing an effective variation in the impedance of the detection system.
Impedance spectroscopy (IS) is a generic term indicating the small-signal measurement of the electrical response of a material of interest (including electrode effects) and the subsequent analysis of the response to yield useful information about the physio-chemical properties of the system [75]. The range of applications of this technique is quite wide [51, 75, 76]. Among them, *electrochemical impedance spectroscopy (EIS)* is highly relevant [75]. EIS involves measurements and analysis of materials in which ionic conduction strongly predominates; in a biological measurement, it requires the application of a bias voltage from outside, high enough to induce electrochemical reactions, followed by the detection of the variation of the complex impedance, connected to the change in a physiological quantity of

interest [75]. In TMek, the voltage bias is kept small enough (100mV) to avoid electrochemical reactions at the surface of targeted particles (HC and RBCs) and just measure the change of impedance between electrodes due to to the presence of those insulating particles, with respect to the ionic conductive medium where electrodes are immersed.

II.4.1. Impedance spectrum. The crucial starting point to characterize the behaviour of the device and its response versus frequency, is to study the charge transport between electrodes immersed in an electrolyte. Blood diluted with PBS, indeed, is a ionic solution, i.e. an electrolyte, with salt ions randomly distributed between water molecules, such that, if external forces are absent, will tend to minimize Coulomb repulsion. When electric fields are applied, free ions movement takes place, such that a net current can be measured between the electrodes. By the way, it remains the fact that ions mobility is much different with respect to the one of electrons in metals: the average value of ion's mobility in PBS has been reported around $10^{-3} cm^2/(V \cdot s)$ [51], which is six orders of magnitude less with respect to free electrons in crystalline silicon [77]. On top of this, the ionic carriers can be chemically active and can react with electrode surfaces; it is therefore important to include chemical phenomena in the treatment of ionic conduction. Because of this difference in terms of conducting behaviour, two physical phenomena arise: *bulk transport* and *interface transport* [78].

Bulk transport: in the bulk, only ionic components are responsible for the transfer of charge. The bulk transfer of charge is similar to that in resistors. Therefore, to fully characterize bulk transport, is necessary to extrapolate an accurate expression for its resistivity. To execute this characterization molar conductivity of electrolyte is required, even though evaluating it is not an easy task. Looking at the data sheet of PBS furnished by "SIGMA ALDRICH" [73], PBS conductivity ranges from 14700 to $16300 \mu S/cm$ such that the overall bulk solution resistivity ρ_{bulk} is about $67\Omega \cdot cm$.

Interface transport: in almost all electrochemical experiments, at least one electrode–electrolyte interface is present. The charge transport phenomena taking place here are quite different from the bulk-type previously described. Two main types of metals behaviour exist: *partially polarizable electrodes*, in which redox reactions with exchange of electrons between electrode and electrolyte take place, and *inert metal electrodes* (e.g. gold), where no redox reaction is present.
Independently by the aforementioned category, an important common phenomena appears at the interface between metal electrode and electrolyte: an *electrical double layer (EDL)*. This structure consists in two parallel layers of charge which are positioned at the surface of the electrode, when it is brought in contact with an electrolyte. Starting from the model proposed by Helmholtz, who for the first time realized that charged electrodes repel ions of the same sign, attracting counter ones, in 1963 was proposed the so-called *BDM model*, by the name of the three physicists that elaborated it [79]. This model states, as represented in Fig.17, that given an electrically charged electrode, a first layer of solvent molecules (i.e. not ions) highly orientated to the electric field is formed at the *inner Helmholtz plane (IHP)*, followed by solvated ions, whose charge is opposite with respect to the electrode; through the centers of these ions passes the *outer Helmholtz plane (OHP)*. Finally, beyond the

OHP, there is the *diffuse layer* proposed by Gouy-Chapman [80]. So, this system represents an electrical double layer which has, between these two opposite surface charges, a dielectric layer (i.e. OHP thick), leading to a *double-layer capacitance*. Moreover, the charge distribution is such that the apparatus is electrically neutral [79].

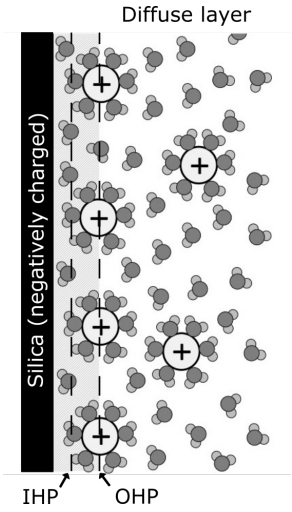

FIGURE 17. *Schematic of double layer in a liquid at contact with a negatively-charged solid, according to the BDM model. Given a negatively charged silicon wafer, put in contact with an electrolyte solution, three main regions arise, identified by three different labels: the inner Helmholtz plane (IHP), containing only solvent uncharged molecules, the outer Helmholtz plane (OHO), defining the region in which are present solvated ions of positive charge, and, way further, the diffuse layer in which dispersion of positive ions increases the more the distance from the wafer accumulates. Modified from [81].*

The resulting capacitance C_{dl} is given by the equation $C_{dl} = \frac{d\sigma}{d\Phi}$ in which σ is the surface charge and Φ, the electric potential. Φ has an exponential form, with respect to gap r (i.e. distance of wafer plane from the particle center), justified by the presence of *diffuse layer* for increasing distances:

$$\Phi(r) = \frac{\kappa \Phi^d a}{r} \exp^{-\kappa(r-a)} \tag{II.27}$$

where Φ^d is the so-called *Stern potential*, a the molecule radius and κ the *Debye length* (i.e. a measure of how far the electrostatic effect of the potential persists) [79].
For coplanar interdigitated electrodes the overall capacitance can be simply expressed as:

$$C_{dl} = A_{el} \cdot C^0_{el} \tag{II.28}$$

with A_{el} the area of the single electrode and C^0_{el} representing the characteristic double layer capacitance per unit area, with typical values ranging from 10 to $40 \mu F/cm^2$ [82].

The impedance spectrum of coplanar electrodes immersed in an electrolyte (Fig.18) displays two asymptotic behaviours: *double layer capacitance* C_{dl} is dominant at low frequencies, whereas another capacitive term, due to the capacitive coupling between electrodes immersed in the solution, C_{sol}, is present and prevalent, at higher frequencies. Between these two capacitance attitudes of the system, there is a resistive plateaux determined by the real part of the solution impedance R_{sol}, strongly related to the electrodes morphology and the conductivity σ_{sol} of the sample.

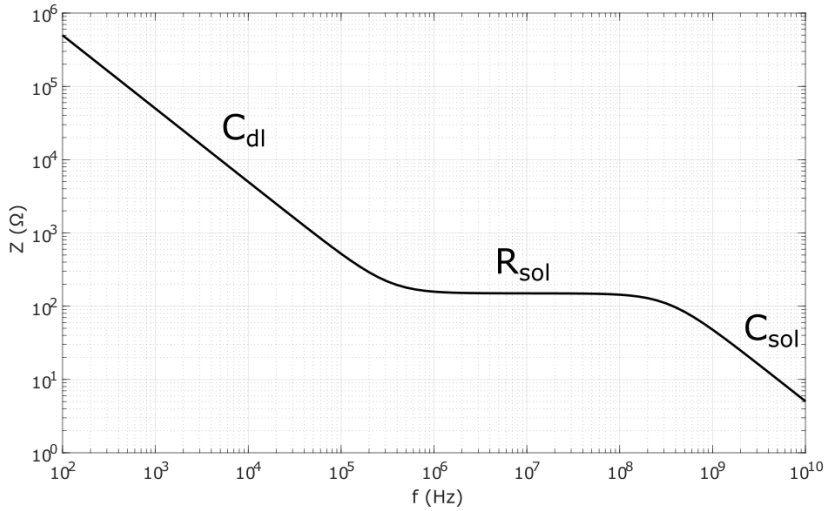

FIGURE 18. *Bode plot of the impedance spectrum of bipole represented in Fig.19, [83].*

To evaluate the spectrum of the impedance and understand how the Bode plot, represented in Fig.18, has been obtained, the electrical model of the system is here displayed:

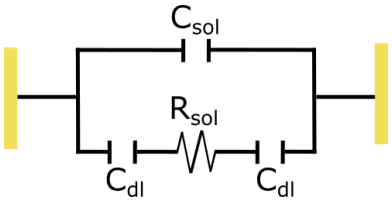

FIGURE 19. *Electrical model of a bipole formed by two electrodes immersed in a electrolytic solution: C_{dl} represent the double layer capacitance, R_{sol} the resistance of the electrolytic solution and C_{sol} the capacitance of the same solution, [83].*

Looking at Fig.19, there are two ideal double layer capacitances C_{dl}, representing the electrodes-electrolyte interfaces, in series with resistance R_{sol}; these three

elements are in parallel with C_{sol}. The total impedance Z is then [83]:

$$Z = \frac{Z_1}{1 + j\omega C_{sol} Z_1} \tag{II.29}$$

with Z_1 given by:

$$Z_1 = R_{sol} + \frac{2}{j\omega C_{dl}} \tag{II.30}$$

This transfer function presents one zero f_L and one pole f_H at higher frequencies:

$$f_L \simeq \frac{1}{\pi R_{sol} C_{dl}} \tag{II.31}$$

$$f_H \simeq \frac{1}{2\pi R_{sol} C_{sol}} = \frac{\sigma_{sol}}{2\pi \varepsilon_0 \varepsilon_{r,sol}} \tag{II.32}$$

where $\varepsilon_{r,sol}$ is the permittivity of the solution that, for PBS, is around 80 [73]. Between f_L and f_H there's a flat region where C_{dl} are shorted and C_{sol} is acting as an open circuit, such that the overall behaviour is given by R_{sol}. It is in this last region that TMek operates, so it would be useful to evaluate the corner frequencies values. These are given by the simulations run with *COMSOL Multiphysics* (see Fig.18) [50, 51]. R_{sol} depends on the conductivity of the medium and the geometrical disposition of the electrodes. In case of interdigitated rectangular electrodes, for example, as stated by M.Ibrahim et al. [76, 83], the resistance R_{sol} can be approximated as:

$$R_{sol} \simeq \frac{2}{\sigma_{sol} \cdot (N-1) \cdot L} \sqrt[3]{\frac{S}{N}} \tag{II.33}$$

in which N is the number of interdigitated electrodes with length L, width W and spacing between electrodes S. For annular electrodes such as TMek case, it does not exist an analytical expression of R_{sol}, therefore equation II.33 has just been used as a starting approximating value, later fine-tuned with numerical simulations with *COMSOL*.
As later justified by the design of the electrodes, and assuming $C_{dl}^0 = 20\mu F/cm^2$ and $R_{sol} = 150\Omega$, the first zero of the spectrum is at $f_L = 234KHz$. On the other hand, performing a sweep from 50Hz to 50MHz, f_H has been measured around GHz, and this is endorsed by further simulations [51]. It follows that the resistive plateaux is around 1MHz, and this is the region where TMek operates (i.e. from 1MHz to 3MHz) to be more sensitive to the resistive impedance of the sample, which, in turns, depends on the presence of captured particles between electrodes.

II.4.2. Quantitative evaluation. Now it is time to focus on how the system can provide a quantitative estimate of the magnetically captured particles above the Ni concentrators.
The detection takes place once HCs and i-RBCs are on the sensitive area, since their conductivity is different from the electrolyte's one, such that a variation of the resistance R_{sol} is detected. What is connected to the number of captured particles, is the relative variation of the impedance, so $\Delta R/R_0$.
The starting point relies in the analysis of the electrical features of red blood cells and hemozoin. An approximately spherical RBC is composed by an external non conducting membrane and, inside, cytoplasm: these two, can be respectively modelled as a capacitance $C_m \simeq 1\mu F/cm^2$ and a resistance R_{cyt}, as depicted in Fig.20A. The overall cell would be then the series of two capacitors and one resistance. This system, at low frequencies, behaves as an insulator, since its impedance tends to

infinity for decreasing frequency; the corner frequency on the other hand is on the order of GHz [84]. It follows that, at TMek's measurements frequencies in the range of MHz, the RBC cell behaves like an insulator. The same insulating quality has been found for hemozoin [64].

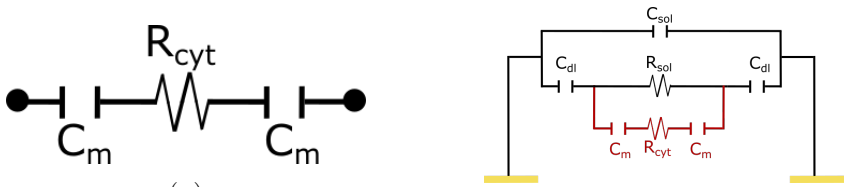

(A) (B)

FIGURE 20. *(A) depicts the electrical equivalent of a red blood cell, where only the capacitance of the membrane C_m and the resistance associated to the cytoplasm R_{cyt} are considered. On the other hand, (B) represents the interaction of the electrical equivalent of RBC (red) with the electrical equivalent of the bipole formed by two electrodes and immersed in an electrolytic solution (black), like the one represented in Fig.19, [84].*

Established the insulating behaviour of the interesting particles involved in malaria diagnosis, it is possible to estimate the increase in resistivity thanks to the Maxwell's mixture equation, which gives an average of the conductance of composite materials [85, 86]:

$$\sigma_{mix} = \sigma_m \left(1 + 3\frac{V_p}{V_{el}} \frac{\sigma_p - \sigma_m}{\sigma_p + 2\sigma_m}\right) \tag{II.34}$$

where σ_{mix} is the total conductivity of the composite material (i.e. the total mixture of particles and elements), σ_p the conductivity of the particle (i-RBC and HC), σ_m the conductivity of the medium, V_p the volume of the particle and V_{el} the sensitive volume of the electrodes. As described above, since attracted particles can be assumed insulators, $\sigma_p = 0$, so the equation II.34 can be simplified:

$$\sigma_{mix} \simeq \sigma_m \left(1 - \frac{3}{2}\Phi\right) \tag{II.35}$$

with $\Phi = V_p/V_{el}$ is the volumetric fraction. This formula, for small values of Φ, can be elaborated, passing from conductivity to resistivity ρ_{mix}, and leading to the subsequent expression:

$$\rho_{mix} = \rho_m \left(1 + \frac{3}{2}\Phi\right). \tag{II.36}$$

ρ_{mix} and ρ_m are directly related, through a common constant, to macroscopic values R_{mix} and R_0, which are, respectively, the value of the whole mixture resistance and the resistance when no particle is present. It follows that the meaningful percentage variation is:

$$\frac{\Delta R}{R_0} = \frac{R_{mix} - R_0}{R_0} = \frac{3}{2}\Phi = \frac{3}{2}\frac{N_p V_{sp}}{V_{el}} \tag{II.37}$$

where N_p is the number of particles and V_{sp} the volume of one of them.
The final relevant signal exploited by TMek is proportional to the one given by

equation II.37, i.e. the total percentage variation of the resistance, which, in turns, is proportional to the volumetric fraction of attracted cells: the more the captured particles, the bigger the signal. Noteworthy, the ratio between sensitive volume of the electrodes and the one of corpuscles is important, such that several considerations will be necessary during the design of the chip. First of all, it appears clear the necessity to concentrate as many particles as possible in a small area to increase the volumetric fraction and the signal. This useful signal, can be better distinguished from the noise and other disturbs, through a *differential measurement*. The signal from reference electrodes, identical to those above the concentrators but without Ni pillar underneath, is subtracted from the measure electrodes, where targeted particles are supposed to be captured. In this way the common mode signal due to spurious fluctuations can be partially eliminated.

CHAPTER III

Experimental techniques and methods

This chapter deals with several interdisciplinary topics. First, I present the design of a new chip which has been realized during my thesis. A description of micro-fabrication processes exploited and optimized in order to produce the new version of the chip is then reported. A short description of the electronics employed for the impedance spectroscopy detection is also included. Finally, the whole setup is presented, together with MATLAB software used to control the test and perform data analysis.

III.1. The new chip design

The layout of the new chip presented in this section, takes its origins from previous Master's thesis works carried out by L. Callegari [50] and E. Giuliani [51]. The intent of this new layout is to improve previous designs in terms of sensitivity and reliability. In particular, the main goal, was to reduce as much as possible a *drift disturbance* affecting all TMek measurements. In fact, during each experiment, fluctuations of the baseline signal, unrelated to the actual signal due to captured particles, can impede a reliable and automatic data analysis.
Before starting to focus on the proper layout, first, let's review how the differential measurement of the signal is carried out.
As already outlined, the impedimetric measurement of TMek is actually a *differential impedimetric measurement*, since it exploits two different impedimetric measures in order to get a final signal free of spurious disturb. A signal, said "measurement signal", comes out from the electrodes placed above Ni pillars, where there is a variation in resistance due to the captured particles, while a second signal, called "reference signal" comes from identical electrodes without Ni pillars underneath and it is just related to fluctuations such as temperature variation, medium evaporation and liquid motion inside the cell once the chip is backed on it. To simultaneously get these two signals, which will be then subtracted one to the other (i.e. "measurement" minus "reference"), at least three distinct electrical contacts and two different detection regions are needed (for further explanations still refer to section III.6). As seen in section II.4, in fact, to perform a single impedimetric measure at least two interdigitated electrodes are needed, between which an AC voltage is applied and the flowing current is measured to determine the impedance and its changes over time. In TMek, a first set of *measurement* electrode "M" is placed in one region and made by inner and outer annular electrodes, all connected in parallel to the measure pad and to the *common* pad "C". A second set of *reference* electrode "R", identical in number and shape but without Ni pillars underneath, is fabricated nearby, with all outer electrodes connected to the reference pad and inner ones again to the same *common* pad "C". The old configuration of the chip

is represented in Fig.21 where the two areas are well separated, the measurement area (green) on the left and the reference area (grey) on the right.

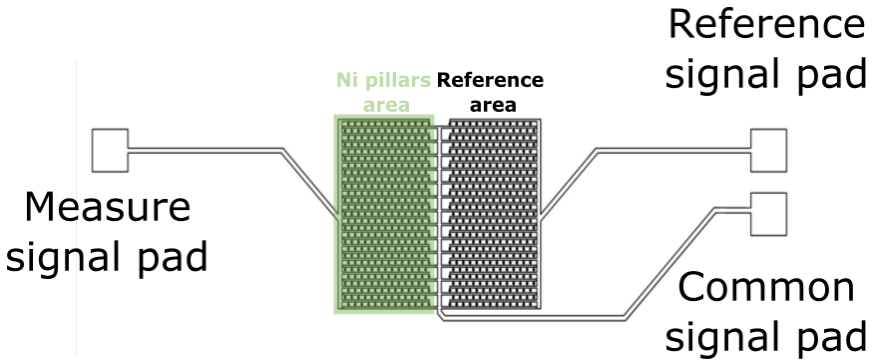

FIGURE 21. *CAD drawing of the old chip layout [87]. Within the green area, 350 Ni pillars and related electrodes are fabricated, while in the grey area only electrodes with the same shape, number and layout are realized. "M" and reference "R" signal pads are sharing the same common "C" signal pad, used to extract the net outcome, [51].*

To the "M" electrode and the "R" electrode, two out-of-phase sinusoidal voltage signals are applied, while the common pad is connected to the virtual ground of a transimpedance amplifier. In this way the current flowing in the feedback resistor is proportional to the difference between the impedance seen between the measurement and reference electrodes.
As it is possible to see from Fig.21, within each of the two regions (2x4mm wide), several interdigitated electrodes are fabricated: in the old layout we had 350 annular interdigitated electrodes per area. Moreover, it is important to underline that the areas on the chip and the mounting in the reader are designed in such a way that the plane separating the two external permanent magnets projects on the vertical symmetry axis of the measurement area: this allows to maximize capture efficiency [50]. Since the physical separation between measurement and reference areas was assumed to be one of the origins of the *drift disturb*, the first innovation implemented in the new layout of the chip is the *interpenetration* of the measurement and reference areas: the electrodes which were in the right reference zone have been moved to the *old measurement area* (i.e. the green one of Fig.21). Introducing this upgrade permits the reference area to see the same disturbances and fluctuations present also in the measurement region, such that a subtraction of these two signals should help, in an ideal case, to remove all common disturbances. The new layout is shown in Fig.22.

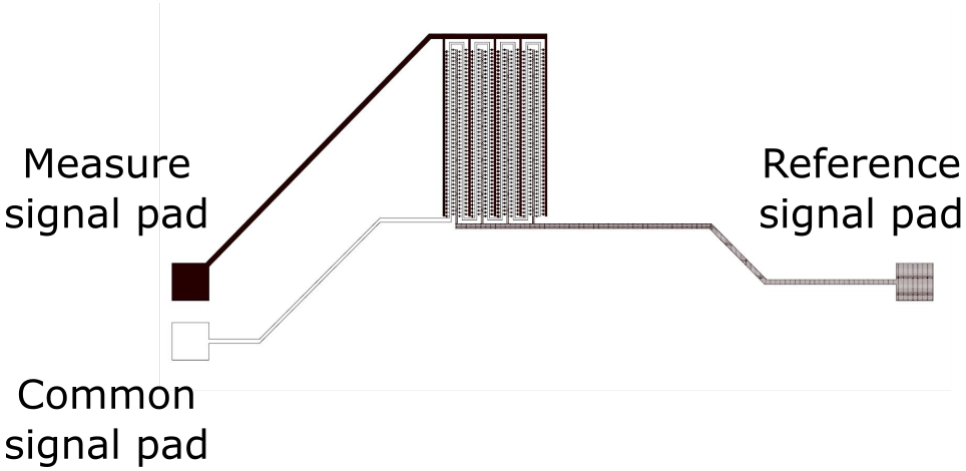

(A)

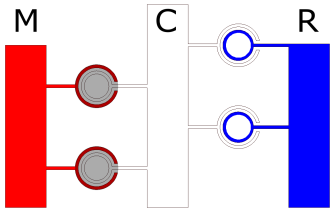

(B)

FIGURE 22. *(A) New layout used for the fabrication of the electrodes and the Ni pillars. With respect to image of Fig.21, here reference and measurement regions are interpenetrated, so there isn't a marked separation. Again, for a single sensing area, three signal pads are needed. (B) A zoom of the interpenetrated electrodes, whose shape is later explained: in white the common electrode "C", in blue the reference electrode "R" and in red, above the grey Ni pillars, the measurement electrode "M".*

It's now time to illustrate the shape of the interdigitated electrodes which are present in the interpenetrated areas mentioned above. Typical shapes of the metallic contacts used in impedimetric measurements are rectangular or have, at least, a resembling sharp geometry [83]. By the way, since from previous feasibility studies and simulations was evident that the optimized shape for the Ni concentrators was the cylindrical one, this was the direction taken. In order to maximize the capture efficiency and the volumetric fraction, to improve the signal, the adapted solution was an hexagonal array of circular concentrators. From numerical simulations and experimental validation, the Ni array is optimized for circular Ni pillars with height of $20\mu m$ and diameter of $40\mu m$ [50, 51].
Another step made to improve the layout of the chip, consists in removing electrodes from useless regions of the sensitive area over the nickel pillars: in fact, during magnetophoretic experiments, the captured particles accumulate on the outer edges of

the Ni pillars with respect to the axial symmetry plane of the external magnetic field, and not randomly above all the cylinders (see Fig.23).

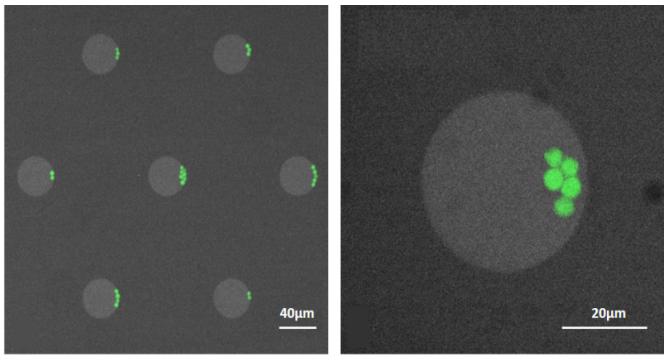

FIGURE 23. *Images of stained t-RBCs attracted by nickel concentrators. It is noted that, during magnetophoretic attraction above the Ni pillars, due to the configuration of the field lines, a major attraction is present at the edges of the magnetic structures, suggesting, firstly, a circular shape for the concentrators and, in second place, a maximization of electrodes sensitive area, obtained by the removal of inner regions, [51].*

To achieve a better sensitivity, not only the original one with inner and outer concentric annular electrodes at the edges of the pillar (see Fig.24A below) has been considered; also a new layout has been implemented with more complex geometries that leads the reduction of sensitive area of the electrode. Based on the symmetry of the external field produced by the external NdFeB magnet assembly, apart from the central region of the active area, the lateral regions have electrodes only in the external half circle with respect to the symmetry plane. Only in the central region, a more interdigitated electrode covering the whole circular footprint of the Ni pillars, is present (Fig.24B), whereas in the left region, the electrodes occupy only the left-part of the pillar and everything is mirrored, with respect to the symmetry plane (Fig.24C), on the right. The old configuration and the new one, for central and right electrodes on pillars, are represented in the Fig.24.

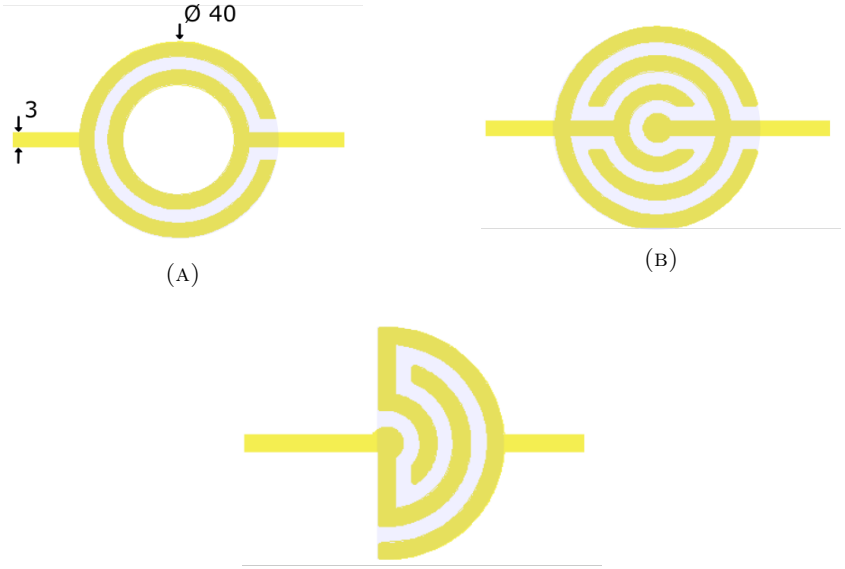

(A) (B)

(C)

FIGURE 24. *CAD drawings of the three designs of electrodes used in TMek. In shaded blue is reported the sensitive area of the specific layout. All the tracks are* $3\mu m$ *wide and spaced by* $3\mu m$*; the diameter of the circle containing them is* $40\mu m$*. (A) depicts the annular shape electrode with a sensitive area placed on the edge, (B) and (C) represent the drawings of the electrodes used in the new chip designed, where sensitive region has been optimized in order to catch as many corpuscles as possible on the smallest useful area.*

To summarize, during my thesis work I realized two new chips, both with interpenetrated electrodes, but with different electrode layouts: *C1* with annular electrodes like in the first TMek version and *C2* with a more complex filling of the active portion of Ni concentrators (Fig.24B,C).
The width and height of tracks used for the electrodes are $3\mu m$ and 200nm, respectively. Each is led to a wider track of $40\mu m$ inside the active region and that, is enlarged to $100\mu m$ in the peripheral zone. These wide tracks are then connected to the pads that, through spring contacts, implement the electrical connection to the electronic board in the cartridge and finally to the electronics performing the impedimetric measurement (see section III.7). Each of these squared pads has a side of $800\mu m$. An active area measures 3520x2100μm and inside there are 360 Ni pillars distributed along 8 columns of 45 pillars each; these 8 columns are, in their turn, divided in 4 pairs. Each of these pairs, which represents an area of measure, since it has been chosen an interpenetrated geometry, is separated by the others pairs of concentrators columns by an equivalent void width where only reference electrodes are fabricated. The distance between concentrators along the same column is of $80\mu m$, while it is of $140\mu m$ in the lateral direction (i.e. within each pair the two columns are staggered to maintain the hexagonal layout of the old chip,

see Fig.35 for the final result). The previous distance values have been obtained trying to keep the overall resistance matching that of the old chip, so as to use the same electronics. Even though in the previous design there were less concentrators, 350, in the new one their number is 360: that's because the new electrodes have a smaller total resistance. The resistances evaluations of the three different designs have been carried out with FEM simulations using *COMSOL*. For 360 pillars there are, as a consequence, 360 interdigitated pairs of measure electrodes and as many reference ones.
All these considerations were just for one sensitive area, but in TMek chip, whose dimensions are 1.82x2.22cm, there are four of them which, ideally, should all contribute to define an average signal. This means having 12 pads, such that the final overall chip layout is the one reported in Fig.25.
Moreover, to enhance the reliability of the system and ensure the test is done whenever the chip is correctly loaded, two additional top and bottom gold tracks have been inserted. These two short-circuits are connected with others tracks of the PCB placed beneath the cartridge (see section III.7). The tracks, on one side are grounded, whereas on the other are connected with a digital input of the microcontroller. If the chip is present, the digital pin of the microcontroller is grounded thanks to the rightly centered short-circuits, otherwise, if the chip is not present or is poorly-loaded, causing open-circuits, the digital input is 5V and the experiment does not start. With respect to the previous layout, where the experiment started anytime, even if the chip did not make the right contact with the connectors of the microcontroller, now the measure starts if and only if a good electrical contact is realized. Misalignments, rotations and translations of the loaded chip, which could cause a missing contact, are avoided.

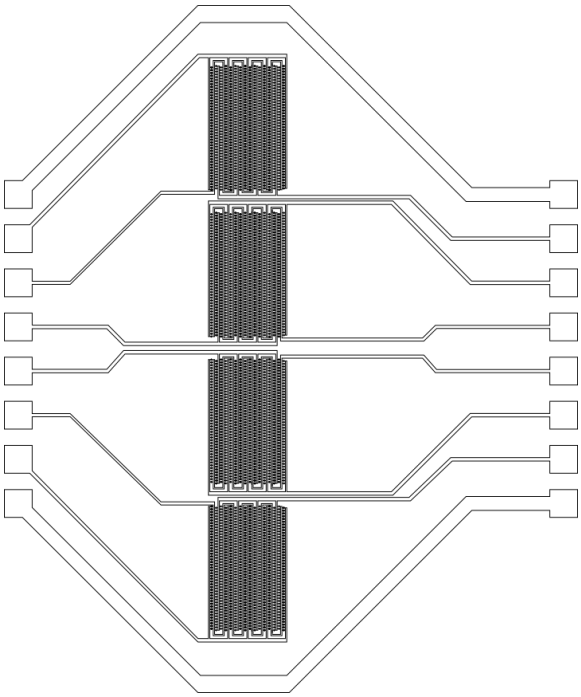

FIGURE 25. *The complete CAD drawing of the new chip layout: 4 sensitive areas are present, with relative 12 pads. Furthermore, two short-circuits on the top and the bottom have been added to ensure the correct loading of the chip within the cartridge.*

III.2. Cleanroom overview

Fabrication of the TMek chip involves three main steps: (i) the fabrication of the Ni pillars array, (ii) the fabrication of the Au electrodes and (iii) a third photolitography step to cover the electrical connections to the electrodes with an insulating polymer, so as to reduce the electrode capacitance and resistance (C_{sol} and R_{sol}).
The chip fabrication was performed in the cleanroom of *PoliFAB*, the micro and nanotechnology center of the Politecnico di Milano [88].
A cleanroom is a facility built and designed with the goal to minimize the presence of particulates such as dust, vaporized particles and any kind of external and disturbing organism. Cleanrooms typically have a cleanliness level quantified by the number of particles per cubic meter with a predetermined size; as stated by *ISO (International Organization for Standardization)*, the maximum concentration of particles C_N over $1m^3$ per class N and per particle size D (in µm), can be calculated with the following formula [89]:

$$C_N = 10^N \left(\frac{0.1}{D}\right)^{2.08} \tag{III.1}$$

In PoliFAB, the cleanroom is divided in two adjacent areas: the first one is a class ISO06 area ($150m^2$) and is equipped to perform optical lithography, electron beam

lithography, wet and dry etching, thin film deposition etc., while the second one ($220m^2$) is a class ISO08 area where processes such as electroplating and others less clean-demanding can be carried out [88].

III.3. Nickel concentrators fabrication

The microfabrication processes needed to fabricate the array of Ni pillars involved in attraction and localization of paramagnetic particles are: (i) *photolitography* to pattern the Si wafer, (ii) *reactive ion etching (RIE)* to excavate cavities, (iii) *electron beam evaporation* to deposit nickel and silicon dioxide, (iv) *electroplating* to fill the cavities with nickel, and finally (v) *polishing* to remove the material in excess over the wafer. Some of these will be then used again in other fabrication steps which consists in the making of gold electrodes first and SU8 deposition to complete the chip.
Here's a brief run sheet (see Fig.26), with related picture, that describes the fabrication of Ni concentrators: everything starts from an highly doped Si wafer which is lithographed optically to report the drawing of the cylindrical holes. These will be etched away using a RIE process; later on, Ni is deposited onto the wafer that is then cut in order to obtain eight chips per wafer. Every chip is polished, flattened and finally treated such that, above it, is deposited an insulating layer of silicon dioxide. All these steps are shown in the figure below.

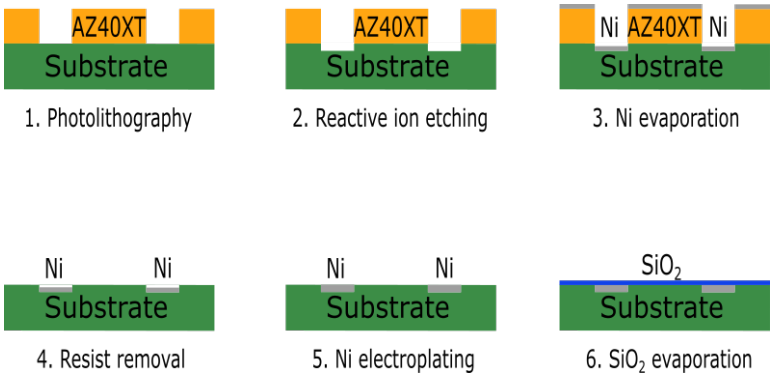

FIGURE 26. *Summary of all the steps needed for Ni array fabrication.*

III.3.1. Optical lithography. First stage involved in the fabrication of Ni concentrators is *optical lithography* (also said *photolitography*) and it comprehends a set of steps aimed to pattern features on a thin film substrate. It is the most widely used form of lithography and semiconductors industry relies almost exclusively on it: the working-principle is based on the change in solubility of a suitable polymer called *photoresist*. This quasi two-dimensional process has a limited resolution without using resolution-enhancing technologies, creating a major constraint for building miniaturized systems. Photolithography and pattern transfer involve a set of process steps: firstly there is a *lithography preparation* needed to pre-treat the sample, then, exploiting an UV light source, *exposure* is done; later, there is a *development* step and, at the end, the photoresist removal. After these first mandatory steps, other *addictive* or *subtractive* processes can follow.

The starting point to produce TMek chip is a 4-inches silicon wafer from "Si Mat" [90]: the substrate has a nominal thickness of $525 \pm 25\mu m$ and it is heavily p-doped (P+/Boron-0.005-0.025$\Omega \cdot cm$). From such a wafer, it is possible to obtain a maximum of eight chips, whose dimensions are 1.82x2.22cm.

Sample cleaning: all optical lithography steps are performed in ISO06 class environment, in particular in the "*yellow room*". In order to optimize the adhesion process, the wafer is cleaned following a standard set of steps. Firstly, it is done an ultrasonic bath at room temperature and different frequencies using, separately, acetone and isopropyl alcohol: the former is a solvent used to remove organic elements while the latter one is used to avoid damaging on the wafer by acetone itself. After that, a baking is performed at 120°C for 10 minutes on a hot plate, such that the remaining solvent molecules are evaporated.

Spin coating: as first step in the lithography process itself, a thin layer of an organic polymer, a photoresist sensitive to ultraviolet radiation, is deposited on the substrate. The photoresist is disposed onto the wafer lying on a wafer-platen in a resist *spinner* (also said *spin coater*). A vacuum chuck holds the wafer in place. The wafer is then spun at high speed and, thanks to centrifugal force, the solution flows to the edges (see Fig.27). The resulting polymer thickness T can be estimated by this empirical formula:

$$T = \frac{KC^{\beta}\eta^{\gamma}}{\omega^{\alpha}} \tag{III.2}$$

in which ω represents spin speed (rpm), C the solution concentration, η the intrinsic viscosity and K is a calibration factor influenced by acceleration, total time, etc. The spinning process is of primary importance to the effectiveness of pattern transfer. The resist film uniformity across a single substrate and from substrate to substrate must be ±5nm to ensure reproducible line widths and development times in subsequent steps [91].
Spin-coating is performed with a *Spin Coater – POLOS SPIN150i* [88] and the polymer spinned for the realization of nickel pillars, is the *AZ40XT* provided by "MicroChemicals" [92]: this is a thick and *positive resist* (see later for positive resist). The spinning is targeted to $25\mu m$ and this is achieved using a standard recipe: 2750 rpm for 45 seconds. After it, a post-bake process is fundamental to remove solvents and stress and to promote adhesion of the resist layer to the wafer: it is done through a soft ramp from 50°C to 120°C and a steady 2-minutes step at 120°C.

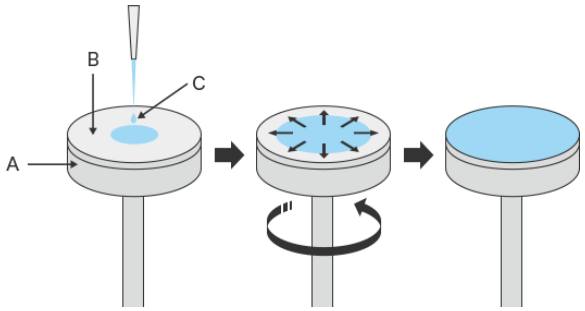

FIGURE 27. *Here is presented the spin coating principle: A is the rotating stage where the wafer or chip are put and hold through vacuum, B is the target surface, wafer or chip, and C is the photoresist, [93].*

Exposure: after bake, resist-coated wafers are ready to be moved to an exposure system where the featured pattern of the mask in transferred to the wafer. Basically, an exposure system consists of a *UV lamp* illuminating the resist-coated wafer through a *photo-mask*; also *maskless systems* are used where a direct writing of the photoresist is carried out using a LED or laser source in combination with proper optical elements. The purpose of the illumination is to deliver light with the proper intensity, direction, spectral characteristics, and uniformity, allowing a nearly perfect transfer of the information onto the resist. In photolitography, UV lamps range from short *EUV* "extreme" (10 to 14nm), to *DUV* "deep" (150 to 300nm) up to UV (300 to 500nm). One of the most typically used wavelength is the "i-line" (365nm) of a mercury lamp. The incident light intensity, whose units are W/cm^2, multiplied by the exposure time, in seconds s, gives the incident energy J/cm^2, also said *dose* D, across the surface of the resist film [94].
Radiation induces a chemical reaction in the exposed areas of the photoresist, altering its solubility, while the non-irradiated areas preserve the solubility of the photoresist itself. The principal components of photoresist are a polymer, a sensitizer and a casting solvent: the polymer changes structure when exposed to ultraviolet radiation; the solvent allows spin application for thin film targeting; sensitizers control the photochemical reaction. There exist two main types of photoresist: *positive* and *negative photoresist* (see Fig.28 below) [91].

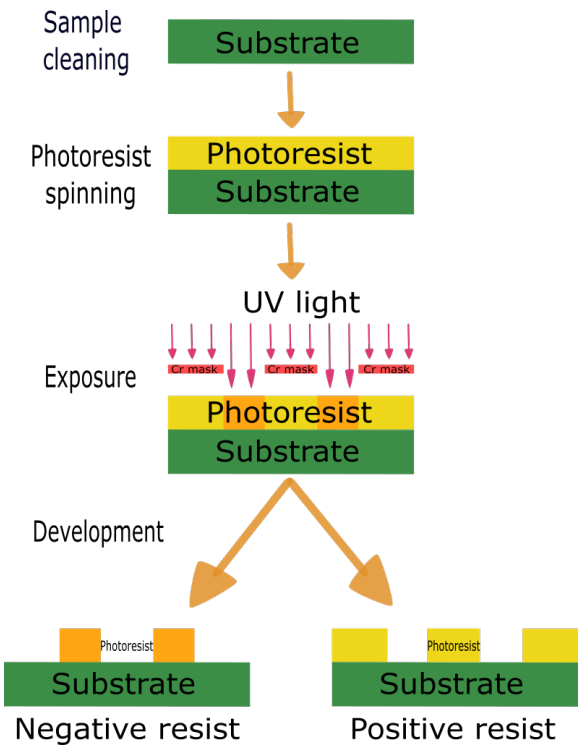

FIGURE 28. *Representation of the optical lithographic methods for positive and negative resists. Executing the same steps, lead to different results: for positive photoresists, the exposed areas are the ones that weaken, whereas for negative photoresists, the exposed areas are strengthened.*

Positive photoresists are the ones that, during the photochemical reaction, due to exposure to the UV lamp, weakens the polymer by scission of the main and side polymer chains, such that the exposed resist becomes more soluble in developing condition. It turns out that the development rate of the exposed resist is much faster (about ten times) with respect to the unexposed one and, because of this, the former areas can be removed more easily by a specific solvent solution called *developer*. Since UV radiation is attenuated passing through the resist, the deeper the analyzed area, the less the photoresist is activated: it means that at the top of the photoresist there is a higher degradation, while a minor one is expected for bottom layers, and this overcut reflects in profiles of the photoresist, typically with angles on the order of 75°-85°.
While in the above mentioned case, energy provided by the UV source is used to break the chemical bonds of the polymer, in *negative photoresists*, the exposed zones, experience a cross-linking effect (i.e. polymerization). Here, the irradiated areas are made insoluble: it follows that this insoluble layer forms a "negative" pattern.
Besides these two main classes of photoresists, it does exists another special type of photoresist which permits to obtain either *positive* or *negative* behaviour, such that

more pronounced undercut resist sidewalls and optimized lift-off processes can be achieved (see later for "lift off"): this is the so-called *image reversal photoresist*. As represented in Fig.29, this is a positive photoresist which can also exhibit negative features, if additional steps are performed, with respect to the ones already seen. In fact, with image reversal resists two more steps are necessary: after the first exposure, that would lead the material to behave like a normal positive resist, a *reversal bake* is done to invert the solubility tendencies of the material. After this passage, is then performed a *flood exposure*, which simply consists in putting the already patterned substrate under a UV source indiscriminately. Upon this treatment, exposed parts becomes insoluble and a negative behavior is obtained [92].

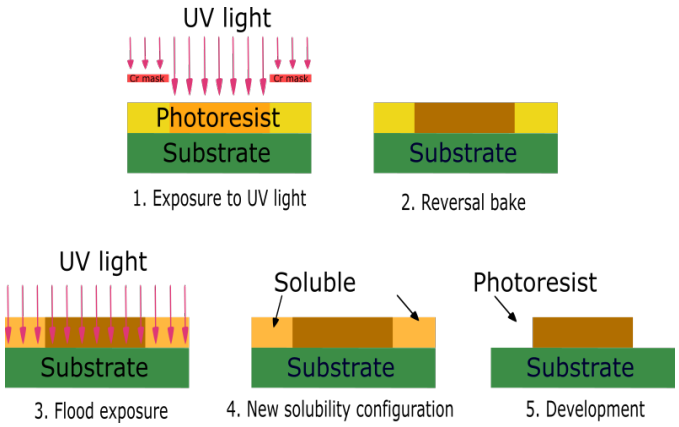

FIGURE 29. *Photolithography steps for image reversal resist, if it is intended to be used as a negative photoresist, [92].*

Talking now about the machines involved in this important photolithographic step, there are, as already said, two types of approaches to discern exposed and unexposed areas: *mask-based* and *maskless-based*. In the former case, the desired pattern, derived by a CAD drawing described in section III.1, is reported on a chromium film deposited onto a transparent quartz substrate: since Cr does not transmit UV radiation, the model is transferred on the wafer. Just as reminder, the pattern to be created on the wafer is composed by 8 replicas (the number of chips coming from a single Si wafer), and in each of them are present 8 micro-arrays with 45 circles with $40\mu m$ diameter properly arranged to define the 360 pillars of each area (see section III.1). Opto-lithography is performed using the *Mask Aligner - Karl Suss MA6*: it is equipped with a 1000W mercury arc lamp with smart power supply capable of operating in constant power mode. This machine can be used in different configurations and in our case two of them will be exploited [88]. For the fabrication of the Ni micro-arrays it is used in *hard contact mode* with a proximity gap of $20\mu m$, duration of exposition of 80 seconds, and exposure dose which is $4.2mJ/cm^2$. After exposure, the sample is subject to a post bake of 105°C for 100 seconds.
On the other hand, a *maskless* system can be used: there is elimination of photomasks from the lithographic process, and this, will increase the flexibility and

significantly reduce costs and times of the prototyping or manufacturing. A natural consequence of this approach, by the way, is the necessity of a longer exposure of the wafer inside the machine with respect to the previous case. The machinery used to achieve *maskless photolitography* is the *Heidelberg Instruments Maskless Aligner MLA100*, provided by a LED source with a power of 10W at 365nm [88]. The *MLA100* is employed in the fabrication of gold sensitive areas (i.e. electrodes) as it will be exposed in section III.4.

Development: after the bake, the wafer is left 15 minutes on another plate to cool down without causing excessive stress. Once thermalization is completed, it starts one of the most critical fabrication steps: *development*. Within *exposure*, the desired pattern has been reported on the photoresist (see Fig.28); to remove the soluble portions of the resist, then, the sample is immersed in a *developer*: for positive photoresist, exposed areas will be removed, while for negative one, the unexposed areas. So, development transforms the latent resist image formed during exposure into a relief image that will serve as a mask for further subtractive and additive steps (see Fig.30). There exist two main types of development techniques: *wet* and *dry*. Within the most used *wet development*, the privileged approach is the one represented by *wet immersion development* where the wafers are batch-immersed for a timed period in a developer bath and agitated, if needed, at a specific temperature: this is the one used in TMek microfabrication process. In particular, the wafer with the pattern of the Ni pillars is immersed at room temperature without agitating, for 120 seconds in *AZ726 MIF developer* produced by "MicroChemicals" [92]. In order to avoid over-development, a water rinsing is useful immediately after developing the photoresist.

Pattern transfer: after the patterning of the photoresist material described above, which is common to every photolithographic process, fabrication incudes two types of processes: *additive* and *subtractive* (see Fig.30). Referring to the first one: it is achieved depositing some specific material as uniform as possible onto a substrate. The additive techniques employed in TMek chip microfabrication are: *electron-beam evaporation*, *electroplating* and *magnetron sputtering*.
On the other hand, when some material has to be removed, a subtractive process is needed (bottom of Fig.30): in case of TMek the *reactive ion etching* is used to drill cylindrical holes from the Si substrate.

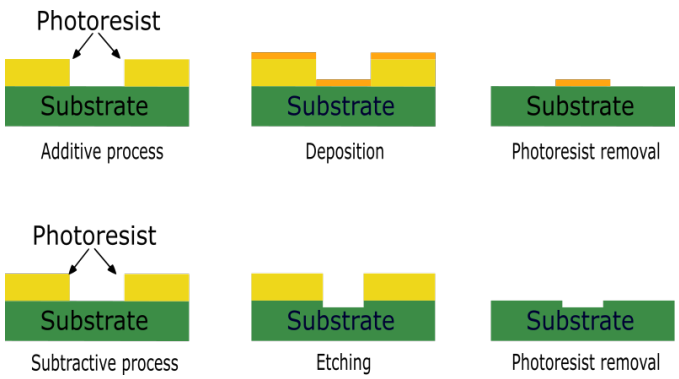

FIGURE 30. *At the top, is reported the additive process, whereby a material is deposited and lifted up (i.e. lift-off); at the bottom, instead, is represented the principle of subtractive procedure. Both of them are executed after that the pattern has been transferred to the resist.*

III.3.2. Reactive ion etching. *RIE* is a type of etching which belongs to the class of *dry etching techniques*. The more relevant difference between *dry* and *wet* methods, is the fact that dry etching removes the material from the wafer *anisotropically* (i.e. directionally), whereas wet etching does that *isotropically*. Dry etching corresponds to a family of methods by which a part of solid surface is dislodged within the gas or vapor phase: this can happen *physically* by ion bombardment, *chemically* by a chemical reaction through a reactive species at the surface, or by combined physical and chemical mechanisms.
RIE is a dry etching technique, which exploits a chemically reactive plasma, generated in vacuum by an electromagnetic field, to remove material from the wafer surface; the removal is due to high-energy ions of the plasma itself. Therefore, its working principle is based on the acceleration of ions towards the wafer, which results in a removal of the wafer by the interaction of gaseous species and the substrate. RIE is a synergistic process between chemically active species and energetic ion bombardment and this permits RIE to be faster than either pure physical ion bombardment or spontaneous chemical etching [95]. Arguably from what said before, since ion bombardment is highly directional, RIE has anisotropic feature with nearly-vertical sidewalls and can work with high aspect ratio structures. This technology, relying to the case of dry etching, has an etchant reaction which results in volatile products:

$$\text{Solid} + \text{Gaseous etchant} \longrightarrow \text{Volatile products}$$

Among the most widely used etch species there are SF_6, CH_4, CHF_3, C_4F_8, and many others obtained with halogens.

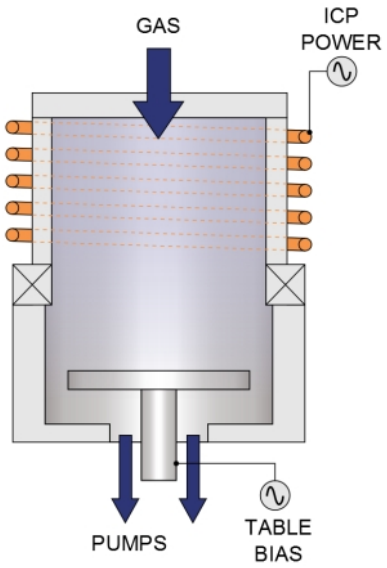

FIGURE 31. *An illustration of an ICP reactive ion etching. The table bias (i.e. sustrate holder), is stimulated with a RF signal and the vacuum chamber as well, such that the plasma can be generated, [96].*

In a typical RIE equipment (see Fig.31), the wafers are placed on top of a substrate holder electrically insulated by the cylindrical vacuum chamber where it is placed. Through small top-inlet, the specific gas enters the vacuum chamber and via another bottom-outlet, it exits the chamber thanks to the pump system. Inside the just mentioned chamber, pressure ranges from a few mtorr to few hundreds. In order to achieve plasma inside the chamber a strong electromagnetic radio frequency RF is applied. The RF signal can be ignited with a *CCP* system (i.e. capacitive coupled plasma) or an *ICP* system, (i.e. inductively coupled plasma): this latter one, has one or two orders of magnitude higher plasma density with respect to the former. Also the substrate holder is biased with a RF signal, CCP-generated this time. This process is cyclical, which means that, in every cycle, electrons are electrically accelerated up and down, while more massive positively charged ions are less influenced by the RF electric field. In their motion, electrons can be absorbed into the grounded chamber wall, or in the sample, leading to an overall positively charged plasma: this results in an high voltage difference. Because of the large ΔV between the holder and the gas, high-energy ions are directed versus the wafer and etch it. Due to both "*physical*" *kinetic energy*, either *chemical interaction* with the surface (i.e. selective erosion caused by chemical reactions between ions and surface atoms), some material can be removed.
Aspect ratios, in the typical RIE technologies, are limited to 2:1; so, a more efficient etching technique has been developed, *DRIE (Deep Reactive Ion Etching)*. This provides higher anisotropic processes up to an aspect ratio of the order of 20:1, which reflects in deeper steep-sided holes [91]. In order to perform DRIE, it cannot be followed a straightforward recipe; in this regard, one of the most used approach

is *Bosch Process* [94]. Its principle is based on alternating etch and passivation steps. The etching gas that creates fluorine radicals in high-density plasma is, in our case, SF_6. After the etch step, a thin fluorocarbon film is deposited from C_4F_8. This film passivates the surface and prevents etching. At the beginning of the next etch step, the fluorocarbon film is removed from horizontal surfaces, but sidewalls remain passivated. The SF_6 etch step is not fully anisotropic, but the polymer is etched preferentially from the horizontal surfaces due to ion bombardment and the sidewalls remain protected. The repetition of etching and passivation steps results in vertical sidewalls. Etching and passivation pulse times ranges around 5 to 15 seconds. Etch rate, anisotropy and selectivity are all influenced by the duration and overlap of the etch and passivation pulses.
RIE represents the only micro-subtractive fabrication step in the realization of the TMek chip; in particular, it is applied to the wafer patterned with AZ40XT through the photolithography by the *Mask Aligner - Karl Suss MA6*. Indeed, the parts of wafer where holes will not be present (i.e. surface not etched), have already been masked with AZ40XT in the previous lithographic process. Focusing to the machine used to perform RIE, it is a *RIE ICP – Oxford Plasmalab 100* [88]: it works at 2.4MHz and an RF power of 2500W. Since the aimed holes, which represent the forerunners of the Ni pillars, must have a depth of $20\mu m$, a Bosch recipe with cycles of 12 seconds for SF_6 and 7 seconds for C_4F_8, is done. The overall process lasts about 2 hours, for a total of 160 cycles. Later, in subsection III.3.4, it is possible to see a SEM image of a cylindrical cavity excavated by RIE (see Fig.34A).

III.3.3. Electron-beam evaporation. Once the holes have been etched, is time to fill them with nickel. This additive step is performed exploiting two separate steps: first process used, is the *electron beam evaporation (EBE)*, and it is followed by *electrodeposition* that will be later explained (see next subsection).
Electron-beam evaporation is a form of physical vapor deposition (EBPVD or even EBE) widely used to grow different materials, both dielectric and insulating. The setup is illustrated in Fig.32. The evaporation of the material of interest takes place under high vacuum, typically around $10^{-5}Pa$ or lower pressure. The material is heated thanks to the energy transferred by an electron beam focused on its surface. The electronic beam is generated through thermionic effect [97]. The filament is located in a region outside the deposit zone, in order to avoid any kind of contamination and the electrons are focused and directed toward the material with magnets.
When the vapour pressure of the material in the crucible is high enough, a sizable flux of atoms towards the substrate is established. Atoms in gaseous phase, travel from the holding crucible to the sample surface where they precipitate and deposit as a solid. Since the trajectories of the atoms must be as linear as possible, the high vacuum in the chamber is fundamental: thus, it follows a remarkable anisotropy (i.e. directionality) in the deposition of the material, which makes EBE ideal to coat regions uncovered by photoresist without sizable deposition on the resist sidewalls.
The deposition rate depends on many variables: the distance between the crucible and the sample, the evaporation rate of the material to be deposited and, strictly related, the power of the electron beam. This power, with a closed-loop system, can be controlled looking at a finely tuned quartz crystal, whose oscillation frequency

is monitored to measure the speed of evaporation and the deposited thickness.
In PoliFAB, the machinery meant to perform electron beam vapor deposition is *E-beam Evaporator – Evatec BAK 640* [88]: it has six crucibles, which means, potentially, a multi-layer deposition during the same process. In any case, for the presented chip, only Ni is deposited. As anticipated, high directionality is critical for TMek's chip fabrication: EBE process, in fact, is exploited in order to deposit an horizontal *seed layer* of nickel at the bottom of the cylindrical cavities of the micro-array, thus working as seed layer which favors the filling by electroplating from the bottom. The reason for this, is that, although electron-beam evaporation reveals itself fundamental, its deposition rate, being around $0.1nm/s$, is too low to fill a cavity $20\mu m$ depth; thus the faster electrodeposition is used to continue the process. In our process, EBE is just used to deposit 30nm of Ni inside the pillars.

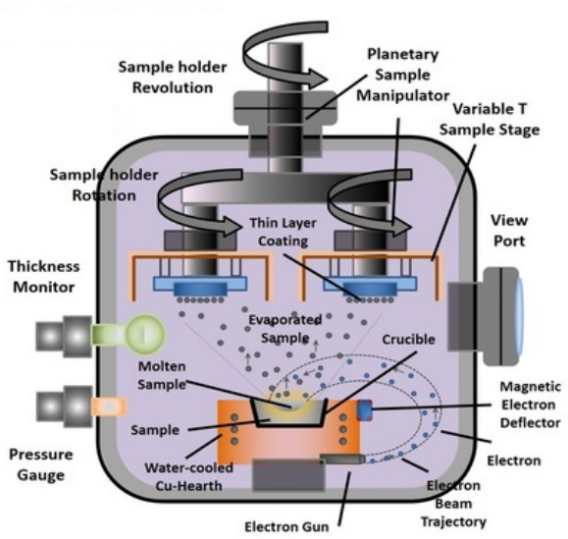

FIGURE 32. *A detailed image depicting the basic elements of EBE machinary, [98].*

III.3.4. Electrodeposition. After that EBE process is accomplished, a 30nm seed layer of Ni is present in the cylindrical $20\mu m$ deep silicon holes. The following step consists, thus, in depositing the remaining nickel needed to fill the cavities, and this is achieved using an additive process: *electrochemical deposition*. Electrochemical deposition is a process by which, a thin and tightly adherent desired coating of metal or oxide, can be deposited onto the surface of a conductive substrate by electrolysis of a solution containing the desired metal ion or its chemical complex. Since it is possible to easily manage the parameters of the process, this technology is widely used, not only in microfabrication, but also to modify some physical properties of the materials, for example against corrosion and heat.
The process, to be executed, needs an electrolytic cell that drives a non-spontaneous redox reaction (i.e. exchange of electrons between two chemical species) by applying a proper voltage bias, which can be continuous or pulsed. The fundamental components are two electrodes, one positively charged called *anode* (also "counter

electrode") and one negatively charged called *cathode* (also "working electrode"), and also an electrolyte, a solution where positive and negative ions are dispersed such that conduction of electricity can take place. Anodes are usually made of the material to be deposited, so, when a current i starts flowing, anodes will consequently dissolve, leading to the formation of free ions M^{n+} which will move towards the negative supplied cathode. In correspondence of the cathode, where the sample is placed, metal ions are reduced by as many electrons, such that it is reached the zero valence state of the metal to be deposited:

$$Me^{n+} + ne^- \longrightarrow Me^0$$

On the other hand, at the anode, metal atoms are oxidized such that Me^{n+} are formed and ne^- as well; these free electrons, sustained by the battery, contribute to the external electrical current. Alternatively, metal ions can come from metal salts added to the electrolyte solution. The basic setup to perform electroplating is reported in Fig.33 below.

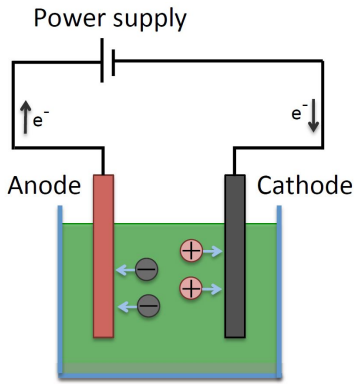

FIGURE 33. *Schematic of the electrolytic cell working principle, [50].*

Referring now to TMek specific case: here the dealt metal Me is nickel, whose oxidation number is $n = 2$. The Si wafer, and also the Ni seed layer, need to be biased negatively, such that the current is sustained and the reduction too.
A key factor characterizing this technique is deposited thickness T. As stated by M. Faraday [99], this parameter is strictly related to many others: time t, current i, surface area to deposit S, atomic weight of the material to be deposited A and its density ρ, valence of the dissolved metal n and Faraday's constant F whose value is $96485.309 C/eq$. The formula relating all these elements is:

$$T = \frac{A}{nF\rho}\frac{it}{S} = \frac{A}{nF\rho} jt \tag{III.3}$$

where it has been introduced the current density j. Since $A/nf\rho = \beta$ is constant, thickness T is proportionally linked with current density and deposition time. For Ni, $\beta = 3.4 \cdot 10^{-5} cm^3/C$, since $A = 58.7 g/mol$, $n = 2 eq/mol$ and $\rho = 8.908 g/cm^3$. It follows that, having j in mA/cm^2, the resulting deposition rate T/t in $\mu m/hour$ is:

$$\frac{T}{t} = 1.22 j \tag{III.4}$$

Before electroplating, is necessary to process the wafer through a *lift off* procedure in order to remove AZ40XT photoresist with the useless seed layer above; this is done immersing the wafer in a hot beaker filled with *universal photoresist stripper*, i.e. AZ100Remover furnished by "MicroChemicals" [92].
The setup employed for the electrodeposition is a 4-inches *silicon wafer plating set* furnished by "Yamamoto MS" [88]. The system permits the deposition of Ni on the whole wafer where Ni seed layer is already present. Inside the 4L-including tank, apart of the cartridge hosting the wafer and acting as the cathode, there are an holder for the anode, a temperature sensor, a heater, a liquid-level sensor and an agitator; disentangled with these objects, there is a mini-filter which processes the *Nickel Sulfammate* solution furnished by "ATOTECH" [100], fundamental for providing the necessary ions of the redox. Moreover, to avoid the formation of air bubbles inside the cavities, a nitrogen gurgle is constantly kept inside the tank. The external current is supplied by a waveform generator (*Agilent-6614C*).
The experiments of deposition are conducted with a temperature T inside the tank of 50°C and, imposing a DC $j = 8 \cdot 10^{-3} A/cm^2$ for about 3 hours, it can be achieved the final $20\mu m$ of Ni growth inside the holes; it is much more than the 2 hours predicted, but is mainly due to overfilling, non-ideal current distribution and a low efficiency of anode and cathode used. Along the electrodeposition, two main unsuccessful events can take place: the growth of a protruding amount of Ni inside the cavity, the so-called "nickel mushroom" (see Fig.34), or, on the contrary, the "tip effect", which causes a major thickness deposition on the side walls rather than the center. This is the reason why next subtractive technique is fundamental: the *polishing*.

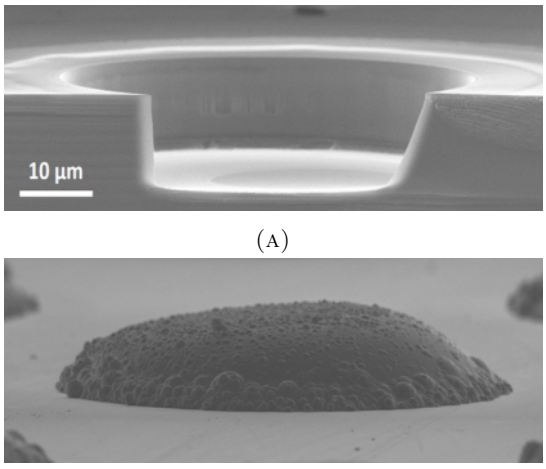

(A)

(B)

FIGURE 34. Image *(A) at the top is a SEM side view of a cavity excavated by RIE; (B) represents the same side view after the cavity has been filled by Ni with the characteristic "mushroom effect", [51].*

In addition, after this process, since there is not a mechanical polishing machine for 4-inches wafers, there is an important conceptual shift: the wafer, indeed, must

be cut, thanks to four crosses, lithographed for each of the eight chips, such that, from now on, every single microfabrication step will be intended for just one single chip and not the wafer anymore.

III.3.5. Polishing. Because of the above mentioned outgrowths, a *polishing* step is required after electrodeposition. This is a "macroscopic" subtractive process used to flatten as much as possible the surface of the wafer and the Ni cylinders embedded. The process of polishing, usually employs *abrasives* pads or power, at first, coarse and then gradually finer.
At PoliFAB, the machinery capable of doing polishing is the *fiber optic polishing machine sfp-550* by "SEIKOH GIKEN" [88]. This setup, initially used to deal with optical fibers, has been converted introducing a holder for the single chip, which is attached to it through a double sided adhesive. The holder is then put in contact to the top of the machine rotating pad. First, it is employed a gross sandpaper and some water as lubricant; then three passages, 10 minutes each, of a permanent diamond suspension are performed, with the diameter of diamonds changing, from $3\mu m$ to $0.25\mu m$ up to $0.1\mu m$. At the end, the chip is planar with some unavoidable scratches that do not affect subsequent processes if the total roughness is kept below 10nm. In Fig.35 is represented the resulting appearance of the Ni concentrators until this fabrication step.

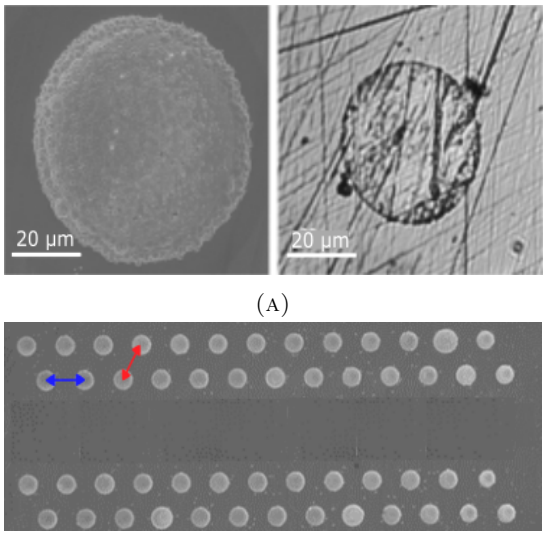

(A)

(B)

FIGURE 35. *(A) is a top view of a Ni concentrator before ("mushroom effect") and after (planar) polishing process, with relative scratches due to the macroscopic intrinsic limits of the procedure, [51]. (B) represents a top view of the final result of the Ni fabrication process. The blue arrow has a length of* $80\mu m$*, while the red one of* $140\mu m$*.*

The last process to complete the fabrication of the array of Ni concentrators, relies in the deposition of an insulating layer of silicon dioxied SiO_2 with thickness

equal to $3\mu m$. This is a key passage since (i) favors the gold electrodes to be insulated from the underlying Ni pillars and (ii) favourites an additional planarization of the chip surface that will lead to a better adhesion of gold and an optimized photolitography process. As for Ni, also the deposition of SiO_2 requires two steps: a first seed layer of 50nm is evaporated exploiting the aforementioned EBE technique (see subsection III.3.3). The final $3\mu m$ deposition is made using a *plasma enhanced chemical vapor deposition (PECVD).*

III.4. Gold electrodes fabrication

In the previous sub-chapter has been demonstrated the fabrication of the hexagonal micro array of Ni concentrators involved in the magnetic capture of HCs and i-RBCs. Once these corpuscles have been attracted, they need to be counted through impedimetric measurement, and this is performed by gold electrodes, whose design and geometry has been explained in section III.1.
When the 1.82x2.22cm chip has been completed for the first phase, before passing to the following one, has to be cleaned. This passage is performed, as seen for the wafer itself, both with acetone and isopropyl alcohol in ultrasonic bath. In this case, to enhance the cleaning of the sample, a *plasma cleaning* process is also used. Plasma cleaning is the process of removing all organic matter and contaminants from the surface of an object through the use of an ionized gas, i.e. plasma. It is usually performed in vacuum chamber using oxygen and/or argon gas. Plasma is extensively used in microfabrication, since (i) it does work for a large range of materials (e.g. metals, plastics, glass etc.), (ii) no hazardous chemical solvents are necessary, but suitable gas, and (iii) the processing eliminates all unwanted by-products and organic compounds. PoliFAB is equipped with *Plasma Asher – PVA TEPLA 300 AL* in which plasma excitation is performed by means of 1000W microwave power supply and the substrates are processed at a pressure of 0.6–1.5mbar [88]. The generated chemical radicals react with the substrate surfaces and create volatile products which are extracted by the vacuum pump. The most widely used gas is oxygen and that is the one employed to execute cleaning upon TMek's chip: so, an O_2Plasma at 200W for 120 seconds is used.
As for the Ni pillars processes, in Fig.36 a run sheet of the steps needed for gold electrodes fabrication is presented: first there is a lithographic passage to pattern the image reversal AZ5214E photoresist and, once developed, chromium and gold are deposited and lifted off. After that, SU8 needs a third lithographic procedure and, at the end, the back of the chip is sputtered with Au.

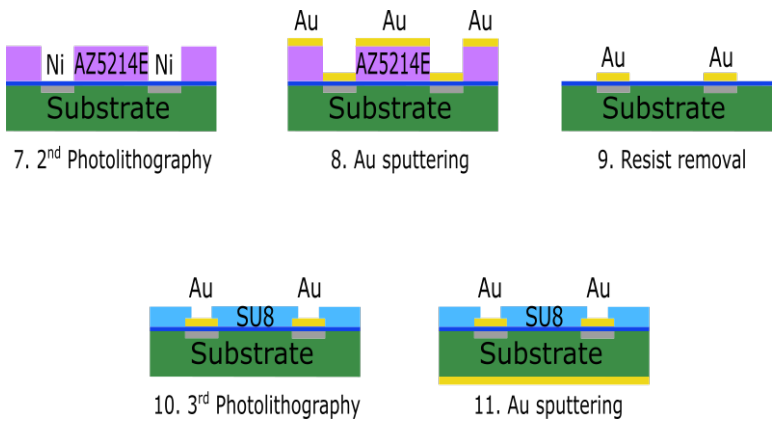

FIGURE 36. *Summary of the steps needed for the gold electrodes fabrication, followed by the optical lithography needed by SU8 and, at the end, a back-sputtering of gold useful to reduce SNR.*

III.4.1. Optical lithography. Once the surface has been properly treated, a second lithographic process is performed. To improve the adhesion of the AZ5214E photoresist that will be used for the electrodes, onto the substrate is first spin-coated an adhesion promoter, i.e. *TI PRIME* by "MicroChemicals" [92]. Just after a bake procedure (i.e. 120°C for 120 seconds), is possible to spin the image-reversal AZ5214E photoresist (see section III.3.1). Is important to assure, before spinning the photoresist, that bubbles of air are absent, in order to maximize the homogeneity of the resulting structure. After this, and a default soft bake (110°C for 90 seconds), the chip undergoes the fundamental step of exposure. In contrast to the fabrication of Ni pillars, for the electrodes is used the more versatile maskless lithographic machine. This permits to expose every time different regions of the chip, thus a different design can be reported each exposition process. In this thesis work, two separate designs have been developed and exposed: the first, *C1*, with interpenetrated electrodes of measure and reference and annular shape of the electrodes themselves, and the second, *C2*, still interpenetrated electrodes, with the more articulated structures displayed in Fig.24B,C. However, the fabrication parameters of these two models, and all the steps processes, are the same.
The machinery used is the aforementioned *Heidelberg Instruments Maskless Aligner MLA100* [88]; the exposure dose is $35 mJ/cm^2$ and is immediately followed by another lithographic passage employed in the so-called *draw-mode*, whereby specific circular patches are exposed onto defects of the substrate to eliminate possible short-circuits. Being an image-reversal photoresist, AZ5214E needs a reversal bake after exposure, and this consists in 90 seconds at 115°C. When this is finished, is opportune to wait thermalization of the sample, that, after, undergoes, through the *Mask Aligner - Karl Suss MA6*, a flood exposure reversal process: within this, the chip is exposed, for 80 seconds, to a default flood exposure recipe. The reason why a negative-behaving photoresist has been preferred, is the following: using a negative photoresist allows to achieve an angle between the side-walls of the photoresist and the substrate smaller than 90°, whereas using a positive photoresist would lead to an obtuse angle in the profile. Therefore, having a type of profile such as the

latter one, would give problems in terms of deposition (i.e. links between material deposited on removed area and photoresist) and lift off (i.e. within positive photoresist case, there are no points of attack for the developer to dissolve the resist itself).
The final crucial step to complete this lithographic process, is represented by the development: the developer used is the AZ726MIF [92], in which the chip is immersed for 20 seconds and kept in smooth agitation. Is important, immediately after the removal by the solvent, to rinse the chip by water and dry it by N_2 gun.

III.4.2. Magnetron sputtering. The chip is now ready to undergo the metal deposition process. This is performed using *magnetron sputtering* technology, and it is used twice: first, a thin adhesive layer of chromium Cr, followed by the actual metallic contact, represented by a thicker layer of gold.
Sputtering is a physical vapor deposition technique (PVD) used to deposit thin films on a substrate [91]. On an atomic level, sputtering is the process whereby, a gaseous plasma (see section III.3.2) is created and its charged particles are highly accelerated, such that they result in a bombardment on the target material; it is then eroded, and the ejected neutral particles (e.g. atoms, clusters of atoms or molecules) will be directed towards the substrate to be coated. Sputtering process begins when a substrate to be deposited is placed in a high-vacuum chamber containing a inert gas, usually argon, and the target source (i.e. the material that will be bombarded) is negatively biased. Due to the electric field near the interface, free electrons are accelerated out of the target, colliding with the outer electronic shell of the Ar atoms and leading to their ionization, such that Ar^+ are formed. These positively charged particles are then highly accelerated versus the target with opposite charge, striking the surface and releasing source material and more free electrons due to the conservation of momentum within the collision. These particles, then, cross the vacuum chamber and are deposited as a thin film of material on the surface of the chip. There are several types of power sources to bombard the target material and sputter atoms, including DC and RF sputtering which are the most widely used. *Direct Current (DC)* sputtering is the simplest and usually employed with electrically conductive target materials like metals; on the other side, *Radio Frequency (RF)* sputtering uses an AC voltage at radio frequency to avoid a charge build up and can be used for most types of insulating coatings [101].
Because ions are charged particles, exploiting Lorentz force, a magnetic field can be used to control their velocity and behaviour, as in *magnetron sputtering* (see Fig.37 below). This technique uses magnets behind the negative cathode (i.e. target) to trap electrons over the negatively charged material, in such a way that they are not free to bombard the substrate. This allows to avoid overheating or damage to the object to be coated. Meanwhile, since the electrons have confined trajectories above the cathode, their probability of ionizing neutral Ar atoms is enhanced by orders of magnitude.

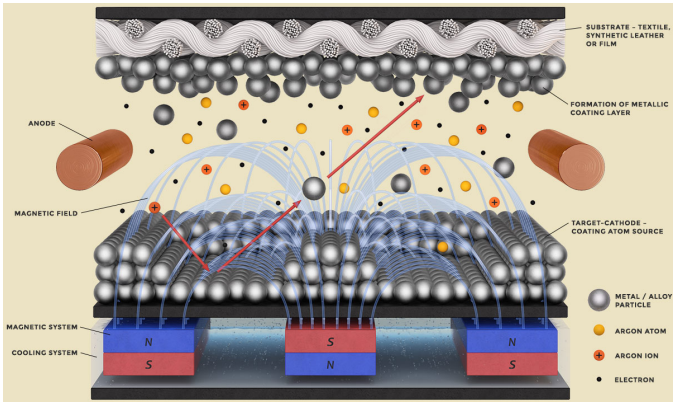

FIGURE 37. *A representation of the basic principles underlying magnetron sputtering process, [102].*

During the device fabrication, the system used to execute magnetron sputtering was a *Leybold-Heraeus LH Z400 MS* [88]. For the metal deposition, a first adhesion layer of Cr (30nm thick) is deposited on the chip, at a pressure of $2 \cdot 10^{-5} mbar$ followed by 200nm of gold for the electrical contacts. During Cr deposition the Ar flow is 70 SCCM (i.e. Standard Centimeters Cube per Minute) and the deposition rate 12nm/min. For gold the deposition rate at 50 SCCM flow, is 28.5nm/minute. To enhance the adhesion of Cr on the substrate, another "activation" process with O_2 plasma is performed with the *Plasma Asher – PVA TEPLA 300 AL*, for 8 minutes at 200W.
Once the deposition steps are done, the *lift-off* process is carried out by putting the chip into an acetone-bath and leaving it for some minutes, till the dissolution of the resist in the exposed regions lifts the gold overlayer.

III.5. SU8 deposition

To finalize the chip fabrication, two additional steps are required: first, the deposition of a passivation layer made of *SU8 photoresist*, followed by another gold deposition on the back of the chip.
SU8 is a commonly used negative photoresist, whereby the parts exposed to UV become tighter bounded and less soluble if immersed in the developer. With SU8, the goal is to cover all the chip, but the sensitive parts (i.e. electrodes regions) to reduce the electrode resistance/capacitance and increase the percentage variation induced by the RBC-capture. Furthermore, the photoresist does not allow blood to cover gold tracks, which could lead to supplementary noise, degrading the *signal to noise ratio (SNR)*. After sample cleaning with ultrasonic bath of acetone and isopropyl alcohol; then, the photoresist (SU8-2005 by "MicroChemicals") [92] is spin-coated with a target of $5\mu m$ thickness and soft-baked with up and down ramps from 65°C to 95°C. Because of photoresist negative feature, the mask, loaded in the *MLA100* performing the exposition, represents the negative of the regions where the SU8 will remain, so the majority of the surface. The exposure dose employed is $630 mJ/cm^2$. The development takes place in the proper *SU8 developer*, where exposed chip is left for about 40 seconds. A final hard bake treatment is done to stabilize as much

as possible the passivation layer: a first ramp from 50°C to 200°C, then, 10 minutes at 200°C and, at the end a descending ramp to 95°C.
In order to minimize the capacitive coupling between the gold electrodes tracks through the Si substrate, and consequentially maximize SNR, a layer of 200nm-thick by gold is deposited on the back of the chip. In this way the back of the chip can be efficiently grounded and parasitic currents through the silicon substrate do not enter the virtual ground of the transimpedance amplifier (see section IV.2).
The chip fabrication is completed and the final result is showed in Fig.38A. The rainbow-coloured effect is given by a further coating by the *MCP-4 polymer* by "Lucidant Polymers" [103], whose aim is to improve the surface hydrophilicity, such that a better adhesion of the liquid sample, made by blood and PBS (and optionally plasma), can be possible. After a first immersion in the above cited polymer, the chip is put in a blocking solution which avoid non specific binding by saturating functional groups [104].

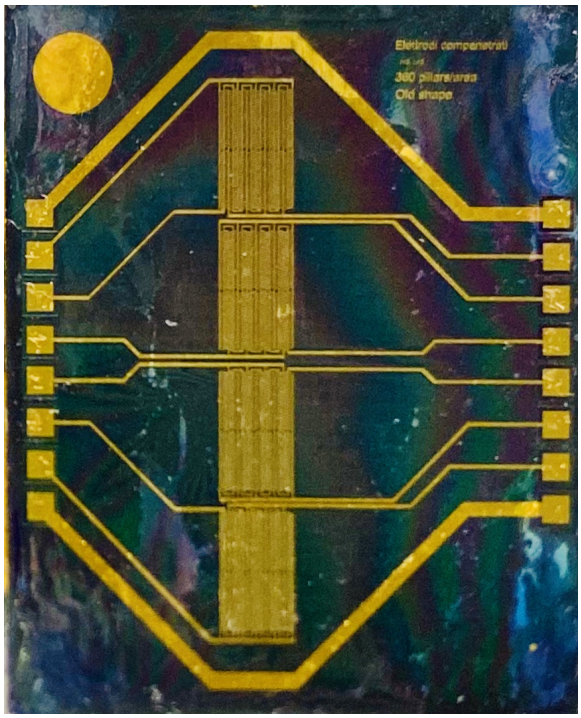

(A)

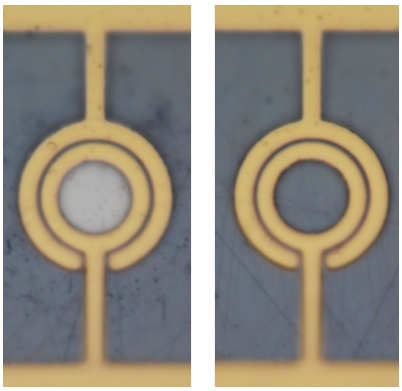

(B)

FIGURE 38. *(A) Picture of a finalized TMek chip. The rainbow-coloured effects is due to the polymer which promotes an higher hydrophillicity of the surface. The gold circle in upper left-corner is useful for the correct loading in the cartridge that will be explained later (see section III.7); in figure (B) a zoom of the electrodes lithographed above Ni pillar for the measurement signal (left) and for the reference signal (right).*

III.6. Electronic design

In this section, a focus on the electronics used in TMek to measure impedance variation and report this value to a system of analysis is presented. The impedimetric detection is performed by a custom circuit board designed by the *"I^3N group"* of Politecnico di Milano.
It is important, first, to wrap up what said in sections II.4 and III.1. Indeed, in the chip are present four pairs of measure and reference areas allowing to perform a differential measurement to get rid of the common mode fluctuations.
Two counter-phase sinusoidal voltage signals at 1MHz (see section II.4) are generated by a direct digital synthesizer (DDS) and supplied, through spring contacts, to the measurement and reference electrodes of the four sensors. Each measure or reference area can be seen as a resistor, so a sensor can be modeled as a series of two resistors (i.e. "R_M" and "R_R"), of about 150Ω. The virtual ground *transimpedance amplifier (TIA)*, with *feedback resistance* $R_f = 1K\Omega$ ($G = 1000$), is connected to the central node of the sensor (i.e. common "C"). If the impedances of measurement and reference are equal (i.e. no net signal present), no current is measured by TIA.

III.6.1. Balancing the starting condition. Before each experiment, an automatic tuning of the counter-phase voltages applied to the reference and measure electrodes is performed: this is done in order to get well-balanced initial condition, where a negligible current is flowing in the virtual ground even though the resistors R_M and R_R are not identical because of fabrication non-idealities. The underlying principle consists in applying, if necessary, two different potentials to the resistors R_M and R_R. In order to maintain $I_M = I_R$, which results in $V_{out} = 0$, for $R_M = \alpha R_R$, the voltages will have amplitudes V_M and $V_R = -V_M/\alpha$ (see Fig.39).

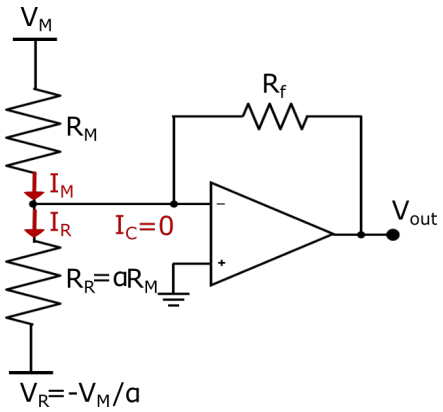

FIGURE 39. *Before every experiment, a fine tuning of the voltages applied to the pads of measure and reference is done, such that, if the resistances are not perfectly equal, the current flowing through the TIA can still be zeroed. In the general case, if $R_M = \alpha R_R$ it follows that, to get $I_C = 0$, the voltages will be related in this way: $V_R = -V_M/\alpha$.*

On the other hand, as schematized in Fig.40, during the experiment, the magnetically captured i-RBCs or HCs, which for frequencies below 10MHz are approximately insulators (see section II.4), cause a percentage variation in the resistance of the sensor ΔR and, consequentially, an unbalance of the current amplified by TIA, returning $V_{out} \neq 0$.

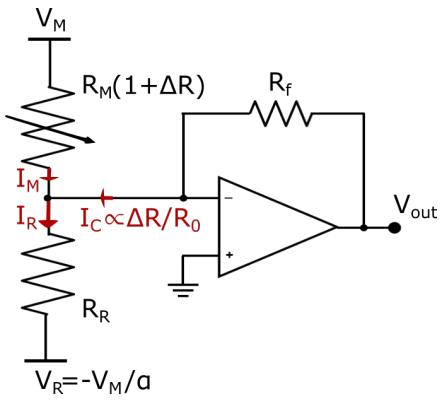

FIGURE 40. *If an i-RBC is captured, being an insulator cause a variation in resistance which, in its turn, causes a variation of current flowing through the TIA: this results in a* $V_{out} \neq 0$.

In the ideal case, assuming an equal magnitude V_{bias} of the applied signals V_M and V_R, as well as identical initial impedance R_0 ($R_0 \simeq R_M \simeq R_R$), both in measurement and reference regions, if ΔR is the percentage variation related to corpuscles, the change of current at the common node (assuming $\Delta R/R << 1$) will be:

$$\Delta I \simeq \frac{V_{bias}\Delta R}{R_0^2} = \frac{V_{bias}}{R_0}\frac{\Delta R}{R_0} \tag{III.5}$$

where $\Delta R/R_0$ is given by equation II.37. It turns out that the current variation at the virtual ground or, equivalently the TIA output voltage variation, is proportional to the volumetric fraction of captured corpuscles in which has been displayed its proportionality to the volumetric fraction Φ.
As discussed above, in order to avoid electrochemical reaction of the interface between the electrode and the liquid, the amplitude of the sinusoidal voltage signals applied to the electrodes, is limited to 100mV.

The output of the TIA is then amplified by a PGA with variable gain ranging from 0.8 to 10. After this, the output of PGA is multiplied, through an analog multiplier, with a reference signal generated by the same DDS that also provides the stimuli for the sensors. The resulting signal is then low pass filtered at 100Hz to implement a lock-in amplifier.
The LIA system just described, in TMek is implemented by a custom electronic board realized with discrete components on a *printed custom board (PCB)*, which converts the LIA output in a digital format; then, using a microcontroller Arduino, data are sent, via USB, to a PC in that performs data analysis. Further details about the setup and the analysis will be displayed in the following sections.

III.7. Experimental setup

The experimental setup consists of two components: a disposable cartridge (see Fig.41A) and a reader (see Fig.41B). The former, made by 3D printing, has two housings: for the placement of the chip and for the PDMS gasket in which the blood sample is placed. The cartridge lid holding the chip is closed putting in contact the chip with the spacer on top of the glass slide, thus defining a closed chamber between the chip and the glass slide. Two rows of spring contacts [105] mounted on a PCB placed underneath the cartridge realize the electrical contact with the pads of the chip. The mechanical setup of the reader presents a lodging for the cartridge insertion and connection to the electronic board, which is positioned on the rear of the setup. A stepper motor, by "Physical Instruments" [106], attached to the structure, allows to position permanent magnets at about $50\mu m$ from the chip back surface or remove them.

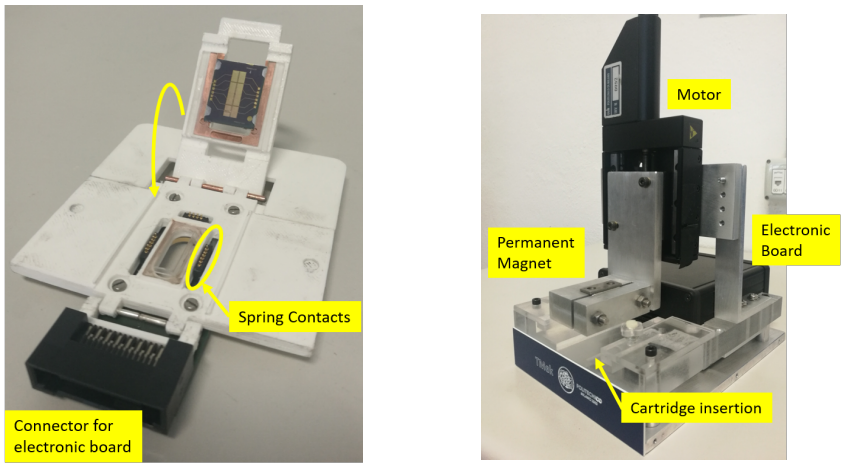

(A) (B)

FIGURE 41. *(A) is a photo of the cartridge where the chip and the blood sample are loaded. When the cartridge is closed, and a microfluidic chamber is performed, it is inserted within the reader (B), such that the experiment can start.*

III.8. Data analysis

Once the resulting signal from the LIA has been acquired and sampled by an ADC, the microcontroller (Arduino Due), sends the acquired data, via USB connection, to a computer. A custom app, developed in MATLAB using App Designer, allows to set the measurement parameters (see section IV.1), start/interrupt the experiment, visualize on real time the test output and perform the data analysis.

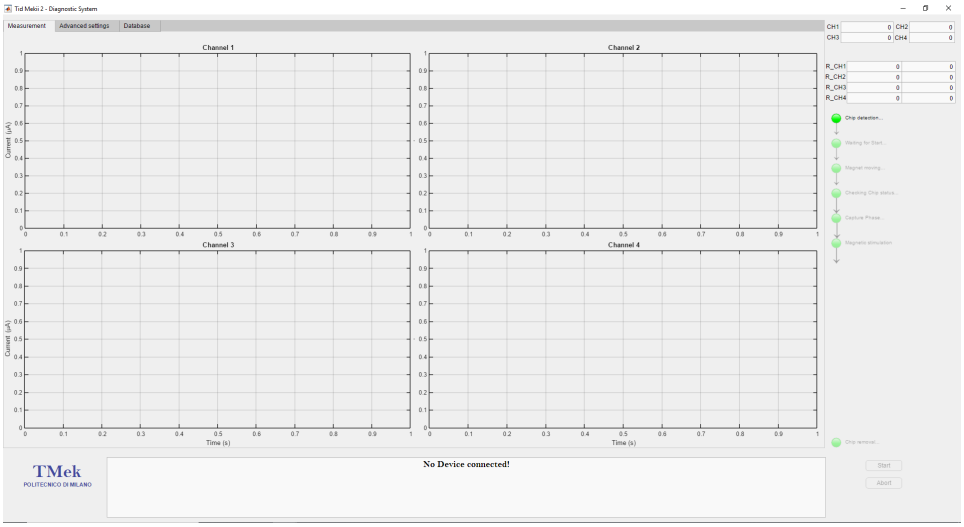

FIGURE 42. *Graphic interface of the device. It is created using MATLAB App Designer and allows the communication of a PC with the setup.*

III.8.1. Graphical interface. The initial graphic interface of TMek device is reported in Fig.42. This has been the first activity I have been involved in at the beginning of my thesis.
Apart from the four panels dedicated to plot in real-time the differential current (Current (μA) vs Time (s)), other important parameters are visualized; on the upper left part, three different pages can be selected: the *main page*, the *advance settings page*, where several important parameters can be tuned for every particular experiment and the *database* page, where, in a summary table, all the principal data of the trials are stored. On the main page, moreover, always with respect to a single sensitive area (i.e. N-th channel), two main information, both on the top-right of Fig.42, must be focused: (i) the upper "CH" "N" indicates the goodness of the resistance matching, and represents the magnitude of the voltage applied to the smaller resistance between R_M and R_R, (ii) lower cells "R_CH" "N", instead, reports the resistances of the two regions, "M" on the left and "R" on the right, and these are always around 150Ω.

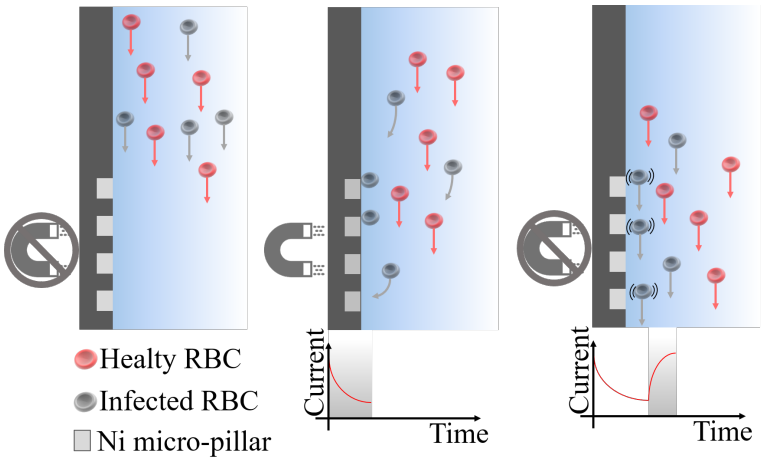

FIGURE 43. *A qualitative picture of the dynamics of infected RBCs and healthy RBCs when the magnets are moved, from and to the Ni concentrators. Below is drawn the qualitative exponential behaviour of the signal.*

III.8.2. MATLAB analysis. When the experiment is launched, assuming a vertical configuration, something like what is sketched in Fig.43 happens. The NdFeB permanent magnets, starting away from the chip, approach the rear of the chip, such that they saturate the embedded Ni pillars. The combined action of the macroscopic and localized gradient causes the attraction of paramagnetic particles, if present, on measurement electrodes. On the other hand, corpuscles with magnetic susceptibility very close to that of the medium, sediment below and do not contribute to a current change. The current signal, which is on the order of the μA, decreases when NdFeB magnets are near the chip, while it increases when the magnet are disengaged (see Fig.43). The reason why explaining the descending slope during the capture, can be found looking at Fig.40. The electronics plots the difference $I_M - I_R$: assuming I_R does not fluctuate, or at least assuming the common mode fluctuations are subtracted, if corpuscles are attracted onto the electrodes I_M decreases, and subsequently $I_M - I_R$ as well. Thus, the plotted signal current is descending during attraction phase, whereas a positive exponential jump in the dynamics is associated to the removal of the magnets.
The agreement between experiments and simulations performed using *COMSOL* (see Fig.44) fully supports the consistency of our interpretation of the physical mechanism governing TMek test. The exponential behaviour of the signal after magnet removal represents a saturation phenomena when all captured corpuscles are released the signal ideally jumps back to the initial value, in absence of a sizable drift.

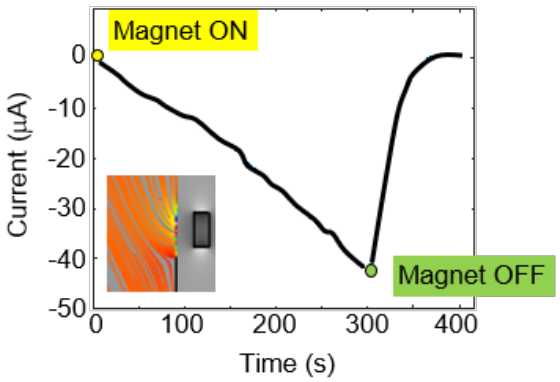

FIGURE 44. *COMSOL simulation current signal amplitude vs. time; within the inset, a zoom of the trajectories in proximity of a concentrator. By courtesy of M. Giacometti and F. Milesi.*

Depending on the protocol of measurement used for the specific test, many cycles of magnets engagement-disengagement can be carried out; even though just one cycle is sufficient to study the sample, usually, two cycles are performed to improve the reliability of the test result and better disentangle the true signal from spurious fluctuations.
In Fig.45A a typical TMek signal of an infected blood sample is presented: as it is possible to see, here two cycles are performed and, accordingly with the multiphysics simulation of Fig.44, even if this is just for one capture, exponential behaviour characterizes the experiment. During an experiment, the most important parameters to be calculated are the amplitudes, A_1 and A_2, and the time constants τ, which can be related to the capture τ_c or the release τ_r of the particles. As explained in section II.4, the amplitude of the net signal variation (i.e. A) is correlated to the corpuscle concentration, the higher the number of attracted particles, the higher the resistance variation, so, the bigger the current signal; in particular, to introduce a technique as rigorous and reproducible as possible, for the measurement and the analysis that will be exposed by now, only the amplitude A_1 will be used. The signal dynamics, expressed by time constants τ_i, instead, reflects the morphology and the magnetic susceptibility that could be useful for a further analysis of the sample, in order to understand, for example, the stage of the parasite cycle. On the other hand, in Fig.45B is represented the typical signal shape of an healthy patient: in this case no exponential dynamics is detectable within the signal.

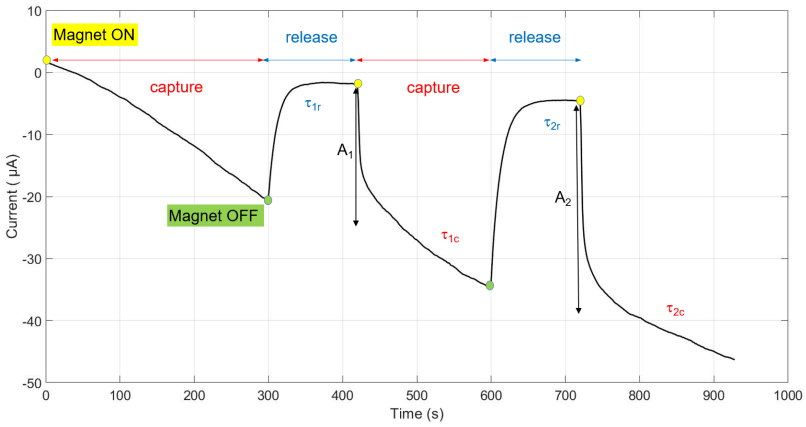

(A)

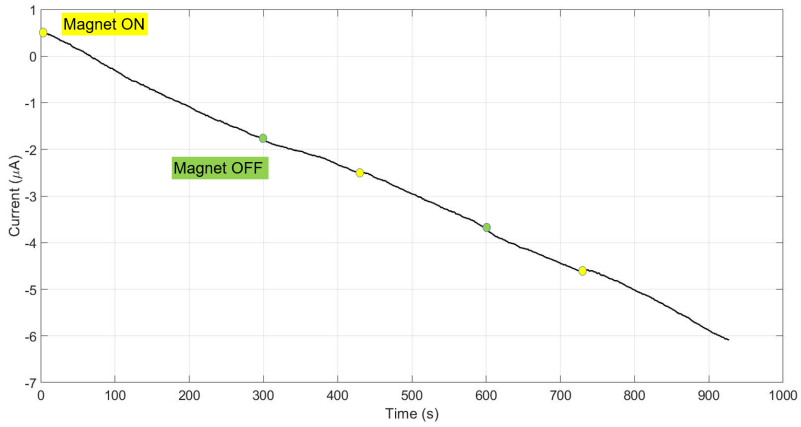

(B)

FIGURE 45. *The two figures represent the typical shapes of diseased (A) and healthy (B) patients. It's evident the different dynamics of the signals related to a capture, in the first case, and just spurious drift, in the second.*

Given the final net signal, several possible types of analysis to extract A_n and τ_i have been tried to tackle the difficult situation corresponding to signals from samples with low parasitemia, there the estimate of the amplitude can be highly affected by fluctuations. MATLAB code was written in order to deal with the most generic and drift-disturbed signal possible, keeping into account the spurious drift that affects the, ideally, exponential dynamics of the net signal. For this reason, after several tries, it was chosen the following type of signal analysis.
Before the real signal analysis, a first screening is performed to determine whether the measurement can be considered valid or not. In particular a measurement is not valid if:

- the baseline has a change of slope between $t_1 = 250$ seconds and $t_2 = 420$ seconds
- in case of small signals, presence of spurious fluctuations bigger than the white signal in correspondence to the amplitude $A_{1,white}$
- in case of small signals, after the movement of the magnets, jumps with opposite amplitude, with respect to the expected one, and with value bigger than $A_{1,white}$
- fluctuations or steps within A_1 with amplitude bigger than $2\mu A$
- variation of the slope of the baseline between before the engage of the magnet and the disengage bigger than a factor equals 5
- baseline with upwards concavity which impedes the estimation of small signals

Then, there is a further filtering of the valid signal itself which consists in selecting the sensitive area (i.e. what channel looking at), and it is usually the one with the highest goodness of resistance matching, since it is usually the most reliable. After this screening, the signal is analysed: by subtracting a linear background and evaluating the amplitude as reported in Fig.46.

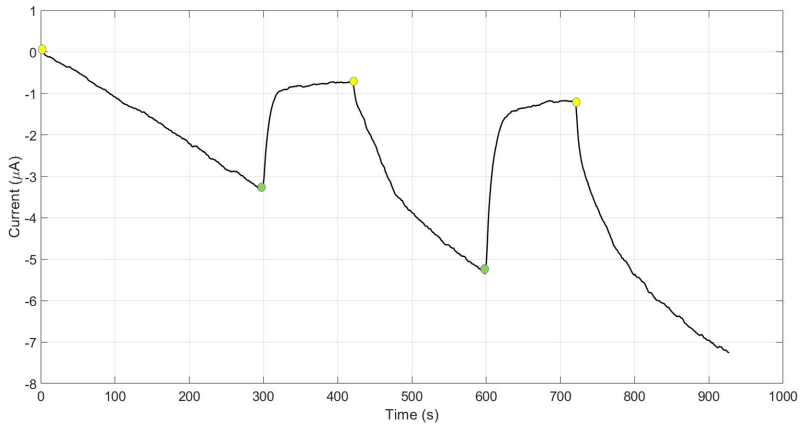

(A)

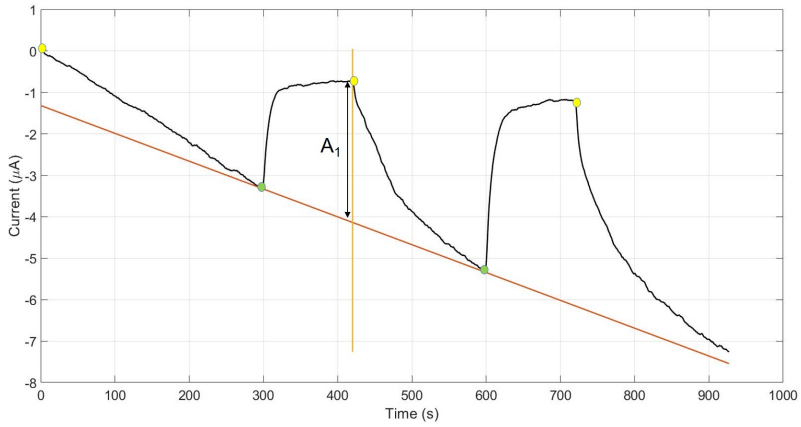

(B)

FIGURE 46. *The two figures represent the analysis signal technique chosen. (A) represents the raw signal of a diseased patient; (B) shows the subtraction and evaluation of the amplitude within the first cycle.*

After background subtraction an exponential fit is performed to evaluate a characteristic time constant tau; the amplitude is derived by the difference between the top-point at which the second capture starts (i.e. yellow spot) and the ordinate value at the same x-axis. To evaluate the overall error due to this chosen method of analysis, the following approach has been chosen: the variance of the raw signal is calculated in the 40 seconds before the first "MAGNET OFF", and the same is done on the top of the exponential, so the 40 seconds before the second "MAGNET ON". These two variances are summed quadratically to get the error A_{err} associated to the estimation of the amplitude of the signal. Talking about the time constants, on the other hand, their associated errors are the ones returned by the fitting app of MATLAB itself.

The calculated values associated to the raw signal are saved, together with the workspace, MATLAB figures and others parameters, within an all-comprehending database, made with *Microsoft Excel*.

CHAPTER IV

Experimental results

This chapter is focused on the experimental results obtained during the Master's thesis work. The variety of the experiments is wide and these have been performed with different goals and perspectives. Notice that during the thesis, both the old chip layout (*separated* measurement and reference regions), and the new chip layout (*interpenetrated* measurement and reference regions) have been used. Before introducing any experiment, let's discuss how samples are treated and tested.

IV.1. Protocol

IV.1.1. Samples preparation. Within all trials done, two main kinds of blood sample have been used:

- *Patient blood samples*: obtained from whole human blood sample diluted with PBS and heparin; the latter is used to avoid coagulation of the cells. These samples have been used for the preclinical validation. From previous optimization works, it was found that an hematocrit (Hct) of 4% favors magnetophoretic capture [51]; therefore, since $8\mu l$ of whole blood sample from patients are taken, they are diluted in $72\mu l$ of heparin-PBS solution.
- *Synthetic models of infected blood, made by spiking treated RBCs in whole blood samples diluted with PBS and heparin*: the treatment with $NaNO_2$ induces a full transformation of hemoglobin into methemoglobin (t-RBCs) which mimics the magnetic behaviour of i-RBCs. As seen in section II.2, methemoglobin is an oxidized form of hemoglobin, in which iron is in ferric state (i.e. Fe^{3+}) and not ferrous such as normal hemoglobin (i.e. Fe^{2+}) [107]. This transformation is the same leading to hemozoin formation from hemoglobin: this means that also methemoglobin exhibits paramagnetic behaviour. Sodium nitrite ($NaNO_2$) solution is used to convert a diamagnetic suspension of diamagnetic healthy erythrocytes into paramagnetic t-RBCs [108]. Referring to section II.3, the net magnetic susceptibility of t-RBCs, with respect to water medium, is $3.9 \cdot 10^{-6}$, slightly bigger than other infected cells: in fact, $\Delta\chi_{metHb}$, is twice that of i-RBCs in schizont stage ($1.8 \cdot 10^{-6}$), which, among the i-RBCs stages, has the highest value. Therefore, t-RBCs can be used to create blood samples mimicking malaria infected ones.
  After treatment, t-RBCs are suspended in a PBS solution with 4% hematocrit. This will act as "mother" for the t-RBCs in the different sample preparations of the experiments: (i) to prepare suspensions of t-RBCs in PBS with different concentrations just for laboratory tests or (ii) create synthetic models of malaria infected human blood samples by spiking

t-RBC at well known concentrations into whole blood diluted 1:10 in PBS+heparin, to simulate the targeted value of parasitemia $\boldsymbol{P}$.

IV.1.2. Measurement procedure. Once the blood has been properly treated, about $70\mu l$ of the resulting solution are placed on a glass slide with a PDMS rectangular gasket, which is pre-charged on a cartridge, defining, in this way, the bottom well of the magnetophoretic cell. When the operator closes the cartridge lid, the microchip is put in contact with the spring-connectors and the PDMS gasket: thus, is established an electrical connection and, above all, the cell sealing is created, such that a static situation is achieved. The cartridge is inserted into the reader (see section III.7), whereby the chip is connected to the electronics to perform impedimetric measurements and to transmit the data to the PC. Finally, using a stepper motor, the permanent magnets are moved in proximity to the chip at a distance between 25 and $50\mu m$ from its rear face; now the measurement starts. The most general protocol is the one qualitatively represented in Fig.45A and schematically reported here. First capture of corpuscles typically lasts 300 seconds, after which starts the cyclic movement of the magnets, taken far away and then repositioned close to the microchip. The cycles, whose duration is constant within a single trial, are characterized by two parameters: time of release, usually 120 seconds, and time of capture, usually 180 seconds.
As anticipated in section II.3, given that in the horizontal configuration the minimum gradient of magnetic field needed to attract particles towards the chip, is not supplied by the magnets, to analyse the samples where RBCs are the targeted particles, it is always used the vertical configuration in which the surface of the chip is perpendicular to the support surface. In Fig.47, an example of what explained is reported: here the same sample has been analysed with both horizontal (top) and vertical (bottom) configuration, giving just a correct positive diagnosis in the latter case.

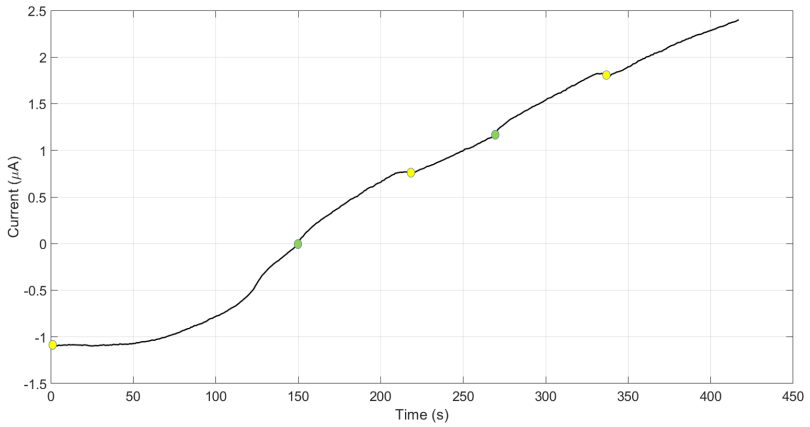

(A)

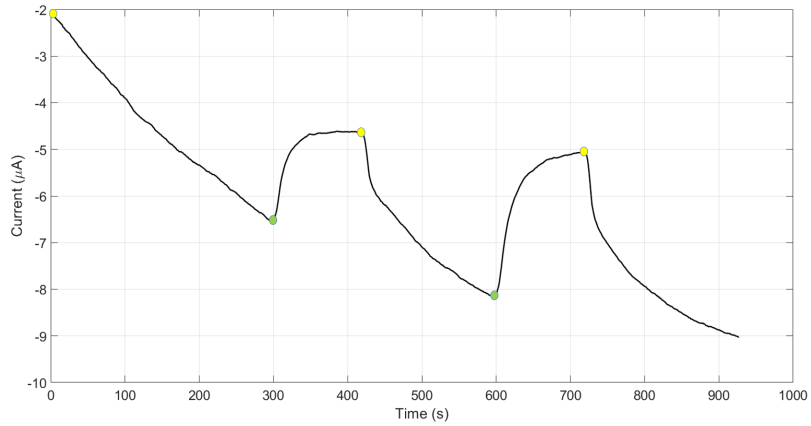

(B)

FIGURE 47. *Comparison of outcome signals for i-RBCs in horizontal (top) and vertical (bottom) configuration. Given the same sample, only the vertical configuration leads to a correct positive diagnosis.*

Before any set of quantitative trials with human blood, a calibration of the device it is necessary to evaluate the so-called "white" signal of the day. This measurement is done using a solution made only by PBS, i.e. without paramagnetic corpuscles, and it is useful (i) to estimate the signal amplitude due to mechanic jumps or electromagnetic interference in correspondence of stepper motor movement and (ii) to evaluate the spurious drift signal. The "white" signal is then processed by the software of data analysis and the amplitudes of jumps due to the motor movement will be then subtracted to the ones from the signals related to potentially infected human blood.

After the measurement the chip and the gasket are cleaned and sterilized by subsequent washing with a *SDS* (i.e. sodium dodecyl sulfate) solution, water-ethanol solution and deionized water, to be reused for the following tests.

IV.2. Limit of detection

The differential current I(t) measured by the TIA is proportional to the impedance variation, in particular $\Delta R/R_0$ which, in turn, is proportional to the volumetric fraction Φ (see section II.4). With the electronic systems employed, the minimum measurable $\Delta R/R_0$ has been estimated around 0.01% [50].
This threshold, together with "fluid-related problems" thermal fluctuations, noise sources associated to the chip (i.e. stray currents), fluctuations due to non-perfect mechanical fabrication of the cartridge or the gasket and the movement of the motor, lead to a resultant minimum number of $10 parasites \cdot \mu l^{-1}$ (see later), which is the aimed limit of detection (LoD) of TMek.
"Fluid-related problems" concern undesired motion of the fluid within the cell due to non perfect sealing. Changes of temperature can also induce spurious fluctuations: indeed, a few tens of millidegrees produce a $\Delta R/R_0$ variation around 0.015% [109]. Moreover, since the electrolytic solution has its own resistance, there is an associated Johnson-Nyquist noise (i.e. thermal noise), whose power spectral density (PSD) can be evaluated:

$$S_i(f) = \frac{4k_BT}{R_0} = 9 \cdot 10^{-23} A^2/Hz \tag{IV.1}$$

where k_B is the Boltzmann constant ($1.38 \cdot 10^{-23} J/K$), T the temperature expressed in Kelvin ($300K$) and R_0 the resistance equal to 150Ω. Considering that the pole of the LPF of the lock-in amplifier is at 100Hz, a root mean square (rms) value of the noise current at the input of the transimpedance amplifier of about 0.1nA is found. Nonetheless, since TMek measure is done in liquid, the thermal noise term is dominated by the aforementioned fluctuations related to the fluid and the temperature variations. Having said this, within the device other kinds of noise can be considered.
Another source of noise is due to the unavoidable parasitic capacitance which always affects an electronics system, related to the length and proximity of wires, pads and tracks.
There is then noise associated to stray current paths between gold tracks. Indeed, even though on the chip is deposited an SU8 passivation layer over all connecting tracks, but the sensitive areas, the photoresist still acts as a dielectric, such that a stray capacitance between gold tracks arises. Total current entering the TIA is given not just by the signal related to the sensitive areas, but also by current related to the gold tracks: $I_{total} = I_{signal} + I_{stray}$. Since the significant readout signal is proportional to the percentage change in current $\Delta I/I_{total}$, the number at the denominator must be reduced, and this can be done reducing the parasitic current. Furthermore, reducing I_{stray} is also beneficial in terms of total noise reduction. This parasitic current can be reduced increasing the impedance related to the tracks, on which, in fact, SU8 is put. If SU8 were not used, assuming $R_{signal} = 21K\Omega$ and $R_{stray} = 16.5K\Omega$, there would have been a quasi-equal partition between the two paths; on the other hand, with a $5\mu m$ thick SU8 layer, the impedance, assuming $\varepsilon_r = 30$ [110], at 1MHz becomes on the order of $10^5 - 10^6\Omega$ such that the contribution of stray current along the tracks can be lowered by a factor of 10 (up

to 100).
At the same time, another parasitic capacitance arises between the gold tracks and the substrate through the SiO_2 dielectric layer which separates the electrodes from the Ni concentrators. The elevated conductivity of the highly-doped substrate allows to close, through two capacitors in series (i.e. electrode-SiO_2-substrate and substrate-SiO_2-electrode), the path in parallel to the sensing area (see Fig.48). To reduce this effect, and consequently improve SNR, a 200nm gold layer is sputtered on the back of the chip to ground it: doing that, is created a short circuit for the current through the SiO_2 which does not enter the TIA virtual ground.

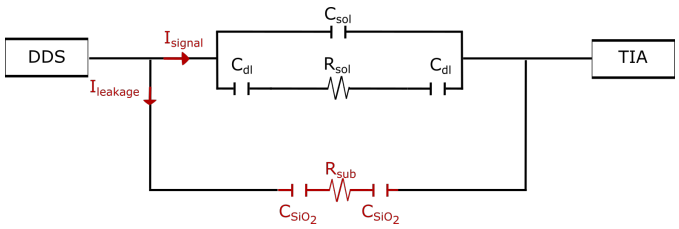

FIGURE 48. *Schematic of sensing unit and the stray capacitance due to the substrate: in black is represented the electric path of the current related to the actual signal, whereas in red the path associated to the current of leakage. The latter path is grounded with 200nm of sputtered gold, such that* $I_{leakage}$ *is reduced at most.*

The total value of noise current, which in any case is mainly due to variations of temperature, can be measured putting just a PBS sample in the cell and measuring the output signal of the chip. Evaluating the peak-to-peak signal amplitude after subtraction of a linear background in an isolated trial, led to a minimum value around 20nA such that the standard deviation σ can be roughly estimated by dividing by 6, thus obtaining 3.5nA: this means that, ideally suppressing any other possible source of noise and fluctuation, the minimum detectable signal would be 4nA.
Finally, there are other spurious terms such as fabrication of PDMS gasket and cartridge, that have to be optimized as well if one wants to reduce external sources of undesired signals and, especially, *spurious drift signal*. Indeed, drift signal intrinsically affects, not only the resolution of the system, but also the reliability of the automatic analysis of the differential currents. Since the behaviour of this spurious drift signal constitutes one of the main obstacles to improve the LoD and reliability of the diagnostic system, many different experiments focused on its reduction have been carried out, together with the design and realization of a new chip layout (see section IV.7.2).

IV.3. TMek calibration curves

This section deals with two important experiments which delineate two of the main features of TMek: LoD and quantification of malaria parasites. These experiments were done at "Luigi Sacco" hospital in Milan. t-RBCs blood samples, prepared as described in section IV.1, and the old chip layout with reference and

measurement regions separated were used.

IV.3.1. Calibration curve. In the former experiment, it was used an initial attraction time of 300 seconds, during which the permanent magnets are in proximity of the rear of the chip; then the default protocol was exploited (see section IV.1.2), with $t_{capture} = 180$ seconds and $t_{release} = 120$ seconds. Fig.49 shows the signals amplitudes A_1 due to t-RBCs capture, as a function of their concentration. The different concentrations of t-RBCs$\cdot\mu l^{-1}$, mimicking the behaviour of mature RBCs infected by *Plasmodium*, were obtained by spiking whole-blood samples from a healthy donor, previously diluted in PBS to a 4% hematocrit, with well-known amounts of t-RBCs. After the evaluation of the "white" signal A_{white}, this was subtracted to every A_1 associated with the corresponding parasitemia level. In Fig.49, the linear fit in the log-log plot highlights a linear behaviour over more than two decades, from 10^2 to about $5 \cdot 10^4$t-RBCs$\cdot\mu l^{-1}$ (which equals to a parasitemia between 0.002% and 1%), followed by a change of slope at higher concentrations.

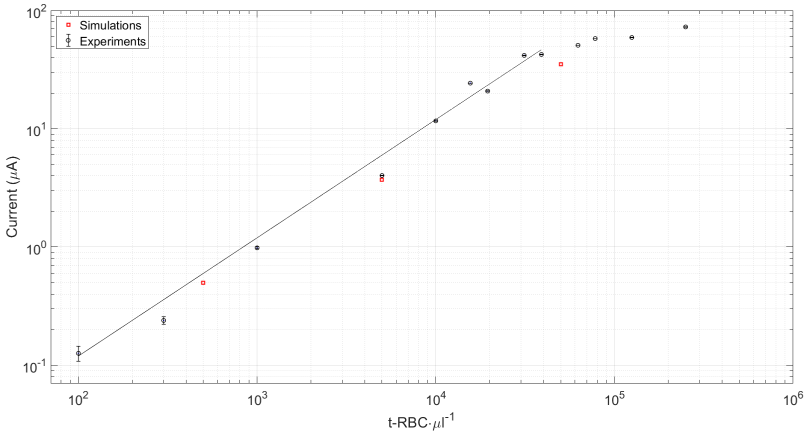

FIGURE 49. *Calibration curve on blood samples from healthy blood donors with known concentration of t-RBCs mimicking the behaviour of RBCs infected by Plasmodium. In the log-log plot, in red are reported the simulations by COMSOL (courtesy of M. Giacometti and F. Milesi), while in black the experimental points, with a linear fitting in the range* 10^2 *to* $5 \cdot 10^4$*t-RBCs*$\cdot\mu l^{-1}$.

The initial linear behaviour, with a sensitivity $S \simeq 1nA\cdot(\text{t-RBC}/\mu l)^{-1}$, fully reflects the expected proportionality obtained by *COMSOL* simulations: in the graph are superimposed, with red spots, three simulation points done for t-RBCs$\cdot\mu l^{-1}$ (parasitemia) equal to 500(0.01%), 5000(0.1%) and 50000(1%), to which were associated amplitudes A_1, respectively, of $0.5\mu A$, $3.7\mu A$ and $35\mu A$. In the graph, are reported the error-bars calculated with the method described in section III.8. Apart from a small shift upwards, there is a good agreement between experiments and simulations, whereby it can be confirmed a full understanding of the physical mechanisms underlying the system. It must be remarked, anyway, a possible additional

source of error due to the preparation of the sample: indeed, the nominal concentration reported in Fig.49, and in the following curves as well, might be affected by some level of uncertainty related to the small volumes of liquid involved in sample preparation. This might explain, for example, the signal at $1.5 \cdot 10^4$ t-RBCs$\cdot\mu l^{-1}$ which is out of statistic by about $5\mu A$. The final saturation at high concentrations of t-RBCs, moreover, could be told by the filling of the sensitive areas and also by saturation of the electronic itself. Therefore TMek, dealing with a fully controlled situation of samples by t-RBCs, can provide a quantitative estimation of the parasitemia level over more than three decades.

IV.3.2. Limit of detection curve. To improve the *Limit of Detection* of the device, it was used a different measurement protocol rather than the one described above: the first attraction phase lasted 10 minutes, $t_{capture} = 360$ seconds and $t_{release} = 120$ seconds. The overall time of capture was doubled in order to catch a higher number of paramagnetic corpuscles. Moreover, this modification was also introduced to discriminate more easily the spurious signal jumps from fluctuations and motor movement. The "white" signal used to perform the signal analysis is the same exploited in the above mentioned calibration experiments: this because the chip employed was the same for the two calibration tests. The linear plot in Fig.50 is obtained using the same approach seen before, but working with lower levels of parasitemia: the healthy blood sample has been treated and diluted such that were mimicked four solutions with 10, 20, 40 and 80t-RBCs$\cdot\mu l^{-1}$, respectively $\boldsymbol{P}$ equal to 0.0002%, 0.0004%, 0.0008% and 0.0016%.
Exploiting an initial attraction phase of 600 seconds, increases the sensitivity (over $5nA \cdot (\text{t-RBC}/\mu l)^{-1}$), allowing to achieve a record LoD of 10t-RBCs$\cdot\mu l^{-1}$, or equivalently 10parasites$\cdot\mu l^{-1}$, since one i-RBC is infected by one parasite. The curve presents a certain linearity, more accentuated within the three points on the right, whereas is partially avoided by the point at lowest parasitemia: it is expected when reaching the limit of detection baseline signal, from which is increasingly difficult to discern between the actual differential signal and the fluctuation terms.

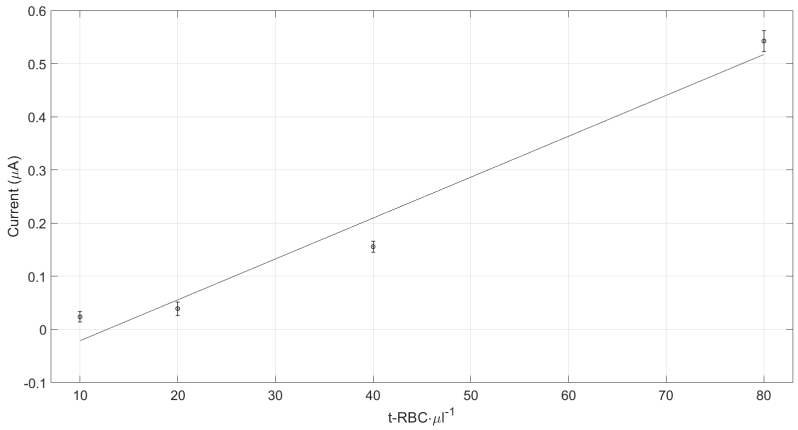

FIGURE 50. *Limit of Detection curve on blood samples from healthy blood donors with known concentration of t-RBCs mimicking the behaviour of RBCs infected by Plasmodium, as Fig.49.* The black line reports the linear fit of the four experimental points.

IV.4. Synthetic hemozoin

In order to characterize the device and its magnetophoretic properties, for a further understanding of hemozoin crystals behaviour, several experiments using synthetic hemozoin crystals have been carried out. As seen in section I.2.1, synthetic hemozoin crystals (β-hematin) show the same magnetic properties of natural HCs. Diluting β-hematin (by "Invivogen") with PBS at various concentrations, a calibration curve made by 4 significant points has been obtained (see Fig.51). The curve was recorded using the chip with the old layout. Moreover, given their high propensity to stick above the gold electrodes, when dealing with synthetic hemozoin an accurate cleaning of the chip between each test is useful, in order to avoid the saturation of the signal. The calibration curve shows a linear behaviour as the concentration of magnetic corpuscles increases. In this case the Limit of Detection is $3\mu g \cdot ml^{-1}$, which corresponds to about 5000parasites$\cdot\mu l^{-1}$, therefore two orders of magnitude higher with respect to the case of direct detection of i-RBC, as expected because the signal is proportional to the volume of attracted particles and HCs are much smaller than RBCs (see section II.2). In the inset of Fig.51 is also reported a picture of HCs accumulated on the electrodes upon magnetophoretic capture.

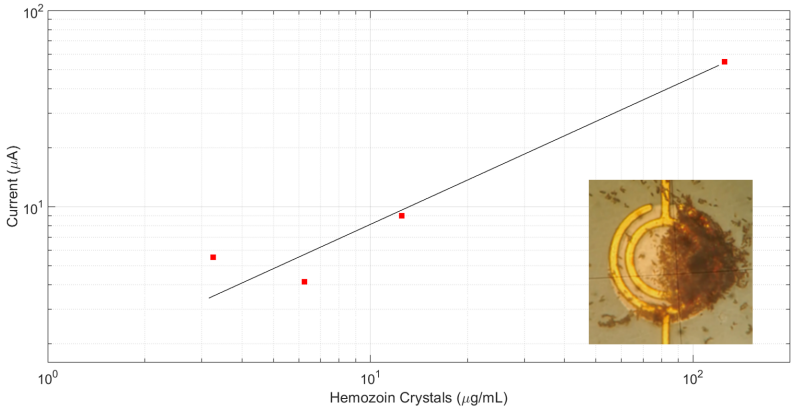

FIGURE 51. *Calibration curve on suspension of β-hematin crystals in PBS. In the inset, the picture of HCs accumulated on the electrodes, [51].*

The calibration curve above was obtained working in vertical configuration; nevertheless, as described in section II.3, because of their high net magnetic susceptibility, this could have been obtained, with the actual device, in the horizontal configuration as well. Fig.52 shows, on the top, the signal of HCs in horizontal configuration, whereas on the bottom the outcome in vertical configuration.

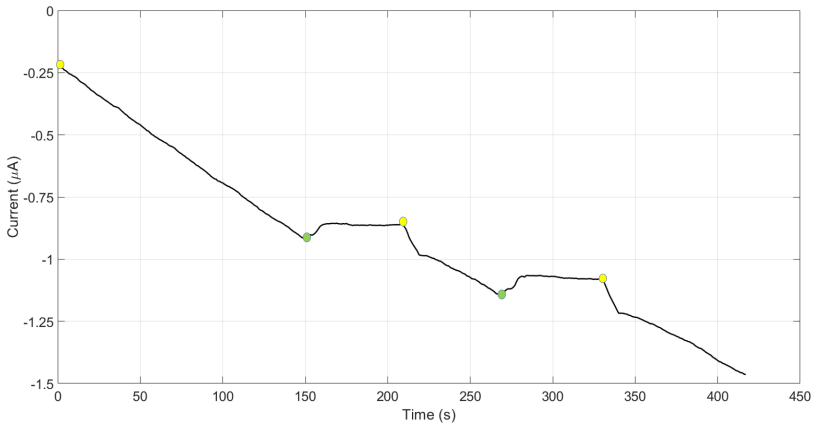

(A)

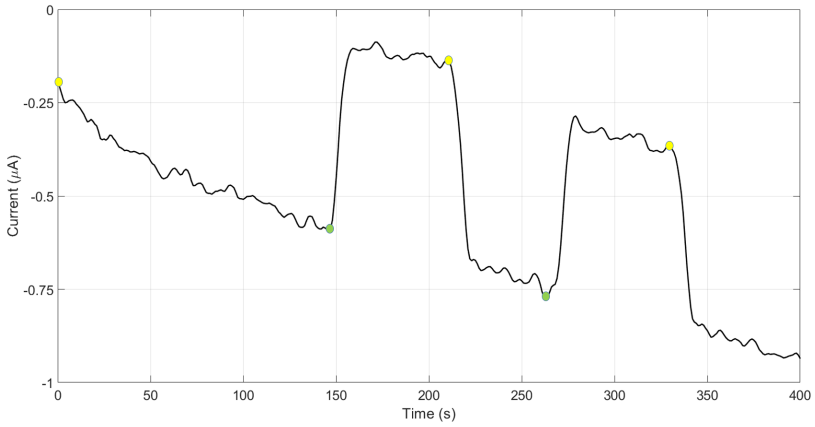

(B)

FIGURE 52. *Comparison of outcome signals for HCs in horizontal (top) and vertical (bottom) configuration. In both cases the signals are showing an evidence of the presence of paramagnetic particles.*

IV.5. Follow up monitoring using TMek

This section exposes a so-called *follow-up* test: in medical field this term indicates a phase of monitoring of a disease to understand its evolution and the eventual efficacy of the treatment adopted. In the case displayed, it has been dealt with a patient affected by *P. vivax*, arrived from India and hospitalized at "Luigi Sacco" hospital. The presence of malaria was initially confirmed by microscopy and PCR, and monitored as well during the illness evolution.
Three TMek tests have been carried out on the patient sample blood: the day of admission and then 24 hours and 48 hours after the beginning of the treatment with chloroquine (see section I.1). Microscopy analysis indicated an initial parasitemia of 1%, with 20% of i-RBCs corresponding to gametocytes, which, thanks to the use

of antimalarial drugs, decreased to 0.1% after 24 hours and was zeroed within the first 48 hours by the recovery.
The three corresponding signals are represented in Fig.53 and were obtained using the standard protocol of TMek and the old chip layout. Moreover, since this is not a synthetic model, the whole blood sample taken was just diluted with PBS and heparin 1:9, as described in section IV.1. In figure below, the three graphs are sorted by timing of treatment, from top to bottom. In red (top Fig.53), is shown a signal with amplitude $A_1 = 1\mu A$, then this value decreases with time: is $0.4\mu A$ after 24 hours (blue) and is negligible for $\boldsymbol{P}$=0% after 48 hours.
These trials highlight the possibility, for TMek, not only to diagnose quickly the eventual presence of malaria parasites, but also its capability of monitor the illness evolution during the treatment.

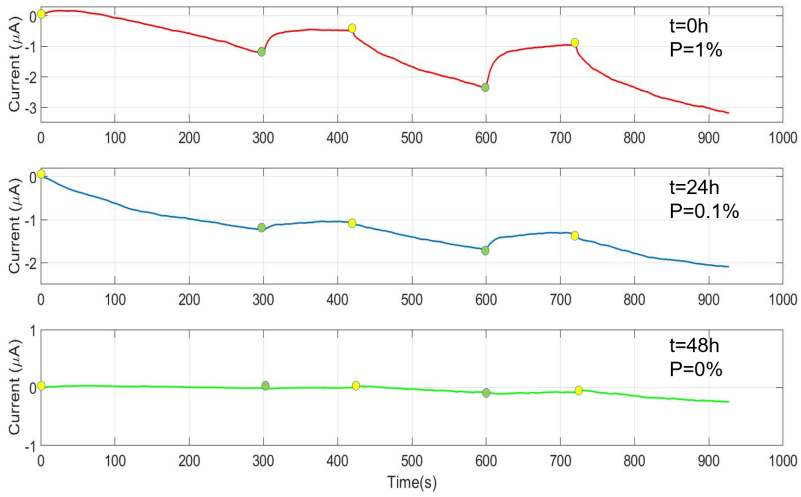

FIGURE 53. *TMek signal vs. time on whole blood sample from a patient affected by P. vivax, at t=0h, 24h and 48h upon treatment with choloroquine. Starting from the top,* $\boldsymbol{P}$*=1%, 0.1% and 0%, and the corresponding amplitudes* A_1*=*$1\mu A$*,* $0.4\mu A$ *and* $0\mu A$*.*

IV.6. Preclinical validation study

In 2019, at the beginning of my Master's thesis, a preclinical validation campaign on 108 patients was carried out in Cameroon. I participated to the preparation of the expedition and the data analysis. During it, two TMek systems have been installed in the diagnostic laboratory of Hôpital Saint Luc of Mbalmayo, where all the analysis have been made. Despite this, blood samples have been taken by three different hospitals: Hôpital Saint Luc of Mbalmayo, Central Hospital of Yaoundé and Hospital CASS of Yaoundé. Only patients with suspects of malaria after a first medical consultation were considered in this study. For each patient taken into account, was collected a file reporting the essential clinical information, as well as the results of the following tests: complete blood count, thick blood smear microscopy with parasitemia quantification evaluated by local staff and RDTs *SD BIOLINE*

MALARIA Ag P.F/PAN by "ABBOT" [111]. In order to lead the experiments, a peripheral venous blood sample was taken from each person, using standard test-tubes with EDTA anticoagulant, while only in the last days, it was employed also a prick-test version on a limited number of patients, in which a capillary sample of $8\mu l$ is taken and immediately diluted with PBS and heparin, such that is ready for TMek analysis. In order to have a clinical picture as complete as possible, all slides with blood smears analysed were collected and brought back to Italy for a further independent evaluation of *Plasmodium* species and parasitemia, by three microbiologists of "Luigi Sacco" hospital.
Throughout the campaign, the majority of the experiments have been carried out using the standard protocol with 5 initial minutes of attraction and 2 cycles with $t_{capture} = 180$ seconds and $t_{release} = 120$ seconds; nonetheless, out of 116 tests, 45 "rapid", with just 1 cycle of capture-release, were done. Moreover, every day, for each chip, a "white" signal test to estimate the baseline noise, was performed by measuring the signal due to a PBS sample.
To be taken into consideration for an effective analysis and subsequent automatic diagnosis, the blood sample and the related raw signal must satisfy some initial conditions, such that a filter protocol has been stated:

(1) elimination of the blood samples badly conserved or with a time interval between the sampling and the measurement longer than 16 hours, which can induce spurious hemoglobin transformations harmful to the analysis
(2) individuation of invalid tests if at least one the following condition is verified:
   - baseline with a change of slope between $t_1 = 250s$ and $t_2 = 420s$
   - in case of small signals, presence of spurious fluctuations bigger than the white signal in correspondence to the amplitude $A_{1,white}$
   - in case of small signals, after the movement of the magnets, jumps with opposite amplitude, with respect to the expected one, and with value bigger than $A_{1,white}$
   - in case of large signals, fluctuations or steps, within A_1 of the signal, bigger than $2\mu A$
   - variation of the slope of the baseline between before the engage of the magnet and the disengage bigger than a factor equals 5
   - baseline with upwards concavity which prevents estimation of small signals by subtraction of linear background

After having passed through this first skimming, the signals have been processed using the software of analysis described in section III.8, obtaining, for each patient, the evaluation of the amplitudes A_n, the time constants τ_i and the respective errors: among these, however, the most relevant were the amplitude A_1 and its error A_{1,err_signal}. TMek analysis have been done using four different chips, all with the old layout: these have been calibrated before the departure, such that a tooling factor could be used to normalize their amplitudes. Moreover, within each chip, for different sensing areas, another tooling factor was needed to normalize the resultant amplitude. The implemented automatic diagnosis assigns a *positive* in case of:

$$(A_{1,signal} - A_{1,white}) > \sigma \tag{IV.2}$$

in which σ is defined as:

$$\sigma = \sqrt{A^2_{1,err\_signal} + A^2_{1,white}} \tag{IV.3}$$

where we assume that the error of the white signal is on the order of the white signal itself, as resulting from the variability of the white signal in different measurements. Data of each patient have been collected within a database: inside this, apart from the parameters of the signals, are also reported the clinical data (e.g. Hct, age, sex, treatment etc.), the experimental main features (e.g. time of sampling, time of measure, setup, chip, channel "CH" analysed etc.), the diagnosis performed in Cameroon and the ones performed in Italy.
As reference for the statistical analysis, has been used the final classification of "true" malaria cases carried out by Infectious Diseases specialists of "Luigi Sacco" hospital on the basis of: (i) three independent evaluations of the parasitemia via microscopy, (ii) the complete blood count, (iii) the database file with clinical relevant information on the patient filled by Cameroonian doctors.

IV.6.1. Results. Having both TMek and reference statements, is possible to define a *contingency table*, in which, "true" and "false", correspond to the *reference* statements of the doctors, while, "positive" and "negative" refer to TMek results. Using this kind of classification, several important statistical measures will be obtained (some of them already cited in section I.3):

- Sensitivity or True Positive (TP) rate: capability to correctly identify a diseased patient
- Specificity or True Negative (TN) rate: capability to correctly identify an healthy patient
- False Positive (FP) rate: occurs when the patient tests positive, but does not actually have the disease
- False Negative (FN) rate: occurs when the person tests negative, but does actually have the disease
- Positive predictive value (PPV): is the probability that patient with a positive diagnostic test truly has the disease
- Negative predictive value (NPV): is the probability that patient with a negative diagnostic test truly does not have the disease

Using the RDT BIOLINE in parallel provides a benchmark, which allows to evaluate the potential and the limits of the TMek test device at the state-of-art. The key performance indicators (KPI) are reported in the table below.

Result	TMek	RDT
True positive (n)	46	45
False positive (n)	10	5
False negative (n)	0	1
True negative (n)	19	24
Sensitivity (% [95% CI])	100 (90.3-100)	97.8 (87-99.8)
Specificity (% [95% CI])	65.5 (45.5-81.4)	82.7 (63.5-93.4)
Positive predictive value (% [95% CI])	82.1 (69.1-90)	90 (77.4-96.2)
Negative predictive value (% [95% CI])	100 (79-100)	96 (77.6-99.7)

TABLE IV.1. *Comparative performances of TMek and lateral-flow RDT, from the prevalidation campaign in Cameroon. For the four bottom values is indicated also the interval of confidence at 95%.*

Following the data analysis procedure exposed before, 33 samples were discarded (15 due to bad or prolonged sample conservation and 18 due to signal anomalies impeding a reliable assessment. The last correspond to invalid tests, which should have been ideally repeated by fixing problems giving fluctuations, anomalous drift, saturation. etc.). This represents an important issue to be taken into account, given that, on the contrary, the RDT tested in parallel does not present invalid tests. Nevertheless, this represents just the first preclinical trial of TMek, so that a sizable number of invalid tests connected to the non-optimal engineering of the setups is expected; in Table IV.1, the KPI numbers are obtained just referring to the 75 venous samples analysed both with TMek and the BIOLINE RDT. The sensitivity of TMek is high with a value of 100% (with interval of confidence at 95%: 90.3%-100%) which is given by the absence of false negatives: this means that the device did not miss any diseased patient, and this is important, since implies that every person affected by malaria has been diagnosed truly and therefore treated with antimalarial drugs. The table, however, indicates the presence of false positives (10) which lead the specificity to 65% (45.5%-81.4%): in any case, this does not present such a vital issue as the presence of false negative. Diagnosing someone positive when he is actually healthy, presupposes an additional treatment when not necessary, but there is no risk for the patient life. Even though a detailed analysis of the origin of false positive results has not been done, some of the FP cases could be due to the degradation of hemoglobin which can transform, partially, into paramagnetic methemoglobin, whose magnetic susceptibility is similar to that of i-RBCs. Moreover, some of the false positive cases, could be due to thalassemic patients [112]: this fact requires a further analysis on sets of patients with peculiar RBC anomalies, but this is definitely beyond the scope of this thesis.
Finally, during the last days of the preclinical validation trial in Cameroon, in parallel with the above cited venous experiments, other (10) trials on samples from finger prick have been done. These experiments display a sensitivity equal to 100% and the specificity as well equal to 100%. Even tough the confidence intervals are very large, this preliminary study indicates that the KPI of the test could improve in case of a synchronous sampling and analysis.
Fig.54 depicts the capability of TMek to quantify the level of parasitemia on-field.

The log-log plot presents on the y-axis the normalized amplitudes of the signal acquired at Hôpital Saint Luc of Mbalmayo (i.e. the samples judged as more reliable, because they have been taken in the same hospital where the TMek apparati were installed), whereas on the x-axis is reported the mean number of parasites estimated by three independent microscopy studies. For what concerns the two error-bars: the ones parallel to y-axis represent the σ value calculated with equation IV.3, intended as an estimation of the uncertainty of the software analysis, while the ones parallel to x-axis expresses the semi-difference between the maximum and the minimum value of the parasitemia levels indicated by the microscopists. Evaluating the *linear correlation coefficient* between TMek signal and the number of parasites$\cdot\mu l^{-1}$, it results $R = 0.51$: this indicates the presence of an actual moderate linear correlation between the two physical quantities. Among the whole population, four out-of-statistic samples can be isolated (red points): all these anomalous data correspond to samples where the microscopy analysis evidenced the presence of either a lot of free HCs or gametocytes. Their high magnetic susceptibilities, and subsequent capture efficiencies (see II.1), could explain the anomalous value of amplitude at low level of parasitemia. Therefore, available data still do not show a clear linear behavior, mainly due to the large uncertainty in parasitemia estimation and in the signal amplitude evaluation which is associated to spurious background fluctuations seen on the field, which are not taken into account in the error bar evaluation; nevertheless these data are promising for future developments.

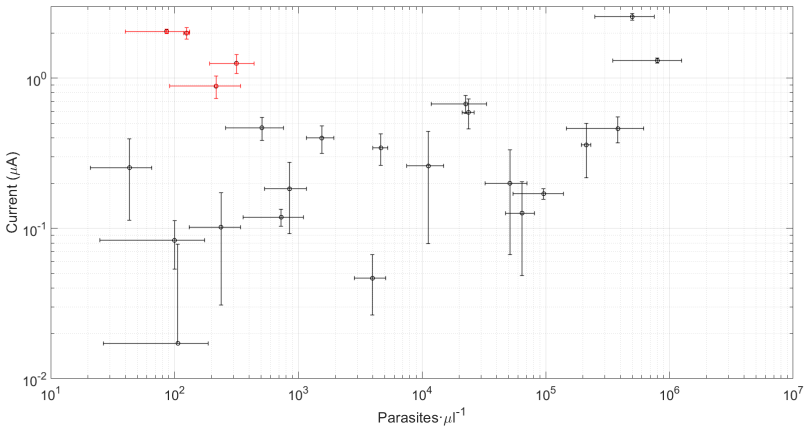

FIGURE 54. *TMek signal vs number of parasites$\cdot\mu l^{-1}$ estimated via microscopy. In red the out-of-statistic samples associated to the presence of free HCs or gametocytes.*

IV.7. New chip layout

IV.7.1. Calibration curve. In order to reduce the spurious signal drift and better subtract the common mode signal, the new chip layout with interpenetrated measurement and reference regions was designed. To calibrate the new chip layout performances, three measurements at different concentration of t-RBCs have been done. These trials are compared with the old chip layout. All measurements

were done following the default protocol and using samples with different t-RBC concentrations in healthy RBCs suspensions in PBS with Hct= 4%.

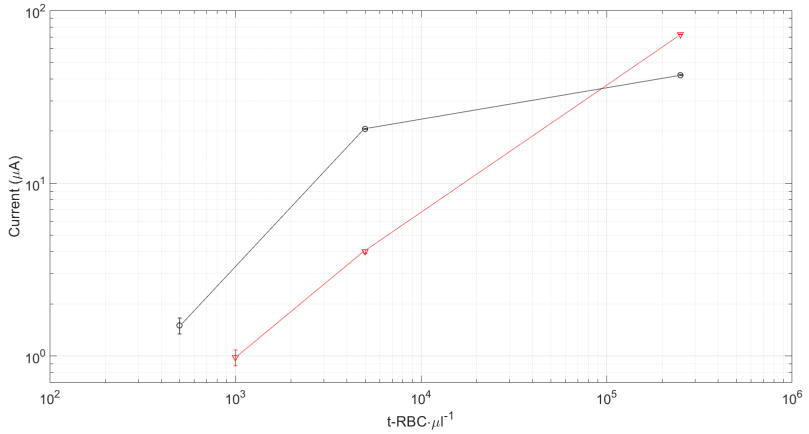

FIGURE 55. *Comparison of performances between new chip layout C2 (black) and old chip layout (red).*

Fig.55 shows the different behaviour between the chips: in black amplitudes A_1 measured with chip *C2* (i.e. interpenetrated regions and more complex design of the electrodes, see Fig.24B,C) while in red the A_1 obtained with the old chip layout (i.e. separated regions with annular shape of the electrodes). With respect to the old configuration, the new one seems to have a less linear behaviour, saturating quicker. Nevertheless, the overall sensitivity of the system does not seem to have been changed, but it is consistent with the previous one.
Although it was not possible to characterize also chip *C1* (interpenetrated regions with annular shape) with different t-RBC concentrations, a first experiment at high level of parasitemia (5%) has been done evaluating, in parallel, the outcome of chips *C1*, *C2*. It came out that the signal amplitudes were similar: $35\mu A$ and $42\mu A$ respectively. Apart from a possible different manufacturing variance the efficiency is on the same order, attesting a similar behaviour, at least at high concentrations, for the two layouts.

IV.7.2. Drift signal. The new chip layout with interpenetrated measurement and reference regions was thought to overcome the problem of spurious drift signal which constantly affects TMek signals. This signal manifests as a baseline over the actual net signal, given by the difference between I_M and I_R: if it were absent, the signal would have a baseline flat in case of absence of paramagnetic particles. Nevertheless this signal is always present and, in addition, with the old chip layout was not repeatable in terms of amplitude and dynamics: indeed, the fundamental issue, relies in the fact that it was not something that could be controlled in advance, but, on the contrary, within each trial presents a specific shape. This problem, as anticipated in section IV.2 strongly reflects, not only on the reliability of the system, but also on the limit of detection. Fig.56 represents two examples of signal affected by the spurious drift. In both cases, because of the change of slope within the single

test, the signal analysis can be strongly affected by an incorrect linear background subtraction.

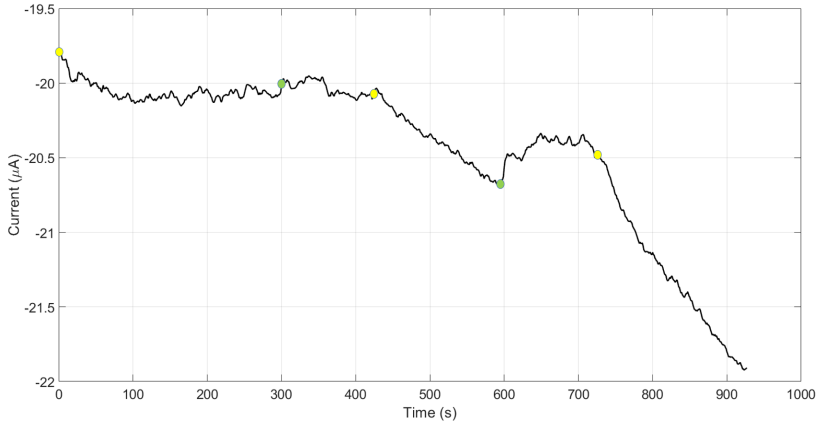

(A)

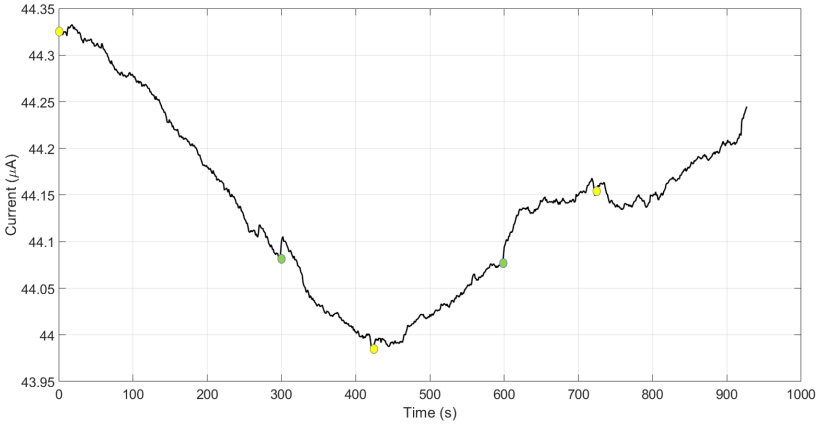

(B)

FIGURE 56. *Two examples of signals affected by spurious drift with the old chip layout.*

The physical causes which might explain it are several: (i) the fluid-related problems which concern movement of the fluid within the chamber and associated variations of temperature, (ii) instabilities of electrical connections through the spring contacts (iii) the PDMS gasket that can have some loss of fluid wetting the pads-spring contacts, (iv) other mechanical fabrication issues related to the cartridge, the reader, the moving motor etc. which could modify the contact impedance or fluid state in the cell.
To minimize these fluctuations a layout allowing for a better subtraction of the common mode fluctuations was chosen. Since at first, the main cause of drift was

associated to the different conditions seen by the separated measurement and reference electrodes, to tackle the problem, it was thought to interpenetrate these two regions. In this way, seeing the same local behaviour of the fluid, the fluctuations of measurement and reference currents should perfectly compensate, such that, in case of just a PBS sample, where no magnetic particle is present, the signal could be flat. Apart from spurious jumps in correspondence of magnet movement, a signal drift is always seen also with the new layout and the expected flat result was not achieved, thus the problem of spurious drift persisted (see Fig.57). Nevertheless, two important results in this direction must be underlined: (i) with respect to the previous layout, the new one presents a smaller absolute value of the drift, indeed out of 34 PBS tests with the new chip, only 3 of them showed a spurious drift signal bigger than 2nA/s, while with the old chip the corresponding percentage was 60% (ii) the new chip guarantees an higher repetition accuracy within each channel of measure; while with the old chip 40% of tests presented a change of the background slope, the rate has been reduced down to 4% in the new chip. These features are highlighted in Fig.57 which shows some characteristic signals measured with the old and new chip. These plots have been obtained exploiting a different protocol of measure because in this case no corpuscle was intended to be captured, therefore a faster acquisition was allowed.

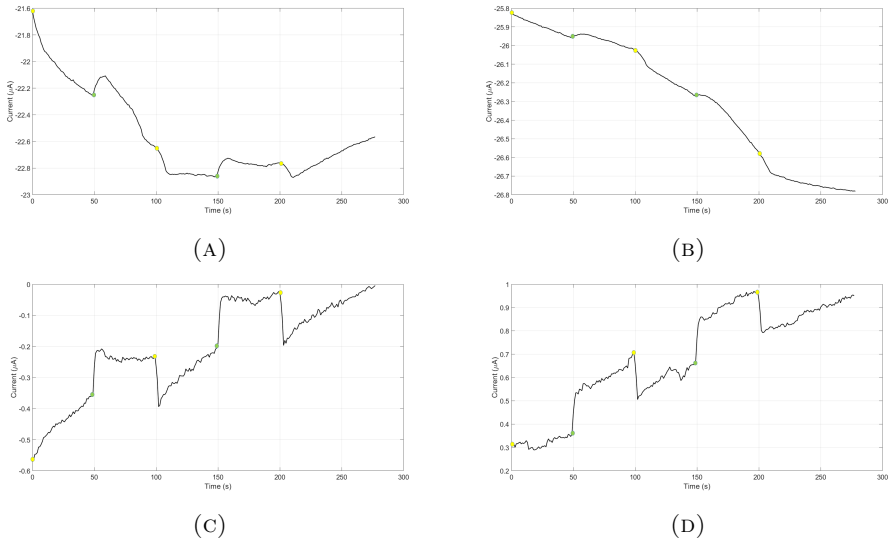

FIGURE 57. *Examples of four signals expressing the different behaviour of the drift with the new chip layout with respect to the old one. In all cases, the sample was just PBS solution. (A) and (B) are the signals taken from the same channel for the chip with old layout. (C) and (D) are the signals taken from the same channel for the chip with new layout.*

Fig.57A and B show typical slope changes obtained with the old chip layout, while Fig.57C and D, measured with the new chip, represent a more reproducible and monotonous drift.

Given that this novelty of interpenetrating two regions of the same sensor did not completely work to solve the problem of spurious drift, other modifications have been tried and others are still under development. One first major modification is represented by the improvement of the Arduino code which is responsible for the initial calibration of the voltages applied to the pads (see section III.6 for physical explanation). To understand whether electronics could be responsible for the drift signal, maybe because of an incorrect and unbalanced supply of voltage, the firmware has been re-written and tested just with physical resistances and not the micro-fluidic chamber. The signal over time (Fig.58) is almost flat, with a slope of about 0.3nA/s, definitely lower than the observed value of 2nA/s in PBS, showing that the electronics itself cannot be addressed as the main cause for spurious drift.

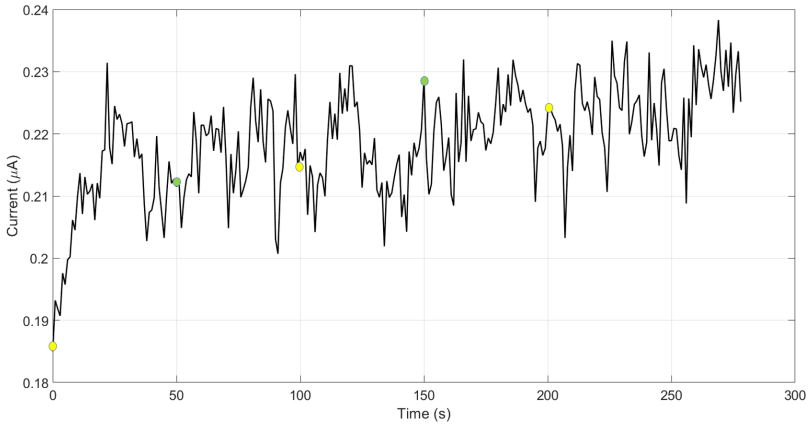

FIGURE 58. *Current signal with only physical resistances to attest the correct compensation of the current and the zeroed spurious drift signal associated to the electronics.*

Among all the remaining possible changes, the main one consists in the design of a new gasket: indeed, it has been noticed that after many tests performed with the same gasket, the chamber, under compression of the chip, starts to have some leakage of fluid and a deterioration of the drift is observed. Therefore, is under development the design and the fabrication of a new system to create the sealed chamber. The current gaskets are fabricated bonding a PDMS rectangular pattern $500\mu m$-high above a glass slide: it became evident that this is not sufficient to guarantee a steady state condition stable along time and this reflects on the resulting signal, whose baseline is not completely flat.
Other finer possible adjustments have been suggested: (i) the employment of a new type of connectors instead of the spring ones currently used, (ii) the design of a new cartridge to avoid any kind of variability during the chip loading, (iii) the improvement and calibration of the reader such that the pressure exerted by the connectors on the chip is a constant and manageable parameter, (iv) the calibration and complete fine-tuning of the noise amplitude associated to the movement of the motor in proximity of the chip.

CHAPTER V

Conclusions and perspectives

TMek project aims at the realization of a compact, low-cost, user-friendly and rapid pan-malaria diagnostic test, at least as sensitive as the *gold standard microscopy*. The physics underlying the system exploits the paramagnetic properties of hemozoin crystals and infected red blood cells, which are collected, thanks to magnetophoretic separation, above gold electrodes which detect and quantify them via impedimetric measurement. During this thesis, characterization, validation and optimization experiments have been carried out starting from a first prototype of the diagnostic test previously developed.

First it has been realized a MATLAB code, whose execution allows the elaboration of several parameters, among which the most important are the amplitudes and the time constants of the signals measured during the test execution. The software has been employed during the prevalidation campaign carried out in Cameroon which demonstrated the high sensitivity of the device and its promising quantification capabilities on-field. About this prevalidation campaign, a paper has been submitted and is currently under peer-review.

Other trials, to characterize the system, have been done at "Luigi Sacco" hospital on human blood samples: a Limit of Detection of 10t-RBCs$\cdot\mu l^{-1}$, and an almost linear calibration curve in the range 10-10^5t-RBCs$\cdot\mu l^{-1}$ was found. Always at "Luigi Sacco" hospital, the first demonstration of the quantification capability of TMek on a patient under treatment has been performed. A final characterization experiment to show the LoD and the quantification potential of the system also with synthetic hemozoin has been performed.

The constant main problem that always affected the TMek signals, was the *spurious drift signal*. In order to tackle it, a new chip with interpenetrated sensitive regions has been designed, fabricated and characterized. After having demonstrated its unchanged sensitivity with respect to the old chip layout using t-RBCs, several studies focusing on the PBS drift signal have been done. Even though the spurious drift has not been completely removed, the new chip showed a higher reliability given by the fact that the "white" signal is now more repeatable and presents a lower average drift.

Nevertheless, this problem of drift has not been completely solved. A possible solution could be the optimization of the gasket containing the liquid solution: in fact, if it is not stable and perfectly sealed, it leads to a liquid leakage which can wet the pads and the spring contacts, reflecting on a drift of the output signal. Strictly related to this microfluidic issues, there are other finer adjustments which include the calibration of the pressure exerted on the chip, the design of a new cartridge to improve the mechanical stability and the use of a new type of connectors, or even the possibility of wire bonding which, however, would conflicts with the low-cost requirement. Another issue, is the problem associated to the stepper motor, whose

movement in proximity of the chip causes, even in absence of magnetic particles, a "white" signal jump: to tackle this problem, a fine tuning of the amplitudes associated to the jumps seems necessary, in order to make the signal analysis more robust. Another optimization deals with the fabrication of the chip which, at the state-of-the-art, remains produced by hand with the unavoidable human error affecting it.
Even though in this work has just been mentioned, it does exist the possibility for TMek to discern among the parasite stages (i.e. *trophozoite, ring, gametocyte* etc.): to do that, it seems necessary the analysis of the dynamics of the signals, in particular the evaluation of the time constants τ. In this direction, a first set of experiments has been carried out in Rome at "Istituto Superiore di Sanità". Other important innovations could moreover been integrated to the device, such as an optical system that, exploiting the magnetophoretic capture, could analyse with an artificial intelligence approach the attracted particles.
Finally, let me mention that, even though at the moment no studies have been performed, this technology might be able to diagnose also other diseases in which organisms feed on blood and, in turn, produce hemozoin for detoxification purposes. Some examples of these include *Rhodnius prolixus, Schistosoma mansoni worms* and *Hemoproteus columbae parasite.*

Bibliography

[1] *World Health Organization, "Malaria Fact Sheet"*. https://www.who.int/news-room/fact-sheets/detail/malaria. Accessed: January 2020.

[2] World Health Organization. *World Malaria Report 2018*. 2018.

[3] *Centers for Disease Control and Prevention, "About Malaria"*. https://www.cdc.gov/malaria/about/. Accessed: January 2020.

[4] Andrej Trampuz et al. "Clinical review: Severe malaria". In: *Critical Care* 7.4 (2003), pp. 315–323. DOI: 10.1186/cc2183.

[5] Eve Worrall, Suprotik Basu, and Kara Hanson. "Is malaria a disease of poverty? A review of the literature". In: *Tropical Medicine & International Health* 10.10 (2005), pp. 1047–1059. DOI: 10.1111/j.1365-3156.2005.01476.

[6] Brian M Greenwood et al. "Malaria". In: *The Lancet* 365.9469 (2005), pp. 1487–1498. DOI: 10.1016/S0140-6736(05)66420-3.

[7] Regina N. Rabinovich et al. "malERA: An updated research agenda for malaria elimination and eradication". In: *PLoS Medicine* 14.11 (2017), pp. 1–17. ISSN: 15491676. DOI: 10.1371/journal.pmed.1002456.

[8] John M. Miller et al. "Estimating the Number of Insecticide-Treated Nets Required by African Households to Reach Continent-wide Malaria Coverage Targets". In: *JAMA* 297.20 (May 2007), pp. 2241–2250. ISSN: 0098-7484. DOI: 10.1001/jama.297.20.2241. eprint: https://jamanetwork.com/journals/jama/articlepdf/207263/jrv70007_2241_2250.pdf. URL: https://doi.org/10.1001/jama.297.20.2241.

[9] https://www.malariasite.com/treatment-of-malaria/. Accessed: March 2020.

[10] Shweta Sinha, Bikash Medhi, and Rakesh Sehgal. "Challenges of drug-resistant malaria". In: *Parasite* 21 (2014). DOI: 10.1051/parasite/2014059.

[11] World Health Organization. *World Malaria Report 2019*. 2019.

[12] *Life cycle of a malaria parasite*. https://www.britannica.com/science/malaria. Accessed: January 2020.

[13] Gurjeet Singh, Ad Urhekar, and Raksha Singh. "Comparison of Different Methods for Diagnosis of Malarial Parasites Comparison of Different Methods for Diagnosis of Malarial Parasites". In: *MGM Journal of Medical Sciences* 2 (Aug. 2015), pp. 131–136. DOI: 10.5005/jp-journals-10036-1058.

[14] Anthea Maton. "Human biology and health". In: 1993.

[15] *Life cycle of a malaria parasite*. http://www.chemistry.wustl.edu/~edudev/LabTutorials/CourseTutorials/Tutorials/Hemoglobin/Hemoglobin.htm. Accessed: March 2020.

[16] Philip J. Rosenthal and Steven R. Meshnick. "Hemoglobin catabolism and iron utilization by malaria parasites". In: *Molecular and Biochemical Parasitology* 83.2 (1996), pp. 131–139. DOI: 10.1016/S0166-6851(96)02763-6.

[17] Devasagayam TP et al. "Free radicals and antioxidants in human health: current status and future prospects". In: *J Assoc Physicians India* 52 (2004), pp. 794–804.

[18] Regis Vanderesse et al. "Inactivation of Malaria Parasites in Blood: PDT vs Inhibition of Hemozoin Formation". In: Nov. 2016. DOI: 10.5772/65053.

[19] Linus Pauling and Charles Coryell. "The Magnetic Properties and Structure of Hemoglobin, Oxyhemoglobin and Carbonmonoxyhemoglobin". In: *Proceedings of the National Academy of Sciences of the United States of America* 4.22 (1936), pp. 210–216. DOI: 10.1073/pnas.22.4.210.

[20] Nguyen Tien Huy et al. "Phospholipid Membrane-Mediated Hemozoin Formation: The Effects of Physical Properties and Evidence of Membrane Surrounding Hemozoin". In: *PLOS ONE* 8.7 (July 2013), pp. 1–7. DOI: 10.1371/journal.pone.0070025. URL: https://doi.org/10.1371/journal.pone.0070025.

[21] Amit V Pandey et al. "Hemozoin formation in malaria: a two-step process involving histidine-rich proteins and lipids". In: *Biochemical and Biophysical Research Communications* 308.4 (2003), pp. 736–743. ISSN: 0006-291X. DOI: https://doi.org/10.1016/S0006-291X(03)01465-7. URL: http://www.sciencedirect.com/science/article/pii/S0006291X03014657.

[22] M. Inyushin et al. "Superparamagnetic Properties of Hemozoin". In: *Scientific Reports* 6.May (2016), pp. 2–10. DOI: 10.1038/srep26212.

[23] David J Sullivan. "Theories on malarial pigment formation and quinoline action". In: *International Journal for Parasitology* 32.13 (Dec. 2002), pp. 1645–1653. DOI: 10.1016/S0020-7519(02)00193-5.

[24] "Malaria Diagnosis Using a Mobile Phone Polarized Microscope". In: *Scientific Reports* 5 (2015), pp. 1–13. ISSN: 20452322. DOI: 10.1038/srep13368.

[25] Lee R. Moore et al. "Hemoglobin degradation in malaria-infected erythrocytes determined from live cell magnetophoresis". In: *The FASEB Journal* 20.6 (2006), pp. 747–749. DOI: 10.1096/fj.05-5122fje.

[26] D. Scott Bohle et al. "Aggregated Heme Detoxification Byproducts in Malarial Trophozoites: β-Hematin and Malaria Pigment Have a Single S = 5/2 Iron Environment in the Bulk Phase as Determined by EPR and Magnetic Mössbauer Spectroscopy". In: *Journal of the American Chemical Society* 120.32 (1998), pp. 8255–8256. DOI: 10.1021/ja980962u.

[27] Gregory Noland, Noelle Briones, and David J. Sullivan. "The shape and size of hemozoin crystals distinguishes diverse Plasmodium species". In: *Molecular and Biochemical Parasitology* 130.2 (2003), pp. 91–99. DOI: 10.1016/S0166-6851(03)00163-4.

[28] Yves Gossuin et al. "NMR relaxation properties of the synthetic malaria pigment β-hematin". In: *Scientific Reports* 7.1 (2017), pp. 1–7. DOI: 10.1038/s41598-017-15238-3.

[29] Hugh Reyburn et al. "Rapid diagnostic tests compared with malaria microscopy for guiding outpatient treatment of febrile illness in Tanzania: Randomised trial". In: *British Medical Journal* 334.7590 (2007), pp. 403–406. DOI: 10.1136/bmj.39073.496829.AE.

[30] Noppadon Tangpukdee et al. “Malaria diagnosis: A brief review”. In: *Korean Journal of Parasitology* 47.2 (2009), pp. 93–102. DOI: 10.3347/kjp.2009.47.2.93.

[31] Mark Amexo et al. “Malaria misdiagnosis: Effects on the poor and vulnerable”. In: *Lancet* 364.9448 (2004), pp. 1896–1898. DOI: 10.1016/S0140-6736(04)17446-1.

[32] Wen Zhu, Nancy Zeng, and Ning Wang. “Sensitivity, Specificity, Accuracy, Associated Confidence Interval and ROC Analysis with Practical SAS ® Implementations K & L consulting services, Inc, Fort Washington, PA Octagon Research Solutions, Wayne”. In: *NESUG : Health Care and Life Sciences* (2010), pp. 1–9.

[33] World Health Organization. “UNITAID. Malaria Diagnostics Technology and Market Landscape - 3rd edition (2016)”. In: *Unitaid Secretariat World Health Organization* 28.April (2016).

[34] “The development of malaria diagnostic techniques: A review of the approaches with focus on dielectrophoretic and magnetophoretic methods”. In: *Malaria Journal* 15.1 (2016). DOI: 10.1186/s12936-016-1400-9.

[35] David C. Warhurst and J. E. Williams. “ACP Broadsheet no 148. July 1996. Laboratory diagnosis of malaria.” In: *Journal of Clinical Pathology* 49.7 (1996), pp. 533–538. DOI: 10.1136/jcp.49.7.533.

[36] Konza Prairie. “Methods Manual”. In: 1 (2012), pp. 1–109.

[37] *Centers for Disease Control and Prevention, Malaria diagnostic tools.* https://www.cdc.gov/malaria/diagnosis_treatment/diagnosis.html. Accessed: January 2020.

[38] Pedro Berzosa et al. “Comparison of three diagnostic methods (microscopy, RDT, and PCR) for the detection of malaria parasites in representative samples from Equatorial Guinea 11 Medical and Health Sciences 1108 Medical Microbiology”. In: *Malaria Journal* 17.1 (2018), pp. 1–12. DOI: 10.1186/s12936-018-2481-4.

[39] Gillian H. Stresman et al. “High levels of asymptomatic and subpatent Plasmodium falciparum parasite carriage at health facilities in an area of heterogeneous malaria Transmission intensity in the Kenyan highlands”. In: *American Journal of Tropical Medicine and Hygiene* 91.6 (2014), pp. 1101–1108. DOI: 10.4269/ajtmh.14-0355.

[40] Lilit Garibyan and Nidhi Avashia. “Polymerase Chain Reaction”. In: *Journal of Investigative Dermatology* 133.3 (2013), pp. 1–4. ISSN: 0022-202X. DOI: https://doi.org/10.1038/jid.2013.1. URL: http://www.sciencedirect.com/science/article/pii/S0022202X1536139X.

[41] Mallika Imwong et al. “High-Throughput Ultrasensitive Molecular Techniques for Quantifying Low-Density Malaria Parasitemias”. In: *Journal of Clinical Microbiology* 52.9 (2014). Ed. by P. H. Gilligan, pp. 3303–3309. DOI: 10.1128/JCM.01057-14. eprint: https://jcm.asm.org/content/52/9/3303.full.pdf. URL: https://jcm.asm.org/content/52/9/3303.

[42] Michael S. Cordray and Rebecca R. Richards-Kortum. “Review: Emerging nucleic acid-based tests for point-of-care detection of malaria”. In: *American Journal of Tropical Medicine and Hygiene* 87.2 (2012), pp. 223–230. DOI: 10.4269/ajtmh.2012.11-0685.

[43] Ana Maria Vasquez et al. “Diagnostic accuracy of loop-mediated isothermal amplification (LAMP) for screening malaria in peripheral and placental blood samples from pregnant women in Colombia”. In: *Malaria Journal* 17.1 (2018), pp. 1–11. DOI: 10.1186/s12936-018-2403-5. URL: https://doi.org/10.1186/s12936-018-2403-5.

[44] Matthew J. Baker et al. “Developing and understanding biofluid vibrational spectroscopy: a critical review”. In: *Chem. Soc. Rev.* 45 (7 2016), pp. 1803–1818. DOI: 10.1039/C5CS00585J. URL: http://dx.doi.org/10.1039/C5CS00585J.

[45] Ki-Ho Han and A. Bruno Frazier. “Paramagnetic capture mode magnetophoretic micro-separator for high efficiency blood cell separations”. In: *Lab Chip* 6 (2 2006), pp. 265–273. DOI: 10.1039/B514539B. URL: http://dx.doi.org/10.1039/B514539B.

[46] “Red blood cell magnetophoresis”. In: *Biophysical Journal* 84.4 (Apr. 2003), pp. 2638–2645. ISSN: 00063495. DOI: 10.1016/S0006-3495(03)75069-3.

[47] Stefan Miltenyi et al. “High gradient magnetic cell separation with MACS”. In: *Cytometry* 11.2 (1990), pp. 231–238. DOI: 10.1002/cyto.990110203.

[48] Smitha Surendran Thamarath et al. “Enhancing the sensitivity of micro magnetic resonance relaxometry detection of low parasitemia Plasmodium falciparum in human blood”. In: *Scientific Reports* 9.1 (2019), pp. 1–9. DOI: 10.1038/s41598-019-38805-2. URL: http://dx.doi.org/10.1038/s41598-019-38805-2.

[49] New Perspectives. “Malaria Diagnosis: Introduction objectives of the meeting”. In: October 1999 (2000).

[50] Livia Callegari. “Callegari_Development of a magnetic on-chip diagnostic test for malaria.pdf”. In: ().

[51] Enrico Giuliani. “Biomedical Engineering Program MSc Thesis POLITECNICO DI MILANO ON-CHIP MAGNETOPHORETIC CAPTURE & DETECTION OF RED BLOOD”. In: (2019).

[52] Amikam Aharoni. *Introduction to the Theory of Ferromagnetism*. 2000.

[53] William Fuller Brown. “Rigorous Approach to the Theory of Ferromagnetic Microstructure”. In: *Journal of Applied Physics* 29.3 (1958), pp. 470–471. DOI: 10.1063/1.1723183.

[54] Exl Lukas, Suess Dieter, and Schrefl Thomas. “Micromagnetism”. In: 5.Pt 1 (1970), pp. 217–228. DOI: 10.1007/978-3-642-25583-0_8.

[55] Stephen Blundell. *Magnetism in Condensed Matter*. 2001.

[56] V. Sechovský. “Magnetism in Solids: General Introduction”. In: *Encyclopedia of Materials: Science and Technology* (2001), pp. 5018–5032. DOI: 10.1016/b0-08-043152-6/00872-x.

[57] L. D. Landau and E. M. Lifshitz. *Electrodynamics of continuous media*. 1960.

[58] Melinda Toth. “Magnetic Properties of Sr2YRu1-xIrxO6 Compounds”. PhD thesis. May 2013.

[59] Xiaoxia Jin et al. “Differences in magnetically induced motion of diamagnetic, paramagnetic, and superparamagnetic microparticles detected by cell tracking velocimetry”. In: *Analyst* 133 (12 2008), pp. 1767–1775. DOI: 10.1039/B802113A. URL: http://dx.doi.org/10.1039/B802113A.

[60] William M. Spees et al. “Water proton MR properties of human blood at 1.5 Tesla: Magnetic susceptibility, T1, T2, T, and non-Lorentzian signal

behavior". In: *Magnetic Resonance in Medicine* 45.4 (2001), pp. 533–542. DOI: 10.1002/mrm.1072. eprint: https://onlinelibrary.wiley.com/doi/pdf/10.1002/mrm.1072. URL: https://onlinelibrary.wiley.com/doi/abs/10.1002/mrm.1072.

[61] "Red blood cell magnetophoresis". In: *Biophysical Journal* 84.4 (2003). DOI: 10.1016/S0006-3495(03)75069-3.

[62] S. Hackett et al. "Magnetic susceptibility of iron in malaria-infected red blood cells". In: *Biochimica et Biophysica Acta (BBA) - Molecular Basis of Disease* 1792.2 (2009), pp. 93–99. ISSN: 0925-4439. DOI: 10.1016/J.BBADIS.2008.11.001. URL: https://www.sciencedirect.com/science/article/pii/S0925443908002238?via%7B%5C%%7D3Dihub.

[63] Coronado et al. "Malarial Hemozoin: From target to tool". In: *Bone* 23.1 (2012), pp. 1–7. DOI: 10.1038/jid.2014.371. arXiv: NIHMS150003.

[64] M. Giacometti et al. "Electrical and magnetic properties of hemozoin nanocrystals". In: *Applied Physics Letters* 113.20 (2018), p. 203703. DOI: 10.1063/1.5050062. eprint: https://doi.org/10.1063/1.5050062. URL: https://doi.org/10.1063/1.5050062.

[65] Jeonghun Nam et al. "Magnetic Separation of Malaria-Infected Red Blood Cells in Various Developmental Stages". In: *Analytical Chemistry* 85.15 (2013). PMID: 23815099, pp. 7316–7323. DOI: 10.1021/ac4012057. eprint: https://doi.org/10.1021/ac4012057. URL: https://doi.org/10.1021/ac4012057.

[66] E. P. Furlani. "Analysis of particle transport in a magnetophoretic microsystem". In: *Journal of Applied Physics* 99.2 (2006), pp. 1–35. ISSN: 00218979. DOI: 10.1063/1.2164531.

[67] A. Einstein. "Über die von der molekularkinetischen Theorie der Wärme geforderte Bewegung von in ruhenden Flüssigkeiten suspendierten Teilchen". In: *Annalen der Physik* 322.8 (1905), pp. 549–560. DOI: 10.1002/andp.19053220806. eprint: https://onlinelibrary.wiley.com/doi/pdf/10.1002/andp.19053220806. URL: https://onlinelibrary.wiley.com/doi/abs/10.1002/andp.19053220806.

[68] https://www.labce.com/spg579126_red_blood_cell_rbc_size_variation.aspx. Accessed: February 2020.

[69] P. Sajeesh and Ashis Kumar Sen. "Particle separation and sorting in microfluidic devices: A review". In: *Microfluidics and Nanofluidics* 17.1 (2014), pp. 1–52. ISSN: 16134990. DOI: 10.1007/s10404-013-1291-9.

[70] Adam C. Siegel et al. "Cofabrication of Electromagnets and Microfluidic Systems in Poly(dimethylsiloxane)". In: *Angewandte Chemie International Edition* 45.41 (2006), pp. 6877–6882. DOI: 10.1002/anie.200602273. URL: https://onlinelibrary.wiley.com/doi/abs/10.1002/anie.200602273.

[71] https://it.wikipedia.org/wiki/Magneti_al_neodimio. Accessed: March 2020.

[72] https://www.comsol.com/. Accessed: March 2020.

[73] https://www.sigmaaldrich.com/catalog/product/sigma/p3813?lang=it&region=IT. Accessed: March 2020.

[74] https://www.supermagnete.it/faq/Che-cosa-significano-le-indicazioni-N42-N45-N50-ecc. Accessed: March 2020.

[75] J. Ross Macdonald. "Impedance spectroscopy". In: *Annals of Biomedical Engineering* 20.3 (1992), pp. 289–305. ISSN: 00906964. DOI: 10.1007/BF02368532.

[76] M. Ibrahim et al. "Physical and electrical modeling of interdigitated electrode arrays for bioimpedance spectroscopy". In: *Lecture Notes in Electrical Engineering* 83 LNEE (2011), pp. 169–189. ISSN: 18761100. DOI: 10.1007/978-3-642-17943-3_9.

[77] Keith Leaver. "Conduction in Semiconductors". In: *Microelectronic Devices* (1997), pp. 1–31. DOI: 10.1142/9781860943041_0001.

[78] M. Waleed Shinwari, M. Jamal Deen, and Dolf Landheer. "Study of the electrolyte-insulator-semiconductor field-effect transistor (EISFET) with applications in biosensor design". In: *Microelectronics Reliability* 47.12 (2007), pp. 2025–2057. ISSN: 00262714. DOI: 10.1016/j.microrel.2006.10.003.

[79] M. Endo et al. "High Power Electric Double Layer Capacitor (EDLC's); from Operating Principle to Pore Size Control in Advanced Activated Carbons". In: *Carbon letters* 1 (Jan. 2001).

[80] Keith B. Oldham. "A Gouy-Chapman-Stern model of the double layer at a (metal)/(ionic liquid) interface". In: *Journal of Electroanalytical Chemistry* 613.2 (2008), pp. 131–138. ISSN: 15726657. DOI: 10.1016/j.jelechem.2007.10.017.

[81] https://gibbslabblog.files.wordpress.com/2017/03/edl.jpg. Accessed: March 2020.

[82] H. L. Lord, W. Zhan, and J. Pawliszyn. *Fundamentals and applications of needle trap devices*. Vol. 2. 2012, pp. 677–697. ISBN: 9780123813749. DOI: 10.1016/B978-0-12-381373-2.00056-9.

[83] M. Ibrahim et al. "Geometric parameters optimization of planar interdigitated electrodes for bioimpedance spectroscopy". In: *Journal of Electrical Bioimpedance* 4.1 (2013), pp. 13–22. ISSN: 1891-5469. DOI: 10.5617/jeb.304.

[84] S. Gawad, L. Schild, and Ph. Renaud. "Micromachined impedance spectroscopy flow cytometer for cell analysis and particle sizing". In: *Lab Chip* 1 (1 2001), pp. 76–82. DOI: 10.1039/B103933B. URL: http://dx.doi.org/10.1039/B103933B.

[85] C. G. Granqvist and O. Hunderi. "Conductivity of inhomogeneous materials: Effective-medium theory with dipole-dipole interaction". In: *Phys. Rev. B* 18 (4 Aug. 1978), pp. 1554–1561. DOI: 10.1103/PhysRevB.18.1554. URL: https://link.aps.org/doi/10.1103/PhysRevB.18.1554.

[86] D. Stroud. "Generalized effective-medium approach to the conductivity of an inhomogeneous material". In: *Phys. Rev. B* 12 (8 Oct. 1975), pp. 3368–3373. DOI: 10.1103/PhysRevB.12.3368. URL: https://link.aps.org/doi/10.1103/PhysRevB.12.3368.

[87] https://www.autodesk.it/products/autocad/overview. Accessed: March 2020.

[88] http://www.polifab.polimi.it/. Accessed: March 2020.

[89] https://www.mecart-cleanrooms.com/learning-center/cleanroom-classifications-iso-8-iso-7-iso-6-iso-5/. Accessed: March 2020.

[90] https://www.si-mat.com/silicon-wafers.html. Accessed: March 2020.

[91] Marc J Madou. *Fundamentals of microfabrication Second Edition*.

[92] https://microchemicals.com/. Accessed: March 2020.

[93] https://www.keyence.com/ss/products/measure/sealing/coater-type/spin.jsp. Accessed: February 2020.
[94] Marc J. Madou. *Manufacturing Techniques for Microfabrication and Nanotechnology*. 2011. DOI: 10.1201/9781439895306.
[95] Sami F. and Sainiemi L. "Reactive Ion Etching". In: *Encyclopedia of Microfluidics and Nanofluidics* (2008), pp. 1790–1790. DOI: 10.1007/978-0-387-48998-8_1358.
[96] https://plasma.oxinst.com/campaigns/technology/reactive-ion-etching. Accessed: March 2020.
[97] P. T. McCarthy, R. G. Reifenberger, and T. S. Fisher. "Thermionic and Photo-Excited Electron Emission for Energy-Conversion Processes". In: *Frontiers in Energy Research* 2 (2014), p. 54. DOI: 10.3389/fenrg.2014.00054.
[98] https://www.adnano-tek.com/electron-beam-evaporator-ebe.html. Accessed: March 2020.
[99] Michael Faraday. "Experimental researches in electricity". In: (1834).
[100] http://www.martechholdings.com/nickel-sulphamate.html. Accessed: February 2020.
[101] http://www.semicore.com/what-is-sputtering. Accessed: March 2020.
[102] https://farotex.com/technology.html. Accessed: March 2020.
[103] https://lucidant.com/index.php?route=product/product&product_id=323. Accessed: February 2020.
[104] Giovanna Pirri et al. "Characterization of A Polymeric Adsorbed Coating for DNA Microarray Glass Slides". In: *Analytical Chemistry* 76.5 (2004). PMID: 14987092, pp. 1352–1358. DOI: 10.1021/ac0352629. eprint: https://doi.org/10.1021/ac0352629. URL: https://doi.org/10.1021/ac0352629.
[105] https://www.mill-max.com/. Accessed: March 2020.
[106] https://www.physical-instruments.fr/. Accessed: March 2020.
[107] https://emedicine.medscape.com/article/204178-overview. Accessed: March 2020.
[108] Michael John Matteucci, William Job Reed, and David Alan Tanen. "Sodium Thiosulfate Fails to Reduce Nitrite-induced Methemoglobinemia in Vitro". In: *Academic Emergency Medicine* 10.4 (2003), pp. 299–302. DOI: 10.1111/j.1553-2712.2003.tb01339.x. eprint: https://onlinelibrary.wiley.com/doi/pdf/10.1111/j.1553-2712.2003.tb01339.x. URL: https://onlinelibrary.wiley.com/doi/abs/10.1111/j.1553-2712.2003.tb01339.x.
[109] M. Mantynen. "Temperature correction coefficients of electrical conductivity and of density measurements for saline groundwater". In: June (2001), pp. 1–40.
[110] http://www.mit.edu/~6.777/matprops/su-8.htm. Accessed: April 2020.
[111] https://www.alere.com/en/home/product-details/sd-bioline-malaria-ag-p-f-pan.html. Accessed: March 2020.
[112] Robertson. "1986 - Unknown - © 1986 Nature Publishing Group". In: *Nature* (1986).